4-12-2021 1:00 PM

Burst Capacity Evaluation of Corroded Pipelines under Internal Pressure and Internal Pressure Combined with Longitudinal Compression

Shulong Zhang, *The University of Western Ontario*

Supervisor: Zhou, Wenxing, *The University of Western Ontario*

A thesis submitted in partial fulfillment of the requirements for the Doctor of Philosophy degree in Civil and Environmental Engineering

Recommended Citation

Zhang, Shulong, "Burst Capacity Evaluation of Corroded Pipelines under Internal Pressure and Internal Pressure Combined with Longitudinal Compression" (2021). *Electronic Thesis and Dissertation Repository*. 7700.
https://ir.lib.uwo.ca/etd/7700

Abstract

Central to the design and integrity assessment of oil and gas transmission pipelines is to accurately evaluate their pressure containment capacities, i.e. burst capacities. Corrosion defects threaten the structural integrity of pipelines as they cause thinning of the pipe wall and therefore reduce the burst capacity. Corroded in-service pipelines may be subjected to longitudinal compression resulting from, for example, ground movement or formation of free spans, in addition to internal pressures. The main objective of the research reported in this thesis is to facilitate Fitness-For-Service (FFS) assessment of corroded pipelines.

The first study investigates the conservatism associated with the rectangular and semi-ellipsoidal idealizations of corrosion defects of naturally-occurring corrosion defects by finite element analysis (FEA). The semi-ellipsoidal idealization of naturally-occurring corrosion defects in FEA is found to lead to more accurate predictions of the burst capacity than the rectangular idealization for defects that are less than 70% through the pipe wall thickness. The FEA results conducted with the semi-ellipsoidal-shaped defects indicate that the burst capacity in general increases as the defect width increases if the defect depth and length remain the same. The defect width effect is marked for deep, relatively short defects, and should therefore be taken into account accordingly in the empirical or semi-empirical burst capacity models.

The second study proposes a new burst capacity model for corroded pipelines based on extensive parametric three-dimensional (3D) elasto-plastic FEA validated by full-scale burst tests. Based on the well-known NG-18 equation, the proposed model takes into account the beneficial effect of the defect width on the burst capacity and employs a new Folias factor that depends on both the defect depth and length. The flow stress in the proposed model is defined as a function of the strain hardening exponent and ultimate tensile strength of the pipe steel based on the analytical solution of the burst capacity of defect-free pipes. The accuracy of the proposed model is validated using extensive parametric FEA and shown to be higher than existing burst capacity models.

The third study investigates the burst capacity of corroded pipelines under combined internal pressure and longitudinal compression based on extensive parametric 3D elastic-plastic FEA.

It is observed that the longitudinal compressive stress can markedly reduce the burst capacity of corroded pipelines. The adverse effect of the compressive stress on the burst capacity is the strongest for wide, relatively shallow defects, and relatively insensitive to the defect length. Based on the parametric FEA results, an artificial neural network (ANN) model is developed in the open-source platform PYTHON to predict the burst capacity of pipelines under internal pressure only or combined loads. The ANN model is validated using FEA and full-scale burst tests conducted by DNV and the results indicate good accuracy of the ANN model.

The fourth study develops a new semi-empirical burst capacity model for corroded oil and gas pipelines under combined internal pressure and longitudinal compression. The proposed model evaluates the burst capacity of a corroded pipeline under combined loads as the burst capacity of the pipeline under internal pressure only, which is proposed in the second study, multiplied by a correction factor to account for the effect of the longitudinal compression. Extensive parametric elastoplastic FEA are carried out, the results of which are used as the basis to develop the correction factor as a function of the corrosion defect sizes and magnitude of the longitudinal compressive stress. The proposed model is validated by a large set of parametric FEA and full-scale burst tests reported in the literature, and is shown to provide marked improvements over two existing models, the DNV and RPA-PLLC models, for corroded pipelines under combined loads.

The fifth study investigates the interaction effect on the burst capacity of oil and gas pipelines containing closely-spaced corrosion defects under combined internal pressure and longitudinal compression by carrying out extensive parametric 3D elasto-plastic finite element analyses. The analysis results reveal that the interaction effects under combined loads are different from the interaction effects under internal pressure only. The interaction between circumferentially-aligned defects under combined loads is significant: the burst capacity corresponding to the two-defect case can be markedly lower than that corresponding to the single-defect case. On the other hand, the interaction between longitudinally-aligned defects under combined loads is negligible due to the so-called shielding effect.

Keywords

Pipeline, corrosion defect, burst capacity, longitudinal compression, finite element analysis (FEA), artificial neural network (ANN), semi-empirical model, defect interaction.

Summary for Lay Audience

Steel pipelines are widely considered the most efficient and safest mode of transmitting and distributing large quantity of hydrocarbon products (e.g., crude oil, natural gas and various petroleum products). Canada has more than 840,000 kilometres (km) of transmission, gathering and distribution pipelines with most provinces having significant pipeline infrastructure. Of this amount, about 73,000 km are federally regulated pipelines which are primarily transmission pipelines. According to the National Conference of State Legislatures, the United States maintains about 2 million miles of natural gas distribution mains and pipelines, 321,000 miles of gas transmission and gathering pipelines, 175,000 miles hazardous liquid pipelines. Failures of pipelines, albeit infrequent, will cause undesirable impacts on economies, environment and the living conditions of residents. The metal-loss corrosion is one of the most common threats to the structural integrity of pipelines. Based on the Pipeline and Hazardous Material Safety Administration (PHMSA) database, the incidents on onshore gas transmission pipelines from 2002 to 2013 indicates that corrosion is responsible for 32.1% of all incidents. This research will improve the accuracy of fitness-for-service assessments of corroded pipelines in practice including the combined loading condition and provide practical recommendations for the defect interaction rules under combined loads.

Co-Authorship Statement

A version of Chapter 2, co- authored by **Shulong Zhang** and Wenxing Zhou, has been published in *Thin-Walled Structures, 154*, 106806. https://doi.org/10.1016/j.tws.2020.106806

A version of Chapter 3, co- authored by **Shulong Zhang** and Wenxing Zhou, has been published in *Journal of Natural Gas Science and Engineering*, 103812. https://doi.org/10.1016/j.jngse.2021.103812

A version of Chapter 4, co- authored by **Shulong Zhang**, Wenxing Zhou and Shenwei Zhang, has been published in In *International Pipeline Conference* (Vol. 84447, p. V001T03A028), ASME. https://doi.org/10.1115/IPC2020-9631

A version of Chapter 5, co- authored by **Shulong Zhang** and Wenxing Zhou, is currently under review for possible publication in *Journal of Pressure Vessel Technology*, ASME.

A version of Chapter 6, co- authored by **Shulong Zhang** and Wenxing Zhou, is currently under review for possible publication in *Engineering Structures* (revision submitted).

Acknowledgments

I have been very fortunate and grateful to have Dr. Wenxing Zhou as my supervisor during my Ph.D. study. I would like to express my sincere gratitude to Prof. Zhou, for his invaluable advice, continuous support and patience throughout my study in Western University. His immense knowledge and plentiful experience have encouraged me in all the time of my academic research. I am always impressed by his dedication to research work, critical thinking, and excellent technical writing skills. It has been a great privilege and joy of studying under his guidance and supervision. This thesis would not have been fulfilled without his help.

I gratefully acknowledge the financial support provided by the Natural Sciences and Engineering Research Council of Canada (NSERC) and the Faculty of Engineering at Western university.

Finally, my heartfelt thanks go to my parents and my sister for their unwavering support and belief in me.

Table of Contents

List of Tables

List of Figures

List of Appendices

List of Symbols

Chapter 1

d	maximum defect depth, in the through wall thickness direction
l	defect length, in the pipe longitudinal direction
w	defect width, in the pipe circumferential direction

Chapter 2

D	pipe outside diameters
d	maximum defect depth, in the through wall thickness direction
E	Young's modulus
e	base of the natural logarithm
K	coefficient of the power-law stress-strain relationship in the plastic domain
l	defect length, in the pipe longitudinal direction
n	strain hardening exponent.
t	pipe wall thicknesses
w	defect width, in the pipe circumferential direction
ε	true strain in the uniaxial tensile test
ε'	engineering strain
σ'	engineering stress
σ	true stress and true strain in the uniaxial tensile test
σ_y	yield strength
σ_u	ultimate tensile strength
P_{b-i}	burst capacity of corresponding base case for *i*
P_{FEA}	FEA-predicted burst capacities
P_i	burst capacity of a given analysis case *i*
P_{FEA}^{Rec}	FEA-predicted burst capacities for rectangular and idealization
P_{FEA}^{Se}	FEA-predicted burst capacities for semi-ellipsoid idealization
P_{test}	actual burst capacities from tests

Chapter 3

A	area of the river-bottom profile
$A_0 = lt$	reference area

D	pipe outside diameters
d	maximum defect depth, in the through wall thickness direction
d_{ave}	average depth of the river-bottom profile of the corrosion defect
E	Young's modulus
e	base of the natural logarithm
K	coefficient of the power-law stress-strain relationship in the plastic domain
l	defect length, in the pipe longitudinal direction
M	Folias (bulging) factor
n	strain hardening exponent.
t	pipe wall thicknesses
w	defect width, in the pipe circumferential direction
ε	true strain in the uniaxial tensile test
σ	true stress and true strain in the uniaxial tensile test
σ_f	material flow stress
σ_{hb}	failure stress, i.e. the hoop stress at burst
σ_u	ultimate tensile strength
σ_y	yield strength
P_b	remaining strength of the corroded pipe, i.e. burst capacity
P_0	burst capacity of the defect-free pipe
f_w	defect width factor

Chapter 4

a	constant, in the range of 0~10
D	pipe outside diameters
d	maximum defect depth, in the through wall thickness direction
E	Young's modulus
e	base of the natural logarithm
G	number of the hidden units
K	coefficient of the power-law stress-strain relationship in the plastic domain
l	defect length, in the pipe longitudinal direction
n	strain hardening exponent.
w	defect width, in the pipe circumferential direction

t	pipe wall thicknesses
ε	true strain in the uniaxial tensile test
ε'	engineering strain
σ	true stress and true strain in the uniaxial tensile test
σ'	engineering stress
σ_a	nominal longitudinal compressive stress
σ_y	yield strength
σ_u	ultimate tensile strength
F_a	longitudinal compressive force
f_w	defect width factor
g_1	number of input units
g_2	number of output units
M_b	bending moment
P_{ANN}	ANN -predicted burst capacities
P_{Base}	burst capacity of base case.
P_{Comp}	burst capacity under combined loads
P_{FEA}	FEA-predicted burst capacities
P_{test}	actual burst capacities from tests

Chapter 5

D	pipe outside diameters
d	maximum defect depth, in the through wall thickness direction
E	Young’s modulus
e	base of the natural logarithm
K	coefficient of the power-law stress-strain relationship in the plastic domain
l	defect length, in the pipe longitudinal direction
n	strain hardening exponent.
t	pipe wall thicknesses
w	defect width, in the pipe circumferential direction
ε	true strain in the uniaxial tensile test
σ	true stress and true strain in the uniaxial tensile test
σ_a	nominal longitudinal compressive stress

σ_u	ultimate tensile strength
σ_y	yield strength
α_{area}	factor that depends on the area of the metal loss projected on the longitudinal plane adopted in RPA-PLLC model
F_a	longitudinal compressive force
F_p	pressure-induced tensile force due to the end-cap effect
F_x	resultant of the externally applied axial compressive force (F_a) and internal pressure-induced tensile force (F_p) due to the end-cap effect
f_{comb}^{FEA}	correction factor calculated with FEA results
f_{DNV}	correction factor adopted in DNV model to account for the effect of the axial compression on the burst capacity
f_{comb}	correction factor to account for the effect of the longitudinal compressive stress on the burst capacity
f_{RPA}	correction factor to account for the effect of the axial compression on the burst capacity adopted in RPA-PLLC model
f_w	defect width factor
M_b	bending moment
M_1	Folias (bulging) factor adopted in DNV model
M_2	Folias (bulging) factor adopted in RPA-PLLC model
P_b	burst capacity of the pipeline under internal pressure only
P_{b-FEA}	FEA-predicted burst capacity of base case
P_b^{comb}	combined loads
P_{b-FEA}^{comb}	FEA-predicted burst capacity of a given parametric FEA case involving combined loads
P_{DNV}	DNV model predicted burst capacities of the corroded pipeline under internal pressure only
P_{FEA}	FEA-predicted burst capacities
P_{DNV}^{comb}	DNV model predicted burst capacities of the corroded pipeline under combined loads
P_{RPA}	RPA-PLLC model predicted burst capacities of the corroded pipeline under internal pressure only
P_{RPA}^{comb}	RPA-PLLC model predicted burst capacities of the corroded pipeline under

	combined loads
P_{test}	actual burst capacities from tests

Chapter 6

D	pipe outside diameters
d	maximum defect depth, in the through wall thickness direction
E	Young’s modulus
e	base of the natural logarithm
K	coefficient of the power-law stress-strain relationship in the plastic domain
l	defect length, in the pipe longitudinal direction
n	strain hardening exponent.
t	pipe wall thicknesses
w	defect width, in the pipe circumferential direction
ε	true strain in the uniaxial tensile test
σ	true stress and true strain in the uniaxial tensile test
σ_a	nominal longitudinal compressive stress
σ_y	yield strength
σ_u	ultimate tensile strength
F_a	longitudinal compressive force
M_b	bending moment
P_b	predicted burst capacity of an analysis case containing two defects
P_{bs}	predicted burst capacity of single-defect case
P_{FEA}	FEA-predicted burst capacities
P_{test}	actual burst capacities from tests
S_C	circumferential separation distances of two neighbouring defects
S_L	longitudinal separation distances of two neighbouring defects

1 Introduction

1.1 Background

Steel pipelines are widely considered the most efficient and safest mode of transmitting and distributing large quantity of hydrocarbon products (e.g., crude oil, natural gas and various petroleum products). Canada has more than 840,000 kilometres (km) of transmission, gathering and distribution pipelines with most provinces having significant pipeline infrastructure (NRCan, 2021). Of this amount, about 73,000 km are federally regulated pipelines which are primarily transmission pipelines. According to the National Conference of State Legislatures (NCSL, 2021), the United States maintains about 2 million miles of natural gas distribution mains and pipelines, 321,000 miles of gas transmission and gathering pipelines, 175,000 miles hazardous liquid pipelines. Failures of pipelines, albeit infrequent, will cause undesirable impacts on economies, environment and the living conditions of residents. The metal-loss corrosion is one of the most common threats to the structural integrity of pipelines as shown in Figure 1.1. Lam and Zhou (2016) analyzed the incidents on onshore gas transmission pipelines from 2002 to 2013 based on the Pipeline and Hazardous Material Safety Administration (PHMSA) database indicating that corrosion is responsible for 32.1% of all incidents. The in-line inspection (ILI) tool is the most common practice throughout the pipe industry to detect and size metal loss anomalies on the pipelines. The ILI tools identify and size the metal loss corrosion defect through a data analysis process and report in a spreadsheet format, which generally includes the maximum depth (d, in the through wall thickness direction), length (l, in the pipe longitudinal direction), width of the corrosion defect (w, in the pipe circumferential direction) as shown in Fig. 1.1.

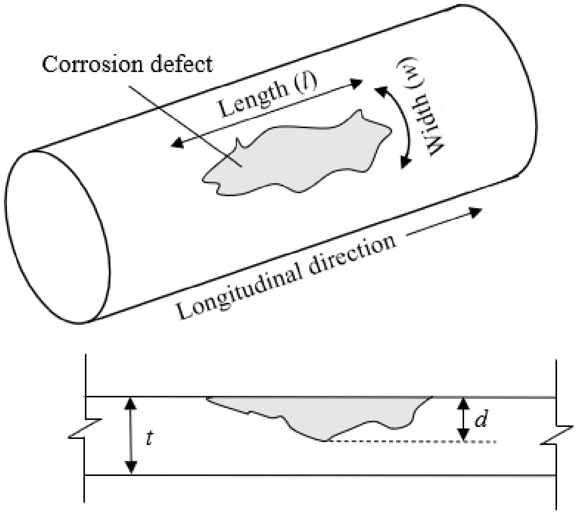

Figure 1.1 Corrosion defect on pipeline

Based on the ILI information, semi-empirical models are commonly used in practice to evaluate the burst capacity of corroded pipelines, for example, the well-known B31G (1991), B31G Modified (Kiefner and Vieth, 1989), CSA (2019), DNV (2017), RSTRENG (Kiefner and Vieth, 1990) and SHELL92 (Ritchie and Last, 1995) models. These models evaluate the burst capacity by taking into account the length and depth of the corrosion defect, but ignoring the influence of the defect width. Many recently developed burst capacity models (Netto, 2009; Chen et al., 2015; Su et al., 2016; Shuai et al., 2017; Keshtegar and Seghier, 2018) include the defect width as a model parameter. For all of such models, an increase in the defect width leads to a decrease in the burst capacity, all the other parameters being unchanged. Idealized corrosion defects are considered in the semi-empirical models, for example, rectangular and semi-ellipsoidal idealizations. The effect of the defect width on the burst capacity of corroded pipelines has been investigated based primarily on the rectangular idealization of the defect (Netto, 2009; Chen et al., 2015; Su et al., 2016; Shuai et al., 2017), which leads to the most conservative prediction. The influence of the defect width on the burst capacity remains an open question in the context of the semi-ellipsoidal idealization, which better approximates the geometry of real corrosion defects than the commonly used rectangular (or cubic) idealization.

Corroded in-service pipelines may be subjected to longitudinal tensile or compressive forces and bending moments resulting from, for example, ground movement or formation of free spans (Karimian, 2006; Wijewickreme et al., 2009; Meidani et al., 2017, 2018), in addition to internal pressures. The burst capacity of a corroded pipeline under the combined internal pressure and longitudinal compression can be markedly lower than that of the pipeline under the internal pressure only as confirmed by both experimental and numerical studies reported in the literature (Chouchaoui, 1995; Bjørnøy et al., 2000; Smith and Waldhart, 2000; Liu et al., 2009; Mondal and Dhar, 2019). Note that the longitudinal compression may result from a compressive force or bending moment (with the corrosion defect located on the compression side of the bending). Widely-used semi-empirical fitness-for-service (FFS) assessment models for corroded pipelines, such as the B31G (1991), B31G Modified (Kiefner and Vieth, 1989), CSA (2019), RSTRENG (Kiefner and Vieth, 1990) and SHELL92 (Ritchie and Last, 1995) models, consider the internal pressure only. The two most well-known practical FFS assessment models for corroded pipelines under combined loads, the one recommended in DNV RP-F101 (2017) and the RPA-PLLC model proposed in (Benjamin, 2008) (RPA stands for the rectangular parabolic area, and PLLC stands for the pressure loading plus longitudinal compression), cannot adequately capture the effect of compressive stress on the burst capacity of corroded pipelines. This is because both models include a relatively high threshold compressive stress (typically greater than 30% of the pipe yield strength), below which the compressive stress is considered to have no effect on the burst capacity. This however is inconsistent with observations obtained in recent studies (Liu et al., 2009; Mondal and Dhar, 2019; Zhang and Zhou, 2020). Results of FEA (Mondal and Dhar, 2019) indicate that a compressive stress equal to about 15% of the pipe yield strength can result in a 8~17% reduction in the burst capacity of corroded pipelines. This suggests that the DNV and RPA-PLLC models do not adequately capture the effect of compressive stress on the burst capacity of corroded pipelines.

Multiple corrosion defects often exist in close proximity on a given pipeline. This can lead to the so-called interaction effect; that is, the burst capacity of the pipeline containing multiple closely-spaced defects is lower than those of the same pipeline containing each of the defects individually. Extensive experimental and numerical studies have been reported in the literature to investigate the interaction of two closely-spaced corrosion defects on pipelines subjected to the internal pressure only (Benjamin et al., 2005, 2006; Silva et al., 2007; Li et al., 2016; Xu et al., 2017; Al-Owaisi et al., 2018; Sun and Cheng, 2018). Simple-to-use (generally conservative) defect interaction rules have also been suggested in various standards and recommended practice to facilitate the integrity assessment of corroded pipelines in practice (Kiefner and Vieth, 1990; ASME, 2017; DNV, 2017; CSA, 2019) for the loading condition of internal pressure only.

1.2 Objective

The study in this thesis is financially supported by Natural Sciences and Engineering Research Council (NSERC) of Canada. The objectives of this study are summarized as follows.

1) Investigate the conservatism associated with the rectangular and semi-ellipsoidal idealizations of corrosion defects and the effect of the defect width on the burst capacity based on semi-ellipsoidal idealization using extensive 3D elasto-plastic FEA

2) Propose a new burst capacity model for corroded pipeline under internal pressure only to achieve high predictive accuracy of the burst capacity.

3) Evaluate the influence of longitudinal compression on the burst capacity of corroded pipelines by using FEA and ANN technique.

4) Develop a new semi-empirical burst capacity model for corroded oil and gas pipelines under combined internal pressure and longitudinal compression.

5) Investigate the interaction effect on the burst capacity of oil and gas pipelines containing closely-spaced corrosion defects under combined internal pressure and longitudinal compression by carrying out extensive parametric 3D elasto-plastic FEA.

This research will improve the accuracy of fitness-for-service assessments of corroded pipelines in practice including the combined loading condition and provide practical recommendations for the defect interaction rules under combined loads.

1.3 Scope of the study

This thesis consists of five main topics that are presented in Chapters 2 to 6, respectively. Chapter 2 investigates the conservatism associated with the rectangular and semi-ellipsoidal idealizations of corrosion defects by comparing the FEA-predicted burst capacities corresponding to these idealizations with the burst capacities observed in a set of full-scale burst tests of pipe specimens containing naturally-occurring corrosion defects (Bao et al., 2018). Then, systematic parametric 3D FEA is carried out to have an in-depth understanding of the influence of the defect width on the burst capacity of corroded pipelines and its implication for the burst capacity predicted by semi-empirical models.

Chapter 3 develops a new burst capacity model for corroded pipeline based on a large number of parametric elasto-plastic FEA validated by full-scale tests. The proposed model follows the basic form of the NG-18 equation but incorporates the defect width as an input parameter in the model, a new Folias factor equation that depends on both the defect depth and length and the same flow stress defined as a function of the strain hardening exponent and ultimate tensile strength of the pipe steel based on the analytical solution of the burst capacity of defect-free pipes. The accuracy of the proposed model is validated using extensive parametric FEA and shown to be higher than those of six well-known NG-18-family models, i.e. the B31G, B31G Modified, CSA, DNV, RSTRENG and SHELL92 and a model recently proposed by Sun et al.

Chapter 4 evaluates the burst capacity of corroded pipelines under combined internal pressure and longitudinal compression loading condition based on extensive parametric 3D elastic-plastic FEA and artificial neural network (ANN) technique. The inter-dependent influence of the defect dimension on the longitudinal compression effect on the burst capacity compression by varying the defect depth, length and width, and magnitude of axial compressive stress. Based on the parametric FEA results, an ANN model is developed to predict the burst capacity of pipelines containing single corrosion defects under internal pressure only or combined internal pressure and axial compression.

Chapter 5 proposes a new semi-empirical burst capacity model for corroded oil and gas pipelines under combined internal pressure and longitudinal compression. The proposed model evaluates the burst capacity of a corroded pipeline under combined loads as the burst capacity of the pipeline under internal pressure only, which is developed in Chapter 3, multiplied by a correction factor to account for the effect of the longitudinal compression. Extensive parametric elastoplastic FEA results, conducted in Chapter 4, are used as the basis to develop the correction factor as a function of the corrosion defect sizes and magnitude of the longitudinal compressive stress. The proposed model is validated by a large set of parametric FEA and full-scale burst tests reported in the literature, and is shown to provide marked improvements over two existing models, the DNV and RPA-PLLC models, for corroded pipelines under combined loads.

Chapter 6 investigates the interaction effect on the burst capacity of oil and gas pipelines containing closely-spaced corrosion defects under combined internal pressure and longitudinal compression by carrying out extensive parametric 3D elasto-plastic FEA. The analysis considers two identical, semi-ellipsoidal-shaped corrosion defects aligned circumferentially or longitudinally on the pipeline. The adequacy of four practical interaction rules, DNV RP F101, B31G and CSA Z662 (CSA) as well as that recommended by Kiefner and Vieth (KV), is also examined for the combined loading condition.

1.4 Thesis format

This thesis is prepared as an Integrated-Article Format as specified by the School of Graduate and Postdoctoral Studies at Western University, London, Ontario, Canada. A total of 7 chapters are included in this thesis. Chapter 1 presents the introduction of the thesis which includes the research background, objective, scope of the study and thesis format. Chapters 2 through 6 are the main body of the thesis, of which each chapter addresses an individual topic. Finally, the main conclusions and recommendations for future research regarding the topics in the thesis are included in Chapter 7.

References

According to National Conference of State Legislatures (NCSL), 2021. Making State Gas Pipelines Safe and Reliable: An Assessment of State Policy. https://www.ncsl.org/research/energy/state-gas-pipelines.aspx

Al-Owaisi, S., Becker, A. A., Sun, W., Al-Shabibi, A., Al-Maharbi, M., Pervez, T., & Al-Salmi, H., 2018. An experimental investigation of the effect of defect shape and orientation on the burst pressure of pressurised pipes. *Engineering Failure Analysis*, *93*, 200-213.

ASME, 1991. Manual for determining the remaining strength of corroded pipelines- a supplement to ASME B31 code for pressure piping, The American Society of Mechanical Engineers, New York.

Bao, J., Zhang, S., Zhou, W., & Zhang, S., 2018. Evaluation of Burst Pressure of Corroded Pipe Segments Using Three-Dimensional Finite Element Analyses. In *2018 12th International Pipeline Conference* (pp. V001T03A043-V001T03A043). American Society of Mechanical Engineers.

Benjamin, A. C., Freire, J. L. F., Vieira, R. D., Diniz, J. L., & de Andrade, E. Q., 2005. *Burst tests on pipeline containing interacting corrosion defects. In ASME 2005 24th International Conference on Offshore Mechanics and Arctic Engineering* (pp. 403-417). American Society of Mechanical Engineers Digital Collection.

Benjamin, A. C., de Andrade, E. Q., Jacob, B. P., Pereira, L. C., & Machado, P. R., 2006. Failure behavior of colonies of corrosion defects composed of symmetrically arranged defects. In *2006 International Pipeline Conference* (pp. 417-432). American Society of Mechanical Engineers Digital Collection.

Benjamin, A. C., 2008. Prediction of the failure pressure of corroded pipelines subjected to a longitudinal compressive force superimposed to the pressure loading. In *International Pipeline Conference* (Vol. 48586, pp. 179-189).

Bjørnøy, O. H., Sigurdsson, G., & Cramer, E., 2000. Residual strength of corroded pipelines, DNV test results. In *The Tenth International Offshore and Polar Engineering Conference*. International Society of Offshore and Polar Engineers.

Canadian Standard Association, (CSA), 2019. Oil and gas pipeline systems. CSA standard Z662-19. *Mississauga, Ontario, Canada*.

Chen, Y., Zhang, H., Zhang, J., Li, X., & Zhou, J., 2015. Failure analysis of high strength pipeline with single and multiple corrosions. *Materials & Design, 67*, 552-557.

Chouchaoui, B. (1995). Evaluating the remaining strength of corroded pipelines, PhD thesis, University of Waterloo.

Det Norske Veritas (DNV), 2017. Recommended practice DNV-RP-F101, corroded pipelines, Hovic, Norway.

Karimian, S. A., 2006. Response of buried steel pipelines subjected to longitudinal and transverse ground movement (Doctoral dissertation, University of British Columbia).

Keshtegar, B., & Seghier, M. E. A. B., 2018. Modified response surface method basis harmony search to predict the burst pressure of corroded pipelines. *Engineering Failure Analysis, 89*, 177-199.

Kiefner, J. and Vieth, P., 1989. A modified criterion for evaluating the remaining strength of corroded pipe (No. PR-3-805). Battelle Memorial Institute, OH (USA).

Kiefner, J. and Vieth, P., 1990. PC program speeds new criterion for evaluating corroded pipe, *Oil and Gas Journal*, August 20, 1990. pp. 91-93.

Lam, C., & Zhou, W. (2016). Statistical analyses of incidents on onshore gas transmission pipelines based on PHMSA database. *International Journal of Pressure Vessels and Piping, 145*, 29-40.

Li, X., Bai, Y., Su, C., & Li, M., 2016. Effect of interaction between corrosion defects on failure pressure of thin wall steel pipeline. *International Journal of Pressure Vessels and Piping, 138*, 8-18.

Liu, J., Chauhan, V., Ng, P., Wheat, S., & Hughes, C., 2009. Remaining strength of corroded pipe under secondary (biaxial) loading (No. Report No. R9068). GL Industrial Services UK Ltd.

Meidani, M., Meguid, M. A., & Chouinard, L. E., 2017. Evaluation of soil–pipe interaction under relative axial ground movement. *Journal of Pipeline Systems Engineering and Practice, 8*(4), 04017009.

Meidani, M., Meguid, M. A., & Chouinard, L. E., 2018. Estimating earth loads on buried pipes under axial loading condition: insights from 3D discrete element analysis. *International Journal of Geo-Engineering, 9*(1), 5.

Mondal, B. C., & Dhar, A. S., 2019. Burst pressure of corroded pipelines considering combined axial forces and bending moments. *Engineering Structures, 186*, 43-51.

Natural Resources Canada (NRCan), 2021. Pipelines Across Canada. https://www.nrcan.gc.ca/our-natural-resources/energy-sources-distribution/clean-fossil-fuels/pipelines/pipelines-across-canada/18856

Netto, T. A., 2009. On the effect of narrow and long corrosion defects on the collapse pressure of pipelines. *Applied Ocean Research, 31*(2), 75-81.

Ritchie, D., & Last, S., 1995. Burst criteria of corroded pipelines-defect acceptance criteria. In *Proceedings of the EPRG/PRC 10th biennial joint technical meeting on line pipe research*. Cambridge, UK, Paper 32.

Shuai, Y., Shuai, J., & Xu, K., 2017. Probabilistic analysis of corroded pipelines based on a new failure pressure model. *Engineering Failure Analysis, 81*, 216-233.

Smith, M. Q., & Waldhart, C. J., 2000. Combined loading tests of large diameter corroded pipelines. In *2000 3rd International Pipeline Conference*. American Society of Mechanical Engineers Digital Collection.

Su, C. L., Li, X., & Zhou, J., 2016. Failure pressure analysis of corroded moderate-to-high strength pipelines. *China Ocean Engineering, 30*(1), 69-82

Silva, R. C. C., Guerreiro, J. N. C., & Loula, A. F. D., 2007. A study of pipe interacting corrosion defects using the FEM and neural networks. *Advances in Engineering Software, 38*(11-12), 868-875.

Sun, J., & Cheng, Y. F., 2018. Assessment by finite element modeling of the interaction of multiple corrosion defects and the effect on failure pressure of corroded pipelines. *Engineering Structures, 165*, 278-286.

Taylor, N., Clubb, G., & Matheson, I., 2015. The Effect of Bending and Axial Compression on Pipeline Burst Capacity. In *SPE Offshore Europe Conference and Exhibition*. Society of Petroleum Engineers.

Wijewickreme, D., Karimian, H., & Honegger, D., 2009. Response of buried steel pipelines subjected to relative axial soil movement. *Canadian Geotechnical Journal, 46*(7), 735-752.

Xu, W. Z., Li, C. B., Choung, J., & Lee, J. M., 2017. Corroded pipeline failure analysis using artificial neural network scheme. *Advances in engineering software, 112*, 255-266.

Zhang, S. & Zhou, W., 2020, Development of a burst capacity model for corroded pipelines under internal pressure and axial compression using artificial neural network, Proceedings of the 2020 13th International Pipeline Conference,September 28 – October 2, 2020, Calgary, Alberta, Canada, IPC2020-9690.

2 Assessment of Effects of Idealized Defect Shape and Width on the Burst Capacity of Corroded Pipeline

2.1 Introduction

Metal-loss corrosion threatens the structural integrity of oil and gas pipelines as it causes thinning of the pipe wall and therefore reduces the pressure containment capacity, i.e. burst capacity, of the pipeline. Semi-empirical models are commonly used in the pipeline industry to evaluate the burst capacity of corroded pipelines, for example, the well-known B31G (ASME, 1991), B31G Modified (Kiefner and Vieth, 1989), CSA (2019), DNV (2017), RSTRENG ((Kiefner and Vieth, 1990) and PCORRC (Stephens and Leis, 2000) models. These models evaluate the burst capacity by taking into account the length (in the pipe longitudinal direction) and depth (in the through-pipe wall thickness direction) of the corrosion defect, but ignoring the influence of the defect width (in the pipe circumferential direction). Many recently developed burst capacity models (Netto, 2009; Chen et al., 2015; Su et al., 2016; Shuai et al., 2017; Keshtegar and Seghier, 2018; Mokhtari and Melchers, 2018) include the defect width as a model parameter. For almost all of such models, an increase in the defect width leads to a decrease in the burst capacity, all the other parameters being unchanged. The extent to which the defect width influences the burst capacity however varies markedly among the models.

The three-dimensional (3D) elasto-plastic finite element analysis (FEA) has proven to be an effective tool to evaluate the burst capacity of corroded pipelines (Chouchaoui, 1995). Although naturally-occurring corrosion defects are irregular-shaped, corrosion defects considered in FEA are often idealized to be rectangular-shaped 3D flaws as illustrated in Fig. 2.1, which is the most conservative idealization of a naturally-occurring defect with given depth (*d*), length (*l*) and width (*w*). The semi-ellipsoidal idealization of the corrosion defect (Fig. 2.1) has been employed in a few studies (Al-Owaisi et al., 2016; Mokhtari and Melchers, 2018, 2019). In particular, Mokhtari and Melchers (2018) considered artificially-generated, complex-shaped defects in finite element models of corroded pipes, and their corresponding rectangular and semi-ellipsoidal idealizations (with the same defect depth, length and width). Based on FEA of eleven pipe models, the authors reported that the semi-ellipsoidal idealization leads to on average about 5% under-prediction of burst capacities of complex-shaped defects, whereas the rectangular idealization on average about 11% under-prediction. The accuracy of FEA is validated by full-scale burst tests of three pipe specimens containing complex-shaped defects and three containing rectangular-shaped defects (Mokhtari and Melchers, 2019). Although the complex-shaped defects considered in (Mokhtari and Melchers, 2018, 2019) are intended to mimic naturally-occurring corrosion defects, there is a lack of rigorous evidence in (Mokhtari and Melchers, 2018, 2019) that characteristics of such defects are indeed representative of those of naturally-occurring corrosion defects.

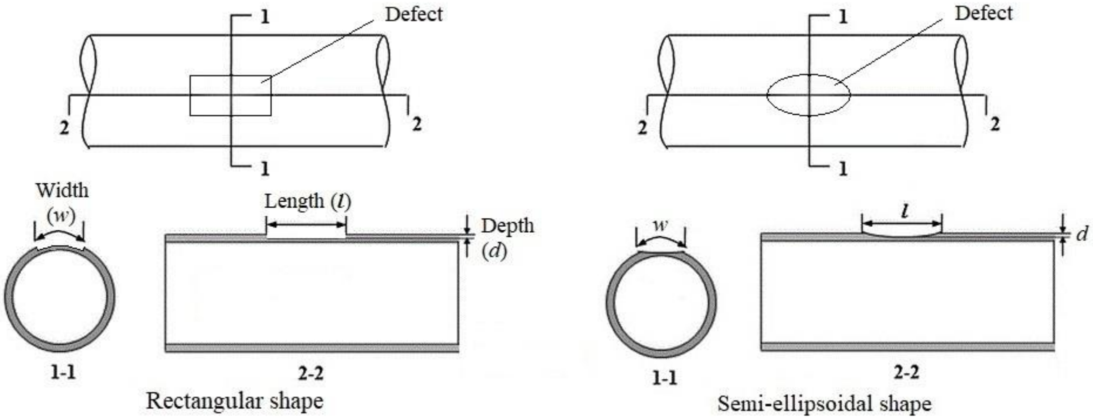

Figure 2.1 Schematics for corrosion defects idealized as rectangular and semi-ellipsoidal shapes.

Leis and Stephens (1997a, 1997b) used the shell element-based FEA to evaluate the burst capacity of pipelines containing rectangular-shaped defects. They reported that the influence of the defect width on the burst capacity is of secondary importance, i.e. less than 5%, based on a limited number of analyses. Chiodo and Ruggieri (2009) evaluated the burst capacity of pipelines containing rectangular-shaped defects by carrying out plane-strain FEA (i.e. assuming the defect to be infinitely long) and found that the defect width has a negligible effect on the burst capacity. Similar findings were reported by Cronin (2000) based on limited FEA of corrosion pits. Fekete and Varga (2012) investigated the effect of the defect width-to-length ratio on the burst capacity of corroded pipelines by using the solid element-based 3D FEA. The corrosion defects in the FEA model are characterized as ellipsoids generated by removing materials from the pipe surface using revolving elliptical surfaces. Fekete and Varga showed that the burst capacity increases markedly as the defect width-to-length ratio increases. It should however be noted that the increase in the defect width-to-length ratio is achieved by fixing the width and reducing the length. This suggests that the increase in the burst capacity is due largely to the decrease in the defect length, and the effect of the defect width-to-length ratio on the burst capacity is rather unclear. Su et al. (2016) carried out 3D FEA to investigate the burst capacity of corroded pipelines by considering rectangular-shaped defects. The authors found that the defect width has a negligible effect on the burst capacity for long corrosion defects. This finding is consistent with that reported in (Chiodo and Ruggieri, 2009). However, for short deep corrosion defects, Su et al. showed that the defect width has a significant effect on the burst capacity: the burst capacity can decrease by as much as 20% as the defect width increases while the defect depth and length remaining the same. Similar findings have also been reported in (Tan and Xiao, 2006; Chen et al., 2015; Shuai et al., 2017).

Although the semi-ellipsoidal idealization is shown to be less conservative than the rectangular idealization for artificially-generated, complex-shaped defects (Mokhtari and Melchers, 2018, 2019), it remains an open question to what degree the FEA-predicted burst capacities corresponding to these two idealizations approximate the actual burst capacity of pipelines containing naturally-occurring corrosion defects. Furthermore, the effect of the defect width on the burst capacity of corroded pipelines has been investigated based primarily on the rectangular idealization of the defect (Netto, 2009; Chen et al., 2015; Su et al., 2016; Shuai et al., 2017). The influence of the defect width on the burst capacity in the context of the semi-ellipsoidal idealization remains an open question.

The objective of the present chapter is two-fold. First, we investigate the conservatism associated with the rectangular and semi-ellipsoidal idealizations of corrosion defects by comparing the FEA-predicted burst capacities corresponding to these idealizations with the burst capacities observed in a set of recently-completed full-scale burst tests of pipe specimens containing naturally-occurring corrosion defects (Bao et al., 2018). Second, systematic parametric 3D FEA is carried out to have an in-depth understanding of the influence of the defect width on the burst capacity of corroded pipelines and its implication for the burst capacity predicted by semi-empirical models. To this end, the semi-ellipsoidal idealization of the corrosion defect is adopted in FEA. The rest of this chapter is organized as follows: Section 2.2 presents details of the finite element model and validation of the model; the difference between the rectangular and semi-ellipsoidal idealizations of the corrosion defects in terms of the burst capacity is discussed in Section 2.3; the defect width effect on the burst capacity of corroded pipelines is investigated in Section 2.4, followed by conclusions in Section 2.5.

2.2 FEA Model

2.2.1 General

The FEA analysis is performed by the commercial FEA package ABAQUS (Dassault Systèmes, 2016) in this chapter. The 8-node solid element (C3D8) with full integration is used in the numerical simulation. The finite-strain elasto-plastic analysis is employed to capture the geometrical and material non-linearity. The von Mises yield criterion and the associated flow rule as well as the isotropic hardening rule are adopted in the numerical simulation.

2.2.2 Material properties and failure criterion

The stress–strain relationship of typical pipe steels can be well represented by a power-law model as given in Eq. (2.1) (Zhu and Leis, 2004; Wang and Zhang, 2011), which is adopted in the present study.

$$\begin{cases} \sigma = E\varepsilon & \sigma < \sigma_y \\ \sigma = K\varepsilon^n & \sigma \geq \sigma_y \end{cases} \tag{2.1}$$

where σ and ε denote the true stress and true strain in the uniaxial tensile test, respectively; E is Young's modulus; σ_y is the yield strength, defined as the stress corresponding to an offset (i.e. plastic) strain of 0.2% or a total strain of 0.5%; K and n are coefficients of the power-law stress-strain relationship in the plastic domain, and n is also known as the strain hardening exponent.

If tensile coupon test results are available, the values of K and n in Eq. (1) can be obtained from curve fitting of the test data. Since the stress-strain curve obtained from the tensile coupon test is usually reported in terms of the engineering stress (σ') and engineering strain (ε'), they are converted to the corresponding true stress and true strain, respectively. In the elastic domain, σ (ε) is assumed equal to σ' (ε'). In the plastic domain, σ (ε) is converted from $\sigma'(\varepsilon')$ as follows up to the onset of necking:

$$\varepsilon = \ln (1 + \varepsilon') \tag{2.2a}$$

$$\sigma = \sigma'(1 + \varepsilon') \tag{2.2b}$$

If only the yield strength (σ_y) and ultimate tensile strength (UTS), denoted by σ_u, are known while coupon test results are unavailable, the following empirical equation can be used to estimate the value of *n* (Zhu and Leis, 2006):

$$n = 0.239 \left(\frac{1}{\sigma_y/\sigma_u} - 1 \right)^{0.596} \tag{2.3}$$

Given the value of *n*, *K* can be estimated by using the Considere's criterion (Dowling, 2007):

$$K = \frac{e^n}{n^n} \sigma_u \tag{2.4}$$

where *e* is the base of the natural logarithm.

Although there is a discontinuity between the two branches of the stress-strain curve in Eq. (2.1), it is noted that the stress-strain curve is defined in a piecewise fashion in ABAQUS (Dassault Systèmes, 2016). It follows that the discontinuity is addressed through a linear approximation of the stress-strain curve near the intersection of the two branches. Such an approximation does not impact the prediction of the burst capacity, which is governed by the second branch of Eq. (2.1) at relatively large strains.

The UTS-based failure criterion, which has been used in the literature to predict the burst capacity of corroded pipelines (Cronin, 2000; Bao et al., 2018), is adopted in this chapter. According to this criterion, the burst capacity of a corroded pipe is obtained once the maximum von Mises (true) stress at any point within the defected region reaches the true stress corresponding to UTS. Note that this criterion is different from another failure criterion commonly used in the literature (Choi et al., 2003; Mokhtari and Melchers, 2018), which states that the burst capacity is obtained once the von Mises stress throughout the remaining ligament at the deepest point within the defect region reaches 90% of the true stress corresponding to UTS.

2.2.3 Validation of FEA

Full-scale burst tests reported in the literature involving pipe specimens containing rectangular- and semi-ellipsoid-shaped defects (Benjamin et al., 2006; Al-Owaisi, 2018) are used to validate the finite element model and UTS-based failure criterion. The material properties of the test specimens obtained from the tensile coupon test results reported in (Benjamin et al., 2006; Al-Owaisi, 2018) are summarized in Table 1.1. The outside diameters (D) and wall thicknesses (t) of the test specimens are summarized in Table 2.2. Four layers of elements are used through the thickness of each defect area to ensure the high stress gradient along the radial direction of the defect area to be accurately captured. To improve the computational efficiency, the mesh in the FEA model is transitioned from a high density in the defect region to a low density in the defect-free region in the longitudinal, circumferential and radius directions and transition is modelled in the same way for rectangular- and semi-ellipsoidal-shaped defects. Because of symmetry, a half of a given specimen is modelled. The mesh density is selected after a convergence study. Figures 2.2 and 2.3 depict representative FEA meshes for pipe specimens IDTS2 and 18 containing rectangular- and semi-ellipsoid- shaped defects, respectively. The meshes in Figs. 2.2 and 2.3 consist of 15307 and 15645 nodes, respectively, with the corresponding number of elements equal to 9144 and 9450, respectively.

Table 2.1 Material properties of full-scale burst tests reported in (Benjamin et al., 2006; Al-Owaisi, 2018)

Source	Steel grade	E (GPa)	σ_y (MPa)	σ_u (MPa)	n
2.A	X80	200	534.1	661.4	0.08
2.B	X52	182	372	497.7	0.20

Note: Sources 2.A and 2.B refer to Ref (Benjamin et al., 2006) and Ref (Al-Owaisi, 2018), respectively.

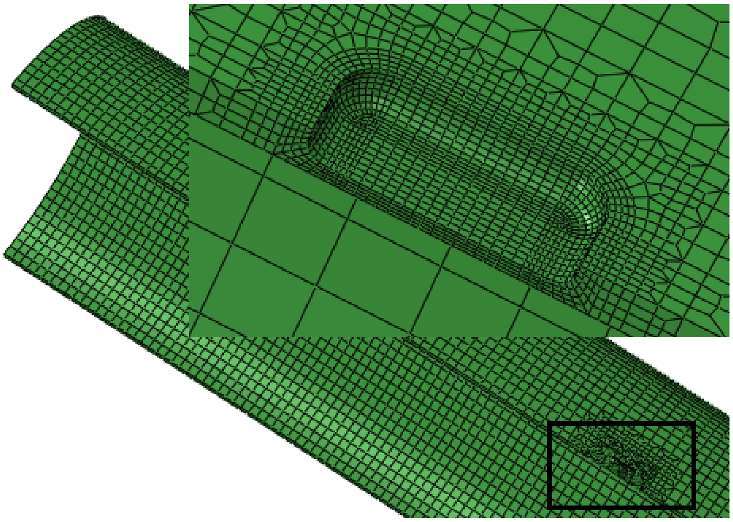

Figure 2.2 FEA mesh for the rectangular-shaped defect in test specimen IDTS2 reported in (Benjamin et al., 2006)

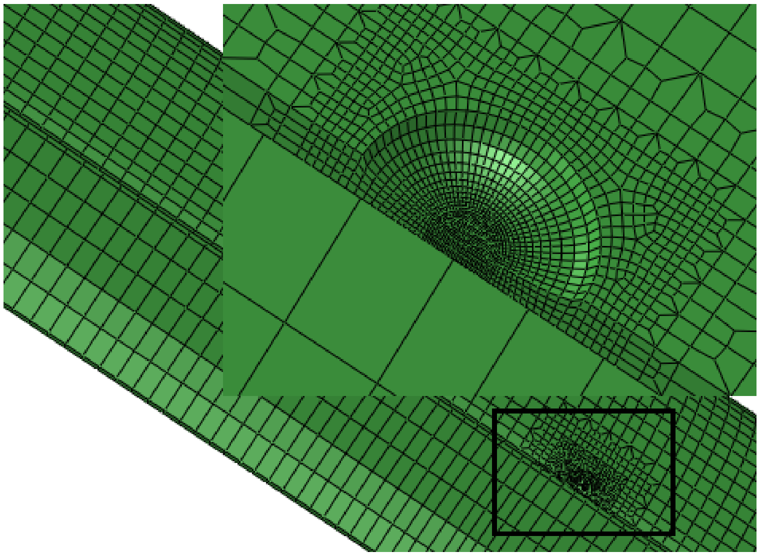

Figure 2.3 FEA mesh for the semi-ellipsoidal-shaped defect in specimen 18 reported in (Al-Owaisi, 2018)

The symmetric constraint is applied to the symmetry plane, and one end of the model is restricted in the longitudinal direction. As the pipe specimens are end caped during the burst tests, corresponding axial stress is simultaneously applied at the free end of the model while the internal pressure load is applied. The FEA-predicted burst capacities (P_{FEA}) for rectangular and semi-ellipsoid shaped defects are summarized in Table 2.2, together with the actual burst capacities from tests (P_{test}).

Table 2.2 Comparison of FEA burst prediction and test results

Source	Specimen ID	D (mm)	t (mm)	Defect shape	P_{test} (MPa)	P_{FEA} (MPa)	P_{test}/P_{FEA}
2.A	IDTS2	458.8	8.1	Rectangular	22.68	22.05	1.03
	IDTS3				20.31	19.80	1.03
	IDTS4				21.14	21.57	0.98
2.B	24	508	9.86	Rectangular	18.42	18.91	0.97
	25		9.7		18.77	19.27	0.97
	26		9.7		19.28	19.34	1.00
	18		9.7	Semi-ellipsoid	19.55	19.83	0.99
	19		9.85		19.11	19.15	1.00
	20		9.7		19.59	19.39	1.01
	21		9.7		19.65	19.48	1.01
	22		9.75		20.08	19.65	1.02
	23		9.8		20.27	19.80	1.02
Mean							1.00
COV							2.0%

Note: Sources 2.A and 2.B refer to Ref (Benjamin et al., 2006) and Ref (Al-Owaisi, 2018), respectively.

The fact that the mean and coefficient of variation (COV) of P_{test}/P_{FEA} are 1.00 and 2.0%, respectively, as presented in Table 2.2 indicates that the FEA-predicted and test burst capacities are in excellent agreement. This provides a strong validation of the finite element model and UTS-based burst criterion employed in the analysis.

2.3 Influence of idealization of defect geometry on burst capacities

To quantify the difference between the rectangular and semi-ellipsoidal idealizations of corrosion defects in terms of the burst capacity of corroded pipelines, eleven recently-completed full-scale burst tests of pipe specimens containing naturally-occurring corrosion defects (Bao et al., 2018) are analyzed using 3D FEA. The dimensions and material properties of the specimens as well as the geometry of corrosion defects on the specimens are summarized in Table 2.3. Note that the defect depth in Table 2.3 is the maximum depth of the naturally-occurring corrosion defect and adopted in the rectangular and semi-ellipsoidal defect idealization. Furthermore, the length shown in Table 2.3 is the length of the effective portion of the defect, i.e. the portion of the defect that leads to the lowest predicted burst capacity per the RSTRENG model (Kiefner and Vieth, 1990). Using the effective length as opposed to the actual length of the defect somewhat reduces the conservatism resulting from the defect idealization, as the actual lengths of the defects on some of the specimens are quite long (over 1000 mm). Photos of corrosion defects on two representative specimens (16-6 and 16-7) are included in Appendix A to illustrate the irregular geometry of the defect. The rectangular and semi-ellipsoidal idealizations of the defects in FEA models are also shown in Appendix A. More detailed information about the specimens is included in (Bao et al., 2018).

Since the pipeline wall is rolled in a circular position the commonly used method can only generate the characteristic defect model with a maximum width, w_{max}, as given by (Fekete and Varga, 2012):

$$w_{max} = 2\sqrt{dD - d^2} \tag{2.5}$$

Furthermore, even the defect width is within the generable range the generated defect profile is not strictly semi-ellipsoidal. In this study, the semi-ellipsoidal-shaped defect is first generated on a flat plate with same thickness as the pipe wall. Then the FE model is converted to a cylindrical coordinate system. Therefore, the defect profile in this study is strictly semi-ellipsoidal and is not subjected to the restriction of the maximum defect width given by Eq. (2.5).

Table 2.3 Summary of the test specimens

Specimen ID	D (mm)	t (mm)	Specimen length(mm)	Steel grade	E (GPa)	σ_y (MPa)	σ_u (MPa)	n	l (mm)	w (mm)	d/t
16-1	408.2	6.2	4361	X52	167	369	540	0.16	346	302	0.33
16-6	407.4	5.9	3001	X52	191	408	576	0.13	142	120	0.57
16-7	407.4	6.0	3230	X52	191	408	576	0.13	346	382	0.87
24-1	610.5	6.8	6384	X70	145	553	680	0.10	742	242	0.30
24-2	610.5	6.7	8152	X70	145	553	680	0.10	412	201	0.39
30-1	763.2	8.4	6185	X70	187	539	655	0.09	331	402	0.68
30-2	763.4	8.5	5768	X70	170	535	652	0.09	398	260	0.48
30-3	763.2	8.4	4970	X70	171	568	691	0.09	294	386	0.73
30-4	763.7	8.5	6005	X70	174	562	604	0.07	203	200	0.78
30-5	762.9	8.4	5313	X70	154	546	659	0.09	482	282	0.59
30-6	764.1	8.4	5142	X70	161	515	628	0.10	979	238	0.75

The FEA-predicted burst capacities for rectangular and semi-ellipsoid idealizations, i.e. P_{FEA}^{Rec} and P_{FEA}^{Se}, respectively, are summarized in Table 2.4, together with the actual burst capacities from tests. The large values of mean (1.87 and 1.59) and COV (47% and 42%) of P_{test}/P_{FEA}^{Rec} and P_{test}/P_{FEA}^{Se} are due primarily to very low predicted burst capacities for specimens 16-7, 30-3, 30-4 and 30-6. It is observed that *d/t* values corresponding to these specimens are all greater than 70%. These results suggest that the rectangular and semi-ellipsoidal idealizations are overly conservative for naturally-occurring corrosion defects with the maximum depth greater than 70% of the pipe wall thickness. This limitation is however of little practical concern as a corrosion defect with *d/t* greater than 70% will typically trigger immediate mitigation actions regardless of the burst capacity of the pipeline at the defect.

Table 2.4 FEA-predicted burst capacities for rectangular and semi-ellipsoid idealizations and the actual burst capacities for the full-scale pipe specimens

Specimen ID	P_{test}(MPa)	P_{FEA}^{Rec} (MPa)	P_{FEA}^{Se} (MPa)	P_{test}/P_{FEA}^{Rec}	P_{test}/P_{FEA}^{Se}
16-1	14.60	13.43	14.92	1.09	0.98
16-6	12.72	11.91	13.31	1.07	0.96
16-7	12.84	3.21	4.19	3.99	3.06
24-1	14.21	12.69	13.34	1.12	1.06
24-2	14.37	11.56	12.51	1.24	1.15
30-1	12.31	7.06	8.72	1.74	1.41
30-2	14.10	10.05	11.30	1.40	1.25
30-3	14.78	6.80	8.53	2.17	1.73
30-4	12.48	5.62	7.15	2.22	1.74
30-5	12.26	8.01	8.88	1.53	1.38
30-6	12.96	4.42	4.75	2.94	2.73
Mean				1.87	1.59
COV				47%	42%
Mean (excluding 16-7, 30-3, 30-4 and 30-6)				1.31	1.17
COV (excluding 16-7, 30-3, 30-4 and 30-6)				18%	15%

By excluding specimens 16-7, 30-3, 30-4 and 30-6, the corresponding mean and COV of the test-to-predicted ratios are also summarized in Table 4. The results indicate that the semi-ellipsoidal idealization is on average a more accurate approximation of naturally-occurring defects than the rectangular idealization, with mean values of P_{test}/P_{FEA}^{Se} and $P_{test}\,/\,P_{FEA}^{Rec}$ equal to 1.17 and 1.31, respectively. Furthermore, the variability of the predictions corresponding to the semi-ellipsoidal idealization is slightly lower than that corresponding to the rectangular idealization, with COV values of $P_{test}\,/\,P_{FEA}^{Se}$ and P_{test}/P_{FEA}^{Rec} equal to 15% and 18%, respectively.

2.4 Effects of defect width on burst capacity

Given the results described in Section 2.3, extensive parametric 3D FEA based on the semi-ellipsoidal idealization of the corrosion defect is carried out to investigate the defect width effect on the burst capacity.

2.4.1 Analysis cases

The parametric FEA includes a total of 156 analysis cases, all of which have D = 610 mm and t = 7.1 mm, and are made of the X65 steel with the specified minimum yield and tensile strengths (SMYS and SMTS) equal to 448 and 531 MPa, respectively. Each analysis case contains a single semi-ellipsoidal corrosion defect with the defect depth (d/t) equal to 0.3, 0.45 or 0.6, normalized defect length $l^2/(Dt)$ equal to 2, 5, 15, 20, 30, 40, 50 or 60, and width-to-length ratio (w/l) equal to 0.25, 0.5, 0.75, 1, 1.25, 1.5, 1.75 or 2. The maximum w/l value considered in FEA is 2 for $l^2/(Dt)$ = 2 and 5, and 1.5 for the other values of $l^2/(Dt)$. Note that $l^2/(Dt)$ is commonly employed in semi-empirical burst capacity models, e.g. the B31G, B31G Modified and DNV models, as a dimensionless measure of the defect length and also adopted in the present study. Note further that $l^2/(Dt)$ = 20 is used to distinguish between short and long defects in the B31G model. For the particular values of D (= 610 mm) and t (= 7.1 mm) considered in FEA, the defect length is approximately 93 and 510 mm corresponding to, respectively, the lower and upper bounds of $l^2/(Dt)$ (i.e. 2 and 60) considered in the analysis. The specific values of d/t, $l^2/(Dt)$ and w/l for each analysis case are summarized in Table B.1 of Appendix B. The power-law stress-strain relationship expressed by Eq. (2.1) is employed in the FEA, with σ_y assumed to equal SMYS. The values of n and K in Eq. (2.1) are determined using Eqs. (2.3) and (2.4), respectively, with σ_u = SMTS. The FEA-predicted burst capacities for all the analysis cases are given in Table B.1 of Appendix B.

2.4.2 Analysis results

Figure 2.4 depicts the width effect on the burst capacity for given defect depth and length. To effectively demonstrate the width effect, the vertical axis in each of Figs. 2.4(a) through 2.4(h) is defined as the ratio between the burst capacity of a given analysis case i, P_i, and that of the corresponding base case for i, $P_{b\text{-}i}$, whereby the base case for i is defined as the analysis case that has the same d/t and $l^2/(Dt)$ as i but a fixed $w/l = 0.25$, i.e. the lowest w/l value considered in the parametric analysis. A quick glance of Fig. 2.4 may lead to the observation that deep defects have higher burst capacities than shallow defects. This is however a misinterpretation of the figure due to that relative (as opposed to absolute) burst capacities are plotted. Figure 2.4 indicates that for given defect depth and length, the burst capacity consistently increases as w/l increases from 0.25 to 1.5 (or 2.0 for cases shown in Figs. 2.4(a) and 2.4(b)). The width effect is marked for deep, relatively short defects as shown in Figs. 2.4(a) and 2.4(b): the burst capacity increases by about 15% as w/l increases from 0.25 to 2.0 for defects with $d/t = 0.6$ and $l^2/(Dt) = 2$ and 5. For very long defects, i.e. $l^2/(Dt) = 50$ and 60, the width effect is marginal regardless of the defect depth: the increase in the burst capacity is about 5% or less as w/l increases from 0.25 to 1.5. For $15 \leq l^2/(Dt) \leq 40$, the width effect on the burst capacity is about 5-7% for $d/t = 0.3$, and about 6-10% for $d/t = 0.45$ and 0.6. The above observations suggest that the generally beneficial defect width effect on the burst capacity, particularly for deep, relatively short defects, should be accounted for in the burst capacity model. This has been investigated in Chapter 3.

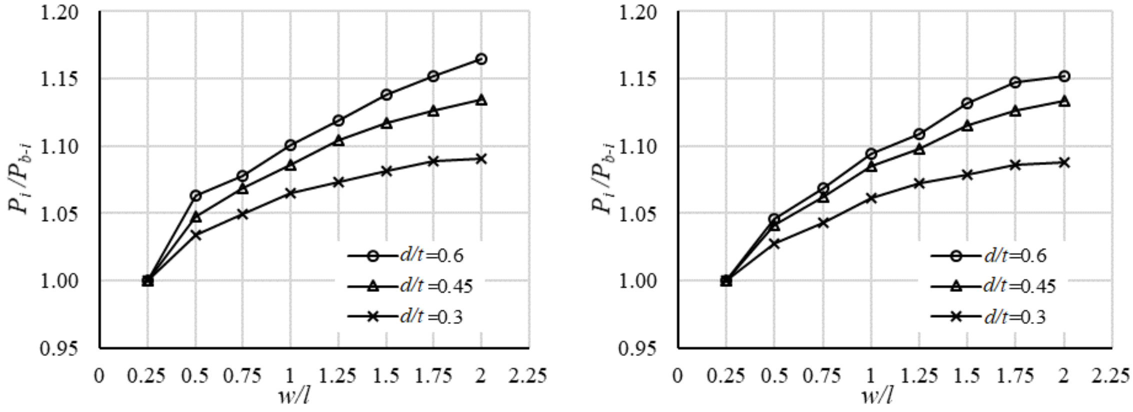

(a) $l^2/(Dt)=2$ (b) $l^2/(Dt)=5$

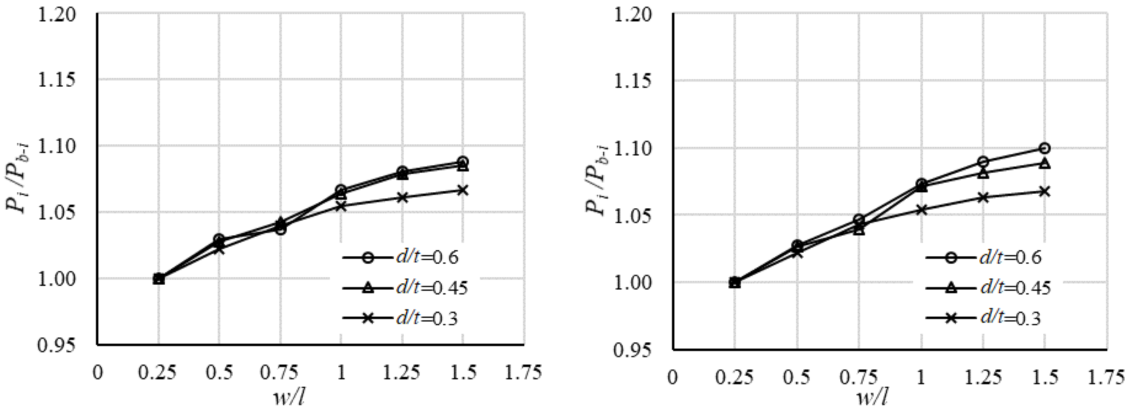

(c) $l^2/(Dt)$=15

(d) $l^2/(Dt)$=20

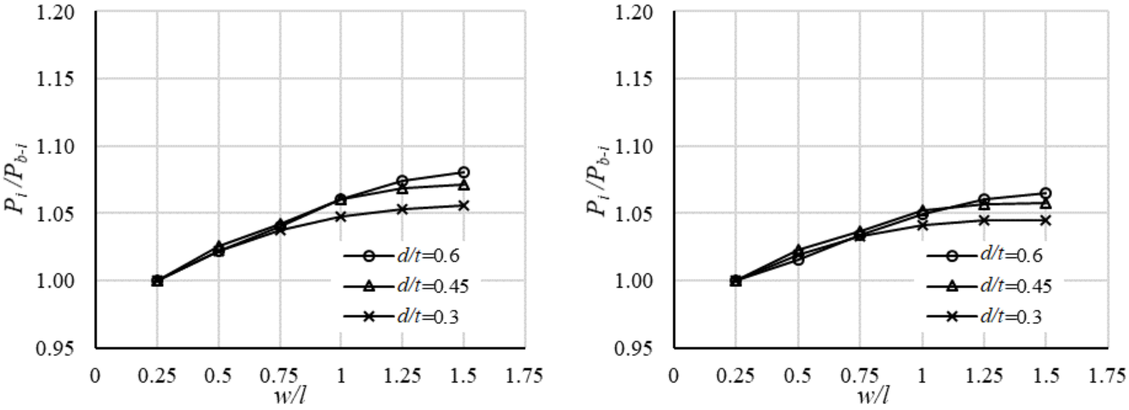

(e) $l^2/(Dt)$=30

(f) $l^2/(Dt)$=40

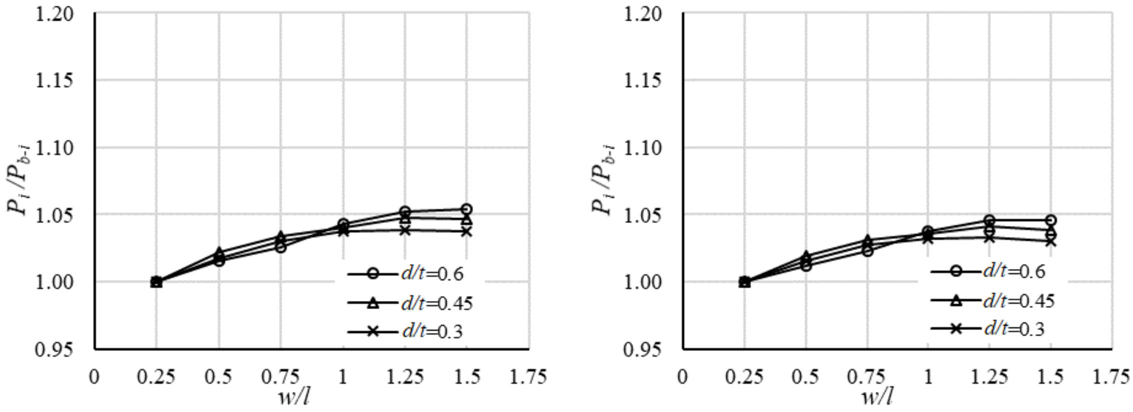

(g) $l^2/(Dt)$=50

(h) $l^2/(Dt)$=60

Figure 2.4 Width effect on the burst capacity of pipelines containing semi-ellipsoidal corrosion defects

The defect width effect on the burst capacity as depicted in Fig. 2.4 is somewhat counterintuitive and opposite to the findings reported in the literature (Tan and Xiao, 2006; Netto, 2009; Chen et al., 2015; Su et al., 2016; Shuai et al., 2017), i.e. the burst capacity decreases as the defect width increases. Note that the rectangular idealization of the corrosion defect is employed in (Tan and Xiao, 2006; Netto, 2009; Chen et al., 2015; Su et al., 2016; Shuai et al., 2017), whereas the present study employs the semi-ellipsoidal idealization. The underlying mechanisms resulting in the opposite width effects reported in the literature and observed in the present study are explained in the following. Two types of stress exist in the vicinity of a corrosion defect on a thin-walled pipeline under internal pressure: the membrane and bending stresses (Stephens et al, 1995). The membrane stress results from equilibrium with the external loads, i.e. the internal pressure, whereas the bending stress is caused by discontinuities, i.e. the change in the wall thickness at the corrosion defect. Since the bending stress is due to the local discontinuity, the bend stresses at locations more distant from the discontinuity are smaller (Stephens et al, 1995).

Corrosion defects idealized as semi-ellipsoidal-shaped exhibit a gradual loss of the wall thickness from the edge of the defect to center of the defect, i.e. the point of the maximum defect depth (Fig. 2.1(b)). The centre of a semi-ellipsoidal defect is also the point where the maximum von Mises stress occurs at a given internal pressure. This is consistent with observations of the point of failure obtained from full-scale burst tests of pipe specimens containing semi-ellipsoidal-shaped defects (Al-Owaisi, 2018). Due to this gradual change of the wall thickness, the bending stress at the defect centre as a result of the edge discontinuity is relatively small, and becomes even smaller as the defect width increases. The above explanation is illustrated by the FEA results for four representative analysis cases with d/t=0.6, $l^2/(Dt)$=2 and w/l = 0.5, 1, 1.5 and 2, respectively, at a fixed internal pressure of 9.5 MPa. For each of the four cases, the true nodal hoop stresses through the remaining ligament at the defect centre (Fig. 2.5(a)) are extracted and displayed in Fig. 2.5(b). Figure 2.5(b) indicates that the hoop stress distribution through the remaining ligament at the same internal pressure becomes more uniform as w/l increases from 0.5 to 2, which suggests less bending contribution to the hoop stress as the defect width increases. Figure 2.5(c) depicts the true hoop, axial and von Mises stresses at node A (see Fig. 2.5(a)) in the four analysis cases, which indicates that the nodal hoop stress decreases as w/l increases. Since the hoop stress is the dominant stress component for a thin-walled pipe under internal pressure, the corresponding von Mises stress decreases as w/l increases, although the axial stress increases somewhat as w/l increases. The decrease in the von

Mises stress at a given pressure results in the increase in the burst capacity according to the burst criterion employed in the present study (see Section 2.2.2). Figures 2.6(a) through 2.6(d) depict contours of the true von Mises stress within the defect (on the pipe external surface) for w/l = 0.5, 1, 1.5 and 2, respectively, which clearly show that the maximum von Mises stress occurs at the centre of the defect.

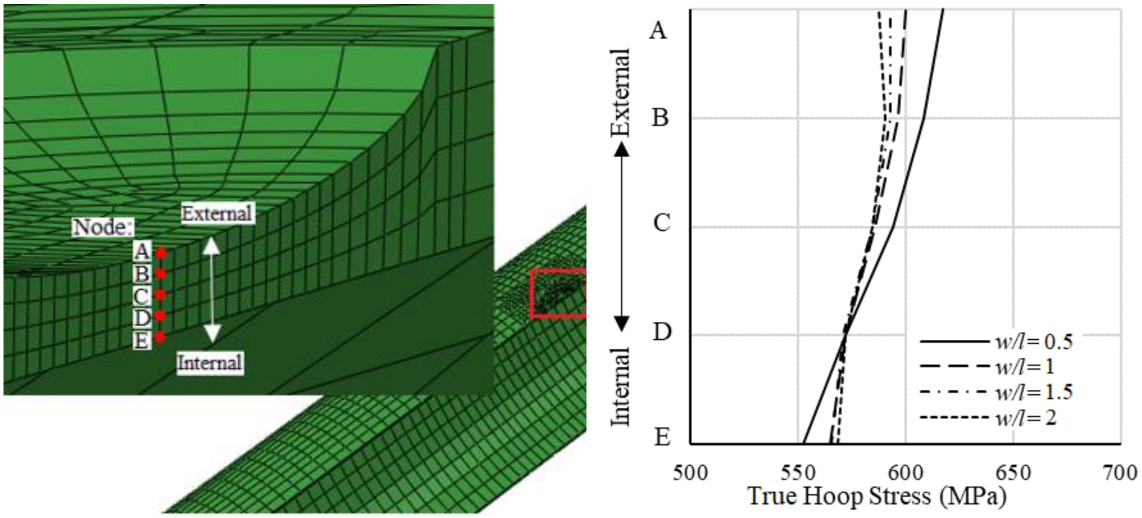

(a) Nodal path for stress extraction at the remaining ligament

(b) Distribution of true hoop stress over the remaining ligament

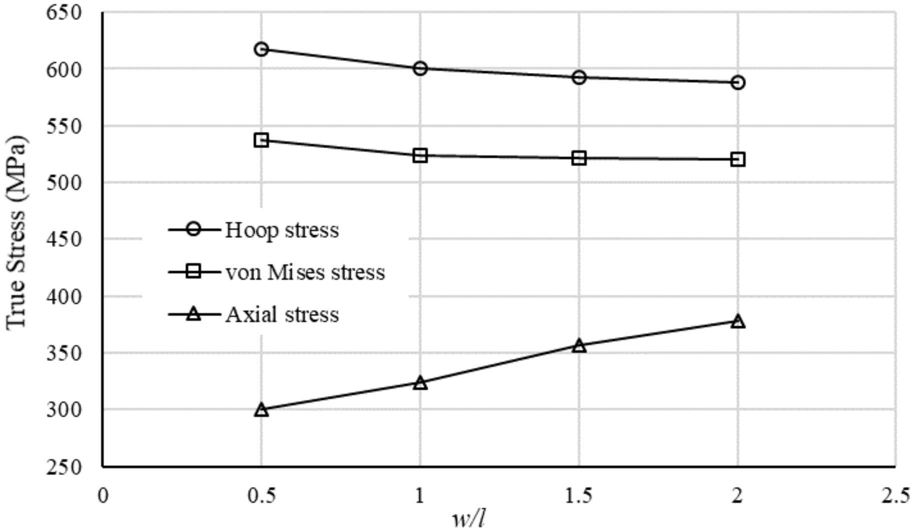

(c) True hoop, axial and von Mises stresses at node A as a function of w/l

Figure 2.5 Defect width effects on the stress field for analysis cases containing semi-ellipsoidal-shaped defects with d/t = 0.6, $l^2/(Dt)$ = 2 and internal pressure = 9.5 MPa

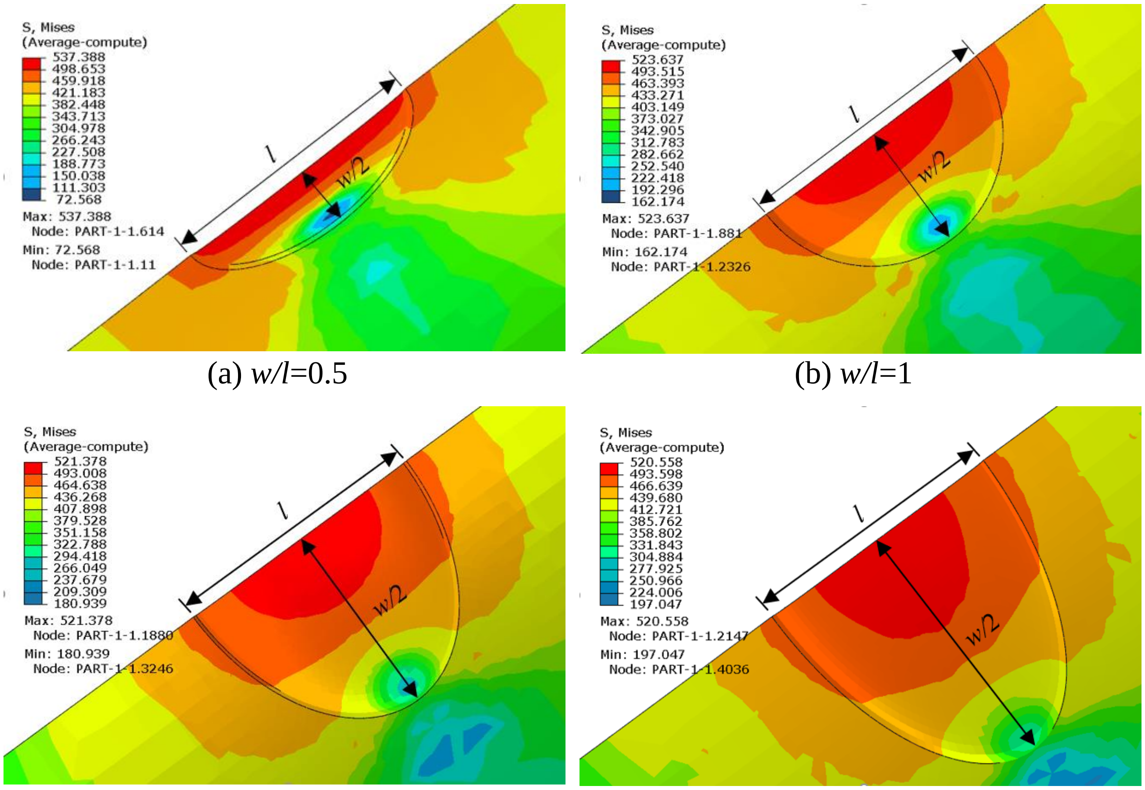

(a) *w/l*=0.5 (b) *w/l*=1

(c) *w/l*=1.5 (d) *w/l*=2

Figure 2.6 Contours of the von Mises stress for analysis cases containing semi-ellipsoidal-shaped defects with d/t = 0.6, $l^2/(Dt)$ = 2 and internal pressure = 9.5 MPa

For corrosion defects idealized as rectangular-shaped, the abrupt change in the wall thickness represents a significant discontinuity, especially for deep defects. Significant bending stresses exist at the remaining ligament close to the defect edge and are not influenced by the defect width. The maximum von Mises stress at a given pressure occurs close to the edge of the defect (as opposed to the defect centre). This is consistent with observations of the point of failure obtained from full-scale burst tests of pipe specimens containing rectangular-shaped defects (Al-Owaisi, 2018). As the defect width increases, the constraint from the surrounding defect-free regions of the pipe wall is weakened, which results in an increase in the membrane stress in the defect. The above explanation is illustrated by FEA results for the same four analysis cases as shown in Figs. 2.5 and 2.6 at the same internal pressure of 9.5 MPa, except that the defects are modeled as rectangular-shaped in FEA. For each of the four cases, the true nodal hoop stresses through the remaining ligament at the defect edge (Fig. 2.7(a)) are extracted and displayed (Fig. 2.7(b)). Figure 2.7(b) suggests that the bending component of the nodal hoop stress remains more or less the same as *w*/*l* increases, given that the four stress distribution curves are more or less parallel. On the other hand, the membrane component of the hoop stress slightly increases, reflected from the increase in the average hoop stress over the remaining ligament, as *w*/*l* increases. Figure 2.7(c) depicts the true hoop, axial and von Mises stresses at node A (see Fig. 2.7(a)) in the four analysis cases. The figure indicates that the hoop and axial stresses slightly increase as *w*/*l* increases, which results in a corresponding slightly increase in the von Mises stress. Figures 2.8(a) through 2.8(d) depict contours of the true von Mises stress within the defect (on the pipe external surface) for the four analysis cases, which shows that the maximum von Mises stress occurs at the edge of the defect.

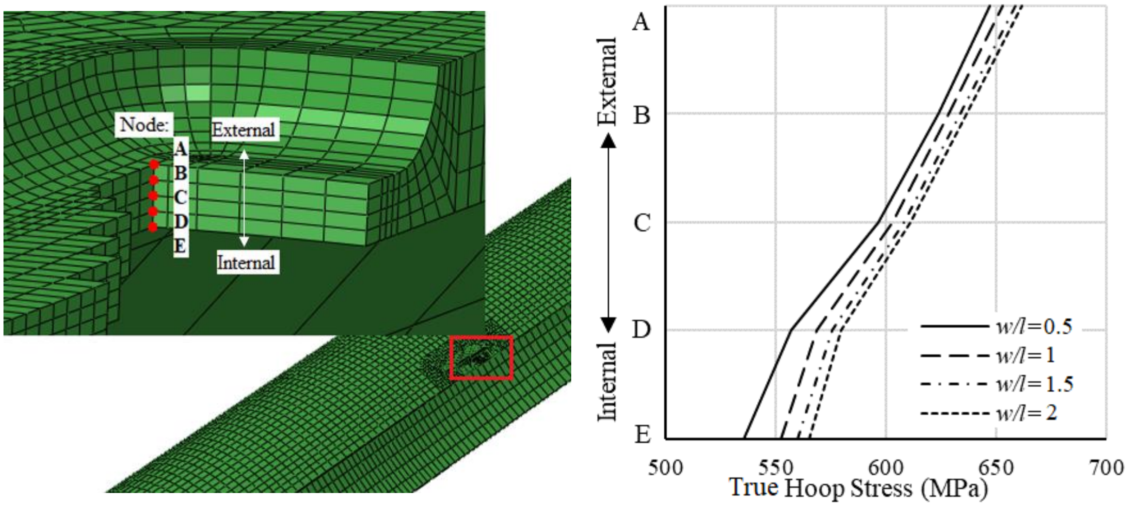

(a) Nodal path for stress extraction at the remaining ligament

(b) Distribution of true hoop stress over the remaining ligament

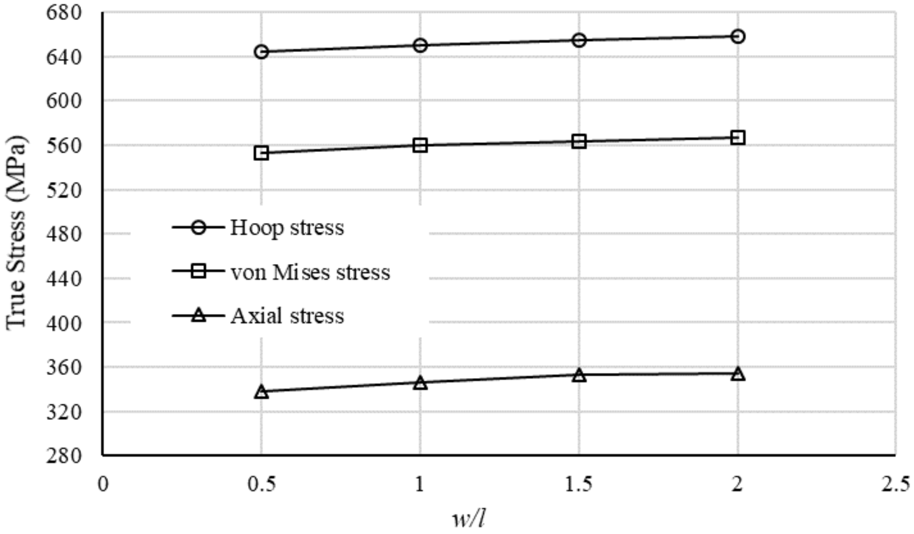

(c) True hoop, axial and von Mises stresses at node A as a function of *w*/*l*

Figure 2.7 Defect width effects on the stress field for analysis cases containing rectangular-shaped defects with *d/t* = 0.6, $l^2/(Dt)$ = 2 and internal pressure = 9.5 MPa

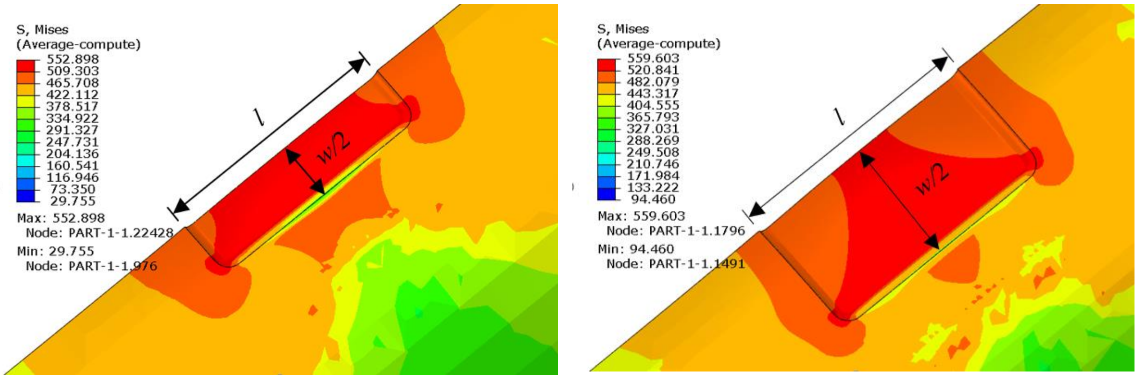

(a) *w/l*=0.5

(b) *w/l*=1

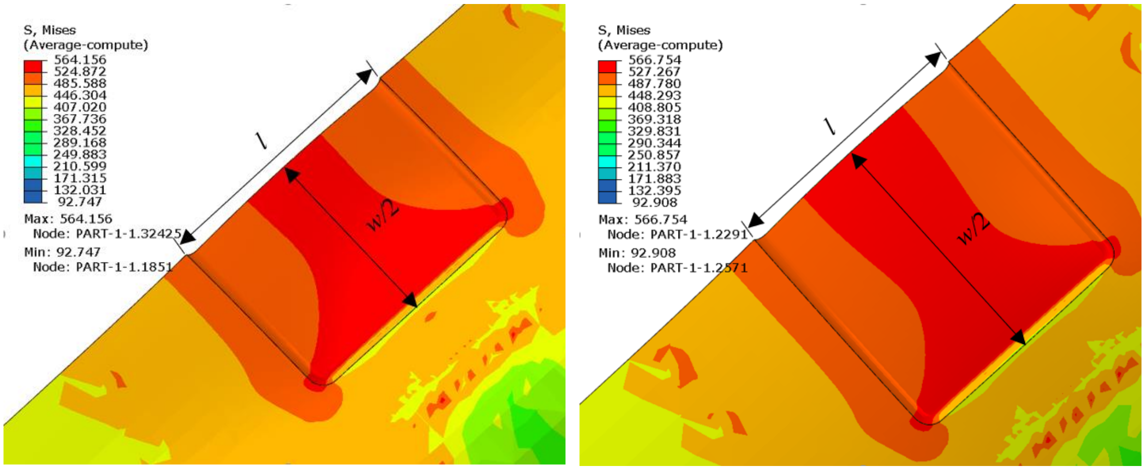

(c) *w*/*l*=1.5 (d) *w*/*l*=2

Figure 2.8 Contours of the von Mises stress for analysis cases containing rectangular-shaped defects with d/t = 0.6, $l^2/(Dt)$ = 2 and internal pressure = 9.5 MPa

2.5 Conclusions

The study in this chapter is focused on the prediction of burst capacities of corroded pipelines using 3D elasto-plastic FEA. Both rectangular and semi-ellipsoidal idealizations of corrosion defects in FEA are considered. The accuracy of the FE model and failure criterion adopted in the analysis are validated by comparing FEA-predicted burst capacities with corresponding test results for full-scale pipe specimens containing rectangular and semi-ellipsoidal defects reported in the literature. Full-scale burst test results of eleven pipe specimens containing naturally-occurring corrosion defects are then used to examine implications of the rectangular and semi-ellipsoidal idealizations for the FEA-based burst capacity prediction. It is observed that both idealizations lead to overly conservative predictions for naturally-occurring defects with $d/t \geq 0.7$. For defects with $d/t < 0.7$, the rectangular and semi-ellipsoidal idealizations lead to on average 31 and 17% under-predictions, respectively, of the burst capacity. Furthermore, the COV (15%) of the predictions corresponding to the semi-ellipsoidal idealization is slightly lower than that (18%) corresponding to the rectangular idealization.

Extensive parametric FEA is carried out to investigate the defect width effect on the burst capacity of corroded pipelines by employing the semi-ellipsoidal defect idealization. It is observed that the burst capacity increases as the defect width increases, all else remaining the same. The width effect is the strongest for deep, relatively short defects: the burst capacity increases by about 15% as w/l increases from 0.25 to 2 for a defect with $d/t = 0.6$ and $l^2/(Dt) = 2$. For long defects with $w/l \leqslant 1.5$, the width effect is marginal regardless of the defect depth. For moderately long defects with $w/l \leqslant 1.5$, the width effect can lead to 5-10% increase of the burst capacity depending on the defect depth. The width effect observed in the present study is opposite to that reported in the literature, which idealizes corrosion defects as rectangular-shaped. The underlying mechanisms for the width effects reported in the present study and literature are explained by considering the contributions of the membrane and bending components to the hoop stress in the defect region. The findings of the present study suggest that the width effect is significant and beneficial for deep, relatively short corrosion defects, and therefore should be appropriately accounted for in the empirical burst capacity models for corroded pipelines.

References

Al-Owaisi, S. S., Becker, A. A., & Sun, W., 2016. Analysis of shape and location effects of closely spaced metal loss defects in pressurised pipes. *Engineering Failure Analysis, 68,* 172-186.

Al-Owaisi, S., Becker, A. A., Sun, W., Al-Shabibi, A., Al-Maharbi, M., Pervez, T., & Al-Salmi, H., 2018. An experimental investigation of the effect of defect shape and orientation on the burst pressure of pressurised pipes. *Engineering Failure Analysis, 93,* 200-213.

ASME, 1991. “Manual for determining the remaining strength of corroded pipelines- a supplement to ASME B31 code for pressure piping”, The American Society of Mechanical Engineers, New York.

Bao, J., Zhang, S., Zhou, W., & Zhang, S., 2018. Evaluation of Burst Pressure of Corroded Pipe Segments Using Three-Dimensional Finite Element Analyses. In *2018 12th International Pipeline Conference* (pp. V001T03A043-V001T03A043). American Society of Mechanical Engineers.

Benjamin, A. C., de Andrade, E. Q., Jacob, B. P., Pereira, L. C., & Machado, P. R., 2006.

Failure behavior of colonies of corrosion defects composed of symmetrically arranged defects. In *2006 International Pipeline Conference* (pp. 417-432). American Society of Mechanical Engineers.

Chen, Y., Zhang, H., Zhang, J., Li, X., & Zhou, J., 2015. Failure analysis of high strength pipeline with single and multiple corrosions. *Materials & Design, 67*, 552-557.

Chiodo, M. S., & Ruggieri, C., 2009. Failure assessments of corroded pipelines with axial defects using stress-based criteria: numerical studies and verification analyses. *International Journal of Pressure Vessels and Piping, 86*(2-3), 164-176.

Choi, J. B., Goo, B. K., Kim, J. C., Kim, Y. J., & Kim, W. S., 2003. Development of limit load solutions for corroded gas pipelines. *International Journal of Pressure Vessels and Piping, 80*(2), 121-128.

Chouchaoui, B., 1995. Evaluating the remaining strength of corroded pipelines, PhD thesis, University of Waterloo.

Cronin, D. S., 2000. Assessment of corrosion defects in pipelines, PhD thesis, University of Waterloo.

Canadian Standard Association, (CSA), 2019. Oil and gas pipeline systems. CSA standard Z662-19. *Mississauga, Ontario, Canada*.

Dassault Systèmes, D. S., 2016. *Abaqus analysis user's guide*. Technical Report Abaqus 2016 Documentation, Simulia Corp.

Det Norske Veritas (DNV), 2017. “Recommended practice DNV-RP-F101, corroded pipelines”, Hovic, Norway

Dowling, N. E., 2007. Mechanical behavior of materials. Prentice Hall, New Jersey

Fekete, G., & Varga, L., 2012. The effect of the width to length ratios of corrosion defects on the burst pressures of transmission pipelines. *Engineering Failure Analysis, 21*, 21-30.

Keshtegar, B., & Seghier, M. E. A. B., 2018. Modified response surface method basis harmony search to predict the burst pressure of corroded pipelines. *Engineering Failure Analysis, 89*, 177-199.

Kiefner, J. and Vieth, P., 1989. “A modified criterion for evaluating the remaining strength of corroded pipe, Final Report on Project PR 3-805”, Battelle Memorial Institute, Columbus, OH, 1989.

Kiefner, J. and Vieth, P., 1990. “PC program speeds new criterion for evaluating corroded pipe”, Oil and Gas Journal, August 20, 1990. pp. 91-93.

Leis, B. N., & Stephens, D. R., 1997a. An alternative approach to assess the integrity of corroded line pipe-part I: current status. In *The Seventh International Offshore and Polar Engineering Conference*. International Society of Offshore and Polar Engineers. *ISBN 1-880653-28-1 (Set); ISBN 1-880653-32-X (Vol. IV),* 624-634.

Leis, B. N., & Stephens, D. R., 1997b. An alternative approach to assess the integrity of corroded line pipe-part II: Alternative criterion. In *The Seventh International Offshore and Polar Engineering Conference*. International Society of Offshore and Polar Engineers. *ISBN 1-880653-28-1 (Set); ISBN 1-880653-32-X (Vol. IV),* 635-641.

Mokhtari, M., & Melchers, R. E., 2018. A new approach to assess the remaining strength of corroded steel pipes. *Engineering Failure Analysis, 93*, 144-156.

Mokhtari, M., & Melchers, R. E., 2019. Next-generation fracture prediction models for pipes with localized corrosion defects. *Engineering Failure Analysis, 105*, 610-626.

Netto, T. A., 2009. On the effect of narrow and long corrosion defects on the collapse pressure of pipelines. *Applied Ocean Research, 31*(2), 75-81.

Shuai, Y., Shuai, J., & Xu, K., 2017. Probabilistic analysis of corroded pipelines based on a new failure pressure model. *Engineering Failure Analysis*, 81, 216-233.

Stephens, D. R., Bubenik, T. A., & Francini, R. B., 1995. Residual strength of pipeline corrosion defects under combined pressure and axial loads. Final report (No. AGA-

96005964). Battelle, Columbus, OH (United States).

Stephens, D. R., & Leis, B. N., 2000. Development of an alternative criterion for residual strength of corrosion defects in moderate-to high-toughness pipe. In *2000 3rd International Pipeline Conference* (pp. V002T06A012-V002T06A012). American Society of Mechanical Engineers.

Su, C. L., Li, X., & Zhou, J., 2016. Failure pressure analysis of corroded moderate-to-high strength pipelines. *China Ocean Engineering*, *30*(1), 69-82

Tan, K. R. and Xiao, X., 2006. Analysis on limit load of corroded submarine pipelines, *The Ocean Engineering*, *24*(3): 63-67. (in Chinese)

Wang, L., & Zhang, Y., 2011. Plastic collapse analysis of thin-walled pipes based on unified yield criterion. *International Journal of Mechanical Sciences*, *53*(5), 348-354.

Zhu, X. K., & Leis, B. N., 2004. Strength criteria and analytic predictions of failure pressure in line pipes. *International Journal of Offshore and Polar Engineering, 14*(02), 125-131.

Zhu, X. K., & Leis, B. N., 2005. Influence of yield-to-tensile strength ratio on failure assessment of corroded pipelines. *Journal of Pressure Vessel Technology, 127*(4), 436-442.

3 Development of a Burst Capacity Model for Corroded Pipelines Considering Corrosion Defect Width and a Revised Folias Factor Equation

3.1 Introduction

Metal-loss corrosion defects threaten the structural integrity of oil and gas pipelines as they cause thinning of the pipe wall and therefore reduce the pressure containment capacity, i.e. burst capacity, of the pipeline. Pipeline operators routinely carry out high-resolution inline inspections (ILI) of pipelines to detect and size corrosion defects. Based on the ILI information, semi-empirical models are commonly used to evaluate the burst capacity of corroded pipelines, for example, the well-known B31G (1991), B31G Modified (Kiefner and Vieth, 1989), CSA (2019), DNV (2017), RSTRENG (Kiefner and Vieth, 1990) and SHELL92 (Ritchie and Last, 1995) models, to support the decision-making for potential corrosion mitigation actions. All of the above-indicated burst capacity models are based on the flow stress-dependent component of the NG-18 equation (Kiefner, 1969), which expresses the burst capacity as a function of the material flow stress (σ_f), Folias (bulging) factor (M) and extent of the metal-loss within the corrosion defect, in addition to the basic geometric properties of the pipeline such as the outside diameter (D) and wall thickness (t).

The flow stress was considered in (Hahn et al., 1969) to lie between the yield and tensile strengths for strain-hardening materials. Various empirical definitions of the flow stress have been adopted in the NG-18-family models, with each definition suitable for a certain range of the pipe steel grades. These definitions do not rigorously characterize the material strain hardening effect. The equations to evaluate the Folias factor adopted in the NG-18-family models are based on Folias's theoretical analysis (Folias, 1964, 1965) for pipes containing through-wall thickness cracks, and a function of the defect length (i.e. in the pipe longitudinal direction). To more accurately account for the bulging effect associated with a part-through wall corrosion defect, the Folias factor should depend on the defect length as well as the defect depth (in the pipe through wall thickness direction). The extent of the metal-loss within a corrosion defect is characterized in the NG-18-family models based on the river-bottom concept (Fig. 3.1). By connecting the deepest points within the defect, a river-bottom path is constructed first and then projected onto a longitudinal plane perpendicular to the pipe wall to generate the river-bottom profile of the defect. The extent of the metal-loss is then characterized by the area of the river-bottom profile. Different approaches and idealizations are employed to evaluate the area of the river-bottom profile as summarized in Section 3.2. For example, the B31G model idealizes the river-bottom profile as a parabola. It follows that the area of the profile equals $2/3dl$, where d and l are the maximum depth and length of the profile, respectively. Through the river-bottom profile, a three-dimensional (3D) corrosion defect is converted to a two-dimensional (2D) defect; therefore, the width of the corrosion defect is ignored in the NG-18-family models. Parametric 3D FEA results reported in (Zhang and Zhou, 2020) show that the width of idealized semi-ellipsoidal-shaped corrosion defects can have a markedly beneficial effect on the burst capacity, especially for deep, relatively short defects. Therefore, the defect width should be incorporated into the semi-empirical burst capacity models to improve their predictive accuracy.

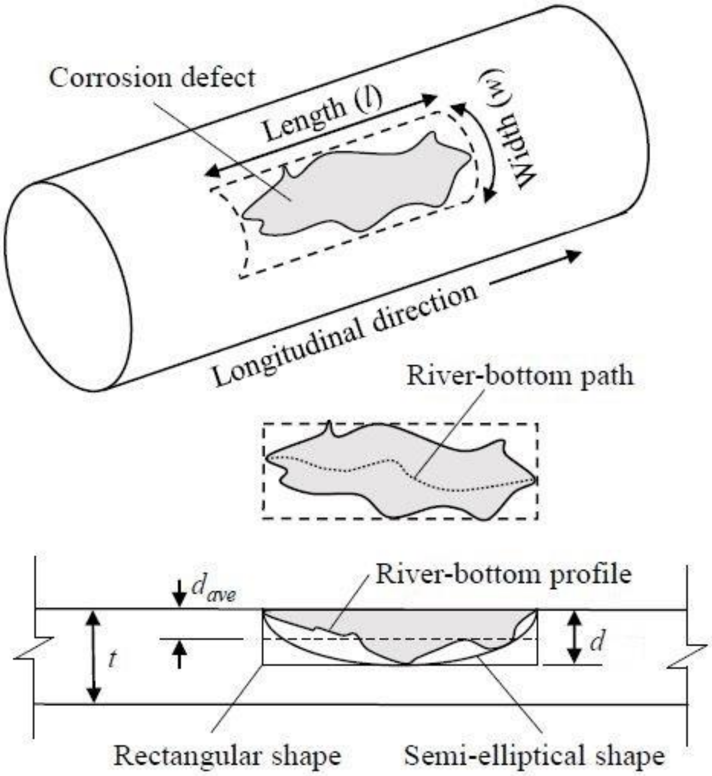

Figure 3.1 Typical corrosion defect on pipeline

New burst capacity models for corroded pipelines have been reported in the recent literature. Sun et al. (2020) proposed an NG-18-type burst capacity model by incorporating a new definition of the flow stress and a revised equation for the Folias factor. Based on an analytical burst capacity model for defect-free thin-walled pipes proposed in (Leis et al., 2016), the flow stress is defined in (Sun et al., 2020) as a function of the strain hardening exponent and ultimate tensile strength of the pipe steel. The Folias factor equation in (Sun et al., 2020) depends on the defect length and depth, and is developed by curve-fitting burst capacities of corroded pipeline (corrosion defects idealized as rectangular-shaped) predicted by elasto-plastic finite element analyses (FEA). It is noted that Sun et al.'s model does not take into account the defect width. The burst capacity models reported in (Netto, 2010; Chen et al., 2015; Su et al., 2016; Shuai et al., 2017; Keshtegar and Seghier, 2018) include the defect width as a model parameter. The extent to which the defect width influences the burst capacity however varies markedly among the models.

The objective of the present chapter is to develop a new burst capacity model for corroded pipeline based on a large number of parametric elasto-plastic FEA validated by full-scale tests. The proposed model follows the basic form of the NG-18 equation but incorporates the defect width as an input parameter in the model, a new Folias factor equation that depends on both the defect depth and length and the same flow stress definition as in (Sun et al., 2020). The model is novel compared with the recently-developed burst capacity models in the literature in that it addresses all three key aspects of the NG-18-family model, i.e. the flow stress, Folias factor and characterization of the extent of the metal loss. The rest of this chapter is organized as follows: Section 3.2 briefly reviews how the flow stress, Folias factor and extent of metal loss are evaluated in six well-known NG-18-family models, i.e. the B31G, B31G Modified, CSA, DNV, RSTRENG and the model recently proposed by Sun et al. (2020); details of the proposed burst capacity model are described in Section 3.3, and Section 3.4 presents the validation of the proposed model and its comparison with the above-mentioned seven existing models, followed by conclusions in Section 3.5.

3.2 Review of NG-18-based burst capacity models

The model for predicting the failure stress of thin-walled pipes containing surface flaws evolves from fracture mechanics considerations for flat plates, with modifications for the bulging effect and high toughness of line pipe materials (Kiefner, 1969). The flow stress-dependent criterion of the NG-18 equation for predicting the failure stress of pressurized pipe containing a corrosion defect is given by (Kiefner, 1969):

$$\sigma_{hb} = \sigma_f \frac{1-A/A_0}{1-\frac{A/A_0}{M}} \tag{3.1}$$

where σ_{hb} is the failure stress, i.e. the hoop stress at burst; σ_f is the material flow stress; A is the area of the river-bottom profile; $A_0 = lt$ is the reference area, and M is the Folias bulging factor. The remaining strength of the corroded pipe, i.e. its burst capacity P_b, is then given by:

$$P_b = P_0 \frac{1-A/A_0}{1-\frac{A/A_0}{M}} = \frac{2t\sigma_f}{D} \frac{1-A/A_0}{1-\frac{A/A_0}{M}} \tag{3.2}$$

where $P_0 = 2t\sigma_f/D$ is the burst capacity of the defect-free pipe. Table 3.1 summarizes seven NG-18-type bursts capacity models for corroded pipelines, including six well-knowns models (i.e. the B31G, B31G Modified (B31G-M), CSA, DNV, RSTRENG and SHELL92 models) and the model recently proposed by Sun et al. (2020). All seven models can be expressed using Eq. (3.2), albeit with different equations to evaluate σ_f, A/A_0 and M. In Table 3.1, SMYS, σ_y and σ_u denote, respectively, the specified minimum yield strength, yield strength and tensile strength of the pipe steel; n is the strain hardening exponent, and d_{ave} denotes the average depth of the river-bottom profile of the corrosion defect (Fig. 3.1). The B31G, B31G-M and RSTRENG models are applicable for $\frac{d}{t} \leq 0.8$, and the applicability limit for the DNV and SHELL92 models is $\frac{d}{t} \leq 0.85$. Note that details of the effective area method employed in RSTRENG to evaluate A/A_0 are well described in the literature, e.g. (Kiefner and Vieth, 1990; Cronin and Pick, 2000), and therefore are not presented here for brevity. Note also that the Folias factor in Sun et al.'s model is a function of the defect length and depth for relatively long defects, i.e. $l^2/(Dt) \geq 20$, but is independent of the defect depth for defects with $l^2/(Dt) < 20$.

Table 3.1 Burst pressure prediction equations in different models

Model	σ_f	*A/A*$_0$	*M*
B31G	$1.1\sigma_y$	$\frac{2d}{3t}, \frac{l^2}{Dt} \le 20$ $\frac{d}{t}, \frac{l^2}{Dt} > 20^1$	$\sqrt{1+\frac{0.8l^2}{Dt}}, \frac{l^2}{Dt} \le 20$ $\infty, \frac{l^2}{Dt} > 20$
B31G-M	$\sigma_y + 68.95$ (MPa)	$\frac{0.85d}{t}$	$\sqrt{1+0.6275\frac{l^2}{Dt}-0.003375\frac{l^4}{(Dt)^2}}, \frac{l^2}{Dt} \le 50$ $3.3+0.032\frac{l^2}{Dt}, \frac{l^2}{Dt} > 50$
DNV	σ_u	$\frac{d}{t}$	$\sqrt{1+\frac{0.31l^2}{Dt}}$
CSA	$1.15\sigma_y$ $SMYS \le 241\ MPa$ $0.9\sigma_u$ $SMYS > 241\ MPa$	$\frac{d_{ave}}{t}$	$\sqrt{1+0.6275\frac{l^2}{Dt}-0.003375\frac{l^4}{(Dt)^2}}, \frac{l^2}{Dt} \le 50$ $3.3+0.032\frac{l^2}{Dt}, \frac{l^2}{Dt} > 50$
RSTRENG	$\sigma_y + 68.95$	Effective area	$\sqrt{1+0.6275\frac{l^2}{Dt}-0.003375\frac{l^4}{(Dt)^2}}, \frac{l^2}{Dt} \le 50$ $3.3+0.032\frac{l^2}{Dt}, \frac{l^2}{Dt} > 50$
SHELL92	$0.9\sigma_u$	$\frac{d}{t}$	$\sqrt{1+\frac{0.8l^2}{Dt}}$
Sun et al.'s model	$2\left(\frac{1}{\sqrt{3}}\right)^{n+1}\sigma_u$	$\frac{d}{t}$	$\sqrt{0.39\frac{l^2}{Dt}+1}, \frac{l^2}{Dt} < 20$ $C_0\frac{L^4}{(Dt)^2}+C_1\frac{l^2}{Dt}+C_2, 20 \le \frac{l^2}{Dt} < 200$ $C_0 = -0.00032\left(\frac{d}{t}\right)^{0.676447}$ $C_1 = 0.1627\left(\frac{d}{t}\right)^{0.9721}$ $C_2 = -4.3175\left(\frac{d}{t}\right)+3.5107$ $C_1\frac{l^2}{Dt}+C_2, \frac{l^2}{Dt} \ge 200$ $C_1 = 0.0138\left(\frac{d}{t}\right)^{1.5926}$ $C_2 = 13.247\left(\frac{d}{t}\right)+2.5319$

1. The B31G model is discontinuous at $l^2/(Dt) = 20$.

3.3 Proposed burst capacity model

3.3.1 Basic equation

The basic equation of the proposed burst capacity model follows the NG-18 format with a slight modification to include the defect width effect as follows:

$$P_b = f_w\frac{2t\sigma_f}{D}\frac{1-\frac{d}{t}}{1-\frac{d}{tM}} \tag{3.3}$$

where f_w is the defect width factor to account for the impact of the defect width on the burst capacity. The definition of σ_f in Eq. (3.3) is described in Section 3.3.2. The equations to evaluate f_w and M in Eq. (3.3) are developed by curve fitting results of parametric elasto-plastic FEA reported in a recently-completed study (Zhang and Zhou, 2020). The curve fitting is conducted with MATLAB (2018). Each FEA case contains a single corrosion defect with an idealized semi-ellipsoidal shape. Details of the parametric FEA and development of f_w and M are described in Sections 3.3.3 and 3.3.4. The semi-ellipsoidal idealization of the corrosion defect implies that the A/A_0 term in the NG-18 equation should be replaced by $\pi d/(4t)$. The rationale for using $\frac{d}{t}$ as opposed to $\pi d/(4t)$ in Eq. (3.3) is two-fold. First, it is observed in FEA that the burst failure initiates at the center of the defect (Al-Owaisi et al., 2016; Zhang and Zhou, 2020), i.e. the point of the maximum defect depth. This is consistent with observations from full-scale burst tests of pipe specimens containing semi-ellipsoidal-shaped defects (Al-Owaisi, 2018). Second, the semi-ellipsoidal shape of the corrosion defect is implicitly taken into account in the equations for f_w and M.

3.3.2 Definition of flow stress considering strain hardening

The analytical solution for the burst capacity of a long thin-walled defect-free pipe has been derived by Zhu and Leis (2007), as shown in Eq. (3.4), by considering the von Mises yield criterion and power-law strain hardening response.

$$P_0 = \left(\frac{1}{\sqrt{3}}\right)^{n+1} \frac{4t}{D}\sigma_u \tag{3.4}$$

By considering $P_0 = 2t\sigma_f/D$, it immediately follows that the flow stress in Eq. (3.3) can be defined as (Sun et al., 2020):

$$\sigma_f = 2\left(\frac{1}{\sqrt{3}}\right)^{n+1} \sigma_u \tag{3.5}$$

The strain hardening exponent (n) can be estimated from σ_y/σ_u using the following empirical equation proposed in (Zhu and Leis, 2005), if the complete stress-strain relationship of the pipe steel is unavailable:

$$n = 0.239\left(\frac{1}{\sigma_y/\sigma_u} - 1\right)^{0.596} \tag{3.6}$$

The flow stress definition given by Eq. (3.5) is a function of the strain hardening exponent and ultimate tensile strength of the pipe steel. Figure 3.2 clarifies the difference between the flow stress defined per Eq. (3.5) and those defined in the B31G, B31G-M, CSA, DNV, RSTRENG, SHELL92 models as summarized in Table 3.1. In Fig. 3.2(a), σ_f/σ_y is plotted versus σ_y/σ_u, whereas σ_f/σ_u is plotted versus σ_y/σ_u in Fig. 3.2(b). For a given value of σ_y/σ_u, Eq. (3.6) is first employed to estimate n, which can then be used to evaluate σ_f/σ_y per Eq. (3.5). For the flow stress definition of $\sigma_y + 68.95$ (MPa) adopted in B31G-M and RSTRENG, three representative values of σ_y are considered in Fig. 3.2(a), i.e. 300, 400 and 500 MPa, each corresponding to a specific range of σ_f/σ_y values, i.e. 0.7-0.8, 0.75-0.85 and 0.8-0.9, respectively. Figure 3.2 indicates that the flow stress defined per Eq. (3.5) is consistently greater than those defined in the above-mentioned six burst capacity models for the range of σ_y/σ_u values typical for pipe steels. In some cases, Eq. (3.5) results in markedly greater values of the flow stress. For instance, σ_f/σ_y = 1.36 per Eq. (3.5) for $\sigma_y/\sigma_u = 0.8$, whereas $\sigma_f/\sigma_y = 1.23$, 1.17 and 1.14 for σ_y = 300, 400 and 500 MPa, respectively, per the flow stress definition in B31G-M and RSTRENG.

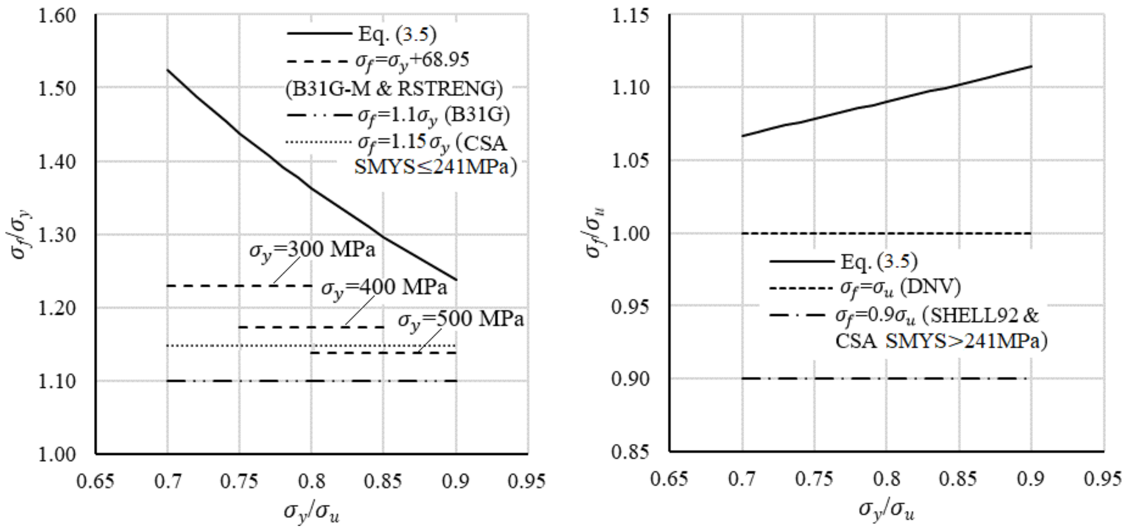

Figure 3.2 Comparison of the flow stress definitions per Eq. (3.5) and the well-known models with the range of σ_y/σ_u values typical for pipe steels

3.3.3 Folias factor *M*

In this study, a new equation of the Folias factor for corrosion defects is developed by fitting the results of the parametric FEA reported in (Zhang and Zhou, 2020), which includes a total of 156 analysis cases involving idealized semi-ellipsoidal-shaped corrosion defects on a pipe with D = 610 mm, t = 7.1 mm and a steel grade of X65 steel (SMYS = 448 MPa). Considering idealized corrosion defects in the parametric FEA is consistent with similar studies reported in the literature (Ritchie and Last, 1995; Netto, 2010; Chen et al., 2015; Su et al., 2016; Shuai et al., 2017; DNV, 2017; Keshtegar and Seghier, 2018; Sun et al., 2020). The rationale for employing semi-ellipsoidal-shaped (as opposed to rectangular-shaped) defects in the analysis is an investigation reported in (Zhang and Zhou, 2020), which compares the experimentally-observed burst capacities of 11 full-scale naturally corroded pipe specimens with the corresponding FEA-predicted burst capacities by idealizing the naturally-occurring corrosion defects as either semi-ellipsoidal or rectangular shaped. It is observed that the semi-ellipsoidal idealization leads to more accurate (less conservative and less variability) FEA-predicted burst capacities than the rectangular idealization. For a given case, the depth (d/t) of the semi-elliptical-shaped corrosion defect equals 0.3, 0.45 or 0.6; the normalized defect length $l^2/(Dt)$ equals 2, 5, 15, 20, 30, 40, 50 or 60, and the width-to-length ratio (w/l) equals 0.25, 0.5, 0.75, 1, 1.25, 1.5, 1.75 or 2. The maximum w/l value considered in FEA is 2 for $l^2/(Dt)$ = 2 and 5, and 1.5 for the other values of $l^2/(Dt)$. While the above-described analysis cases include both relatively narrow (i.e. $w/l \leq 1$) and wide (i.e. $w/l > 1$) corrosion defects, it has been reported in (Zhang and Zhou, 2020) that no abrupt change in the hoop stress, which governs the burst capacity, is observed between cases with $w/l \leq 1.0$ and those with $w/l > 1.0$ (all else being the same). It follows that there is no distinct difference between the failure behaviours of corrosion defects with $w/l \leq 1.0$ and those of defects with $w/l > 1.0$. As described in (Zhang and Zhou, 2020), the finite element model as well as failure criterion for determining the burst capacity has been validated by using 12 full-scale burst tests of pipe specimens reported in (Benjamin, 2006; Al-Owaisi, 2018), among which six pipe specimens contain semi-ellipsoidal-shaped defects with w/l = 1.0. As reported in (Zhang and Zhou, 2020), the mean and coefficient of variation (COV) of ratios of test-to-FEA predicted burst capacities are 1.00 and 2.0%, respectively.

The proposed Folias factor equation is developed based on the FEA results for the 24 analysis cases with *w/l* = 0.25. This implies that the defect width effect on the burst capacity is solely incorporated in the f_w factor in Eq. (3.3). The development of the equation for f_w is described in Section 3.3.3. Let $P_{0.25}^{FEA}$ denote the FEA-predicted burst capacity for a given case with *w/l* = 0.25. FEA is also carried out to evaluate the burst capacity of the case (P_0^{FEA}) by assuming it to be defect-free. Given $P_{0.25}^{FEA}$ and P_0^{FEA} for the analysis case, the value of the Folias factor associated with the case, M_{FEA}, can be evaluated by re-arranging Eq. (3.3) as follows:

$$M_{FEA} = \frac{\frac{d}{t}}{1-\frac{P_0^{FEA}}{P_{0.25}^{FEA}}\left(1-\frac{d}{t}\right)} \tag{3.7}$$

Implicit in Eq. (3.7) is the assumption that f_w = 1.0 for *w/l* = 0.25. The 24 FEA cases result in 24 values of M_{FEA}, corresponding to *d/t* varying from 0.3 to 0.6 and $l^2/(Dt)$ varying from 2 to 60. The following equation for the Folias factor is then developed based on the nonlinear curve fitting.

$$M = \sqrt{1 + 0.3498e^{\frac{d}{t}}\left(\frac{l^2}{Dt}\right)^{-0.01792\frac{d}{t}} + 0.24\frac{d}{t}\frac{l^2}{Dt} - 0.001993\left(\frac{d}{t}\frac{l^2}{Dt}\right)^2} \tag{3.8}$$

Figure 3.3 indicates that Eq. (3.8) fits closely the values of M_{FEA}. Figure 3.4 compares values of *M* obtained from Eq. (3.8) and the Folias factor equations summarized Table 3.1. Figure 3.4 indicates that Eq. (3.8) results in markedly lower values of *M* than all the Folias factor equations summarized in Table 3.1. Among the equations summarized in Table 3.1, the equation employed in B31G (for $l^2/(Dt) \leq 20$) and SHELL92 results in the highest *M* values, whereas the equation in the DNV model results in the lowest *M* values. A few drawbacks of the Folias factor equation in Sun et al.'s model are noted from Fig. 3.4. The equation contains a discontinuity at $l^2/(Dt) = 20$ because *M* is assumed in Sun et al.'s model to be independent of the defect depth for $l^2/(Dt) < 20$. Furthermore, the three *M* curves corresponding to *d/t* = 0.3, 0.45 and 0.6, respectively, intersect at $l^2/(Dt)$ between 25 and 30. This is anomaly caused by the particular form of the fitting equation adopted.

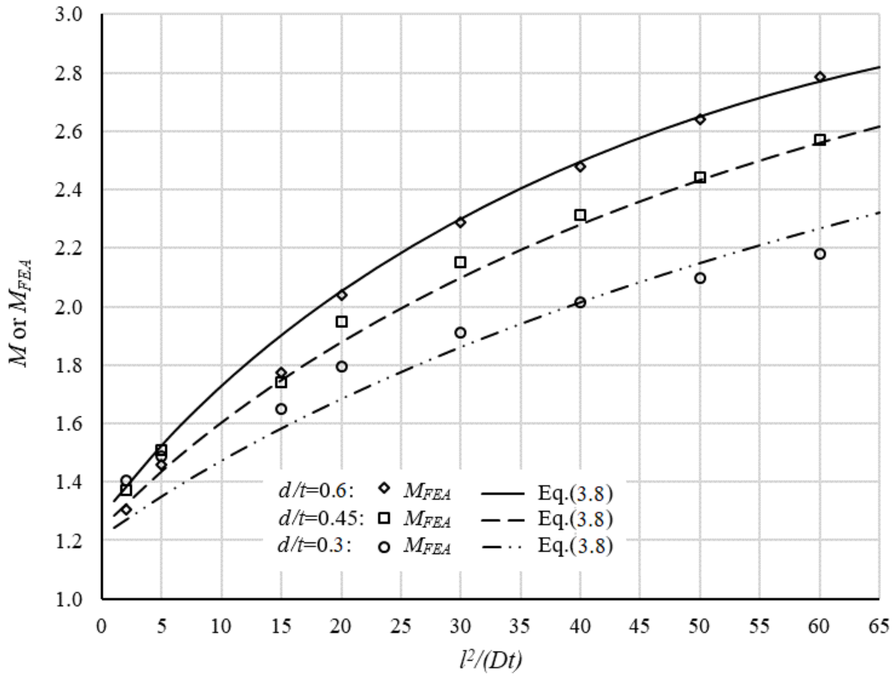

Figure 3.3 The Folias factor values per Eq. (3.8) compared with that from the FEA cases

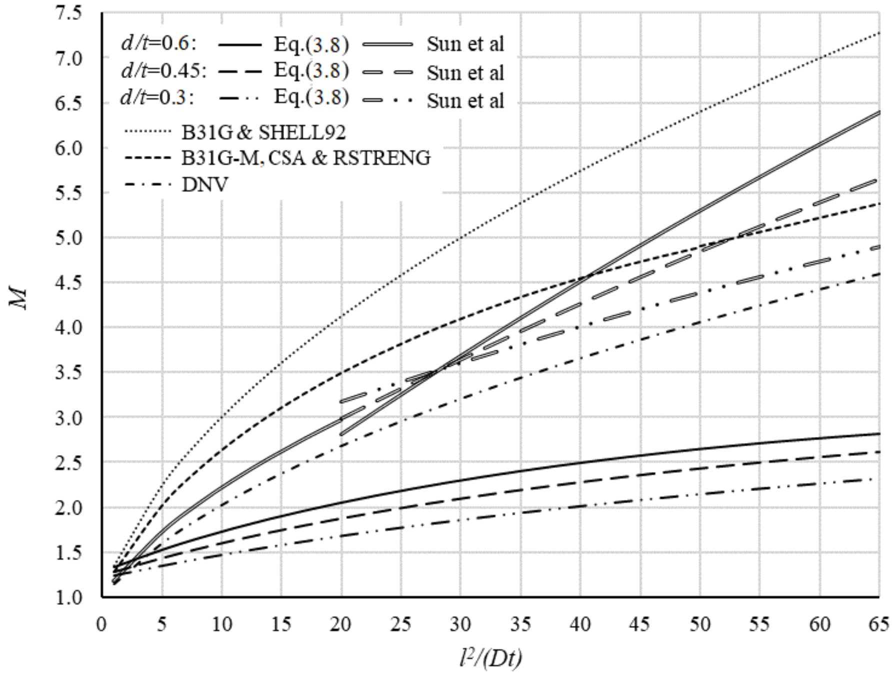

Figure 3.4 Comparison of the Folias factor per Eq. (3.8) and those summarized in Table 3.1

3.3.4 Width effect factor f_w

It is reported in (Zhang and Zhou, 2020) that for semi-ellipsoidal-shaped defects the defect width has a beneficial effect on the burst capacity, especially for deep, relatively short defects. Such a beneficial width effect is accounted for by the factor f_w in Eq. (3.3). To develop the equation for f_w, the burst capacity of a given analysis case with $w/l > 0.25$, denoted by P_b^{FEA}, is normalized by the burst capacity ($P_{0.25}^{FEA}$) of a corresponding analysis case with the same defect depth and length, but with $w/l = 0.25$. It is noted that the beneficial width effect is assumed to be negligible for $w/l \le 0.25$, i.e. $f_w = 1$ for $w/l \le 0.25$. Given the values of $f_w^{FEA} = P_b^{FEA}/P_{0.25}^{FEA}$ for the analysis cases reported in (Zhang and Zhou, 2020), the following expression for f_w is developed based on nonlinear curve fitting:

$$f_w = \begin{cases} 1 & \frac{w}{l} \le 0.25 \\ \sqrt{1 + \left[0.6215\frac{d}{t}\left(\frac{w}{l} - 0.25\right) - 0.2866\frac{d^2}{t^2}\left(\frac{w}{l} - 0.25\right)^2\right] e^{-0.01719\frac{l^2}{Dt}}} & \frac{w}{l} > 0.25 \end{cases} \tag{3.9}$$

Figure 3.5 depicts the fitting accuracy of Eq. (3.9), where f_w values obtained from Eq. (3.9) are compared with the corresponding values of f_w^{FEA}. For brevity, only the cases with $l^2/(Dt)$= 5, 20, 40 and 60 and d/t = 0.3, 0.45 and 0.6. are shown in Fig. 3.5. The fitting accuracy of Eq. (3.9) for the other cases is similar.

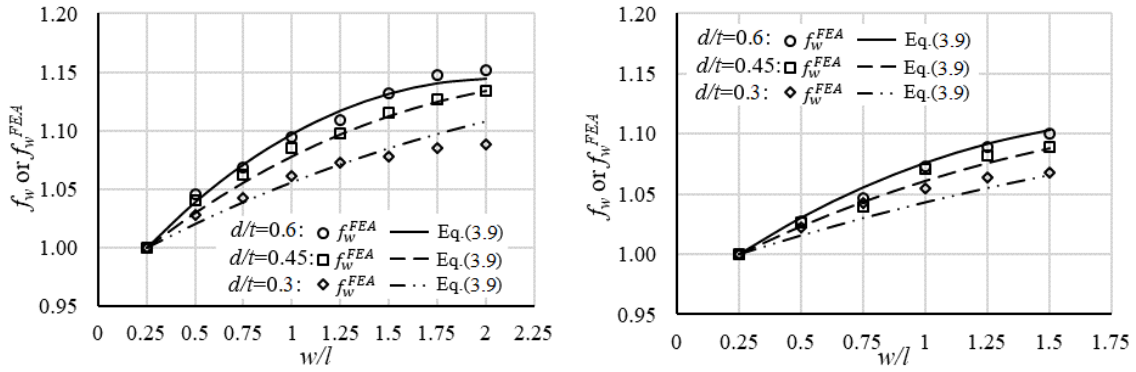

(a) $l^2/(Dt)$=5 (b) $l^2/(Dt)$=20

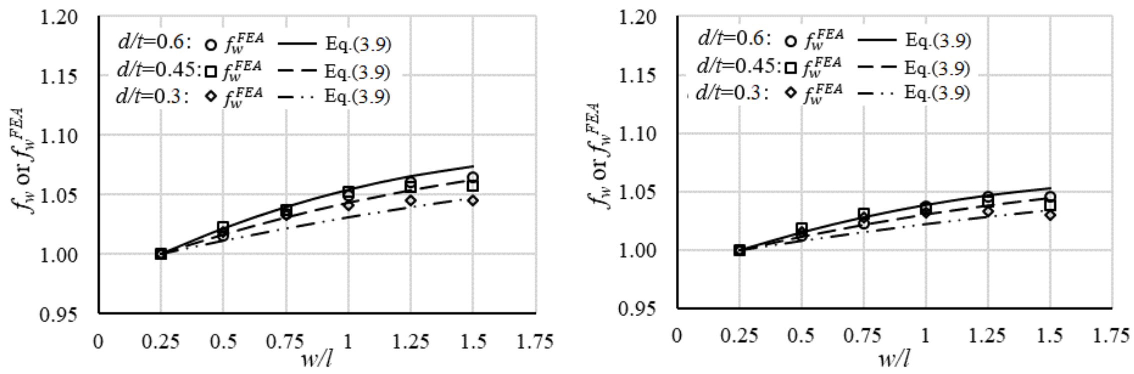

(c) $l^2/(Dt)=40$ (d) $l^2/(Dt)=60$

Figure 3.5 Predicted and FEA results of width effect on burst capacity for $l^2/(Dt)$=5, 20, 40 and $l^2/(Dt)$=60 with d/t=0.3, 0.45 and 0.6

By combining Eqs. (3.3) and (3.4), the proposed burst capacity model for a corroded pipeline can be expressed as:

$$P_b = f_w \left(\frac{1}{\sqrt{3}}\right)^{n+1} \frac{4t\sigma_u}{D} \frac{1-\frac{d}{t}}{1-\frac{d}{tM}} \tag{3.10}$$

where f_w and M are given by Eqs. (3.8) and (3.9), respectively.

Figure 3.6 shows that the burst capacities predicted by Eq. (3.10) are in good agreement with the corresponding burst capacities obtained from FEA for the 156 analysis cases used to develop Eqs. (3.8) and (3.9).

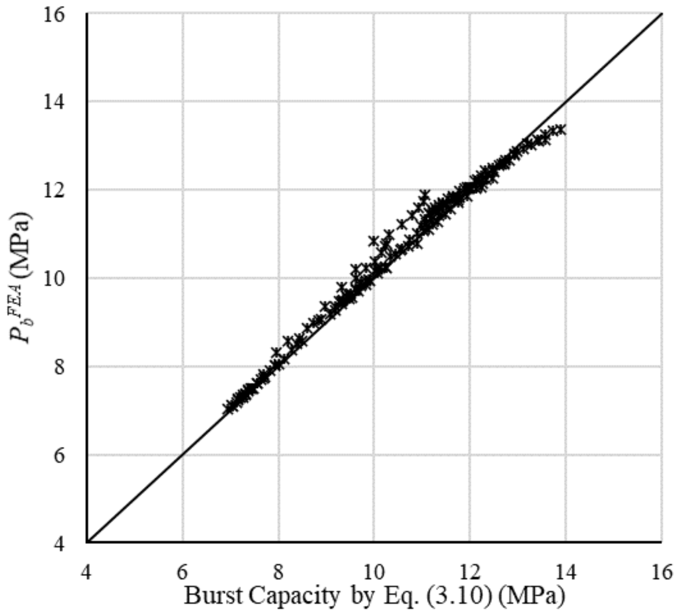

Figure 3.6 Comparison of burst capacities between fitting solution and FEA results

3.4 Validation of the proposed burst pressure model

To validate the proposed burst capacity model (Eq. (3.10)), an analysis matrix of 477 FEA cases is developed involving three different pipes. The corresponding pipe attributes, i.e. *D*, *t*, steel grade, *E*, σ_y and σ_u, which are representative of typical oil and gas transmission pipelines, are summarized in Table 3.2. The values of σ_y and σ_u of a given steel grade considered in FEA are assumed to equal the corresponding SMYS and SMTS (specified minimum tensile strength), respectively. The power-law stress-strain relationship for the pipe steel is adopted in the FEA (Zhang and Zhou, 2020), with the value of n estimated from Eq. (3.6). Each analysis case contains a semi-ellipsoidal corrosion defect with d/t equal to 0.3, 0.45, or 0.6, $l^2/(Dt)$ equal to 2, 5, 15, 20, 30, 40, 50 or 60, and w/l equal to 0.25, 0.5, 0.75, 1, 1.25, 1.5, 1.75 or 2. The maximum w/l value considered in FEA is 2 for $l^2/(Dt)$ = 2 and 5, 1.75 for $l^2/(Dt)$ = 15, and 1.5 for the other values of $l^2/(Dt)$. The pipe model is longitudinally fully-restrained subjected to internal pressure only. The FEA is performed by the commercial FEA package ABAQUS (Dassault Systèmes, 2016) by adopting the von Mises yield criterion and the associated flow rule as well as the isotropic hardening rule. The finite-strain configuration is employed to capture the geometrical and material non-linearity in the analysis. The internal pressure is gradually increased from zero until the burst criterion is reached. No dynamic effects are considered in the analysis. The burst capacity is determined as the pressure at which the nodal von Mises stress anywhere within the corrosion defect reaches the true stress corresponding to σ_u (Zhang and Zhou, 2020). It is noted that due to the highly refined mesh within the corrosion region in the finite element model, the difference between the nodal stress and Gaussian point stress for a given element is negligibly small. Furthermore, the nodal stress as opposed to the Gaussian point stress is almost always used in previous studies, e.g. (Cronin, 2000; Bao et al., 2018), to determine the burst capacity using FEA. The adequacy of this criterion has been demonstrated in previous studies (Cronin, 2000; Bao et al., 2018; Zhang and Zhou, 2020). Two representative finite element models are depicted in Fig. 3.7.

Table 3.2 Pipe attributes considered in parametric FEA

Pipe	Steel grade	D (mm)	t (mm)	E (GPa)	σ_y (MPa)	σ_u (MPa)
1	X52	406	6.0	200	359	455
2	X60	508	6.4	200	414	517
3	X70	914	10.6	200	483	565

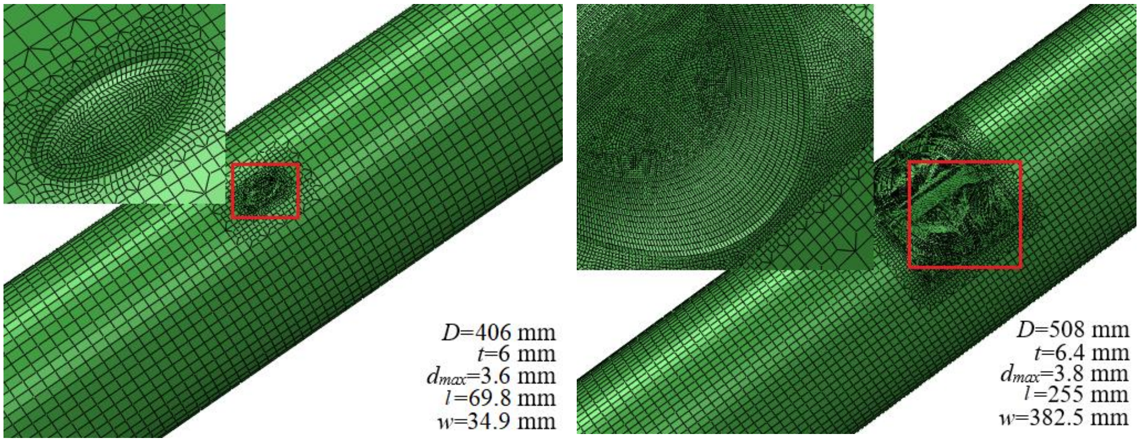

Figure 3.7 Representative finite element models used to validate the proposed burst capacity model

The proposed burst capacity model is used to predict the burst capacities of the 477 analysis cases. In addition, the seven burst capacity models summarized in Table 3.1 are also employed to predict the burst capacities of the analysis cases so that the accuracy of the proposed model can be compared with those of the existing models. Figure 3.8 compares the model- and FEA-predicted burst capacities for each of the models. This figure indicates that the proposed model results in the best predictions of all the models considered. The B31G predictions (Fig. 3.8(a)) are separated into distinctive groups, due mainly to the discontinuity in B31G at $l^2/(Dt) = 20$. For deep, long defects (i.e. with relatively low burst capacities), B31G is highly conservative. As depicted in Figs. 3.8(b) and 3.8(c), the B31G-M and CSA models tend to be more conservative for shallow, short defects (i.e. with relatively high burst capacities) and less conservative for deep, long defects (i.e. with relatively low burst capacities). The mean and coefficient of variation (COV) of the FEA-to-model predicted burst capacity ratios for the 477 analysis cases are summarized in Table 3.3, which again demonstrates that the proposed model leads to the most accurate burst capacity predictions compared with the other models: the mean and coefficient of variation (COV) of the FEA-to-predicted burst capacity ratios are 1.02 and 2.2%, respectively. The accuracies of B31G-M, CSA, DNV, RSTRENG and Sun et al.'s model are somewhat comparable. The B31G and SHELL92 models lead to on average the most conservative predictions (Figs. 3.8(a) and 3.8(f)), with the means of the FEA-to-model prediction ratios equal to 1.40 and 1.49, respectively. Compared with the other models, B31G leads to predictions with the highest variability: the COV of the FEA-to-model prediction ratios equal to 13.5%.

The fact that predictions by the B31G, B31G Modified, CSA, DNV, RSTRENG, SHELL92 and Sun et al.'s models are markedly conservative compared with the FEA predictions is due mostly to the three aspects: the flow stress, Folias factor and defect width effect. The empirical definitions of the flow stress adopted in these seven models except Sun et al.'s model do not adequately characterize the material strain hardening effect as depicted in Fig. 3.2 and lead to conservative predictions of the burst capacity. The Folias factor equations adopted in all of these models result in large values of M as depicted in Fig. 3.4 and therefore conservative predictions of the burst capacity. Finally, none of the seven burst capacity models takes into account the beneficial effect of the defect width, which again leads to conservative predictions of the burst capacity.

Table 3.3 Mean and COV of the FEA-to-model predicted burst capacity ratios

	B31G	B31G-M	CSA	DNV	RSTRENG	SHELL92	Sun et al.'s model	Proposed model
Mean	1.40	1.24	1.27	1.23	1.24	1.49	1.13	1.02
COV	13.5%	5.2%	5.6%	4.6%	4.1%	6.2%	5.0%	2.2%

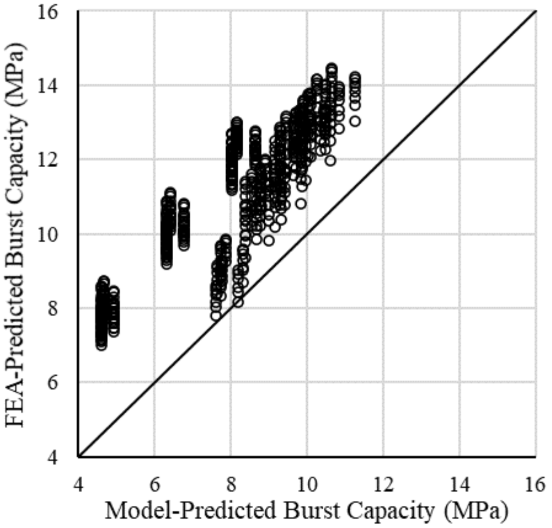

(a) B31G

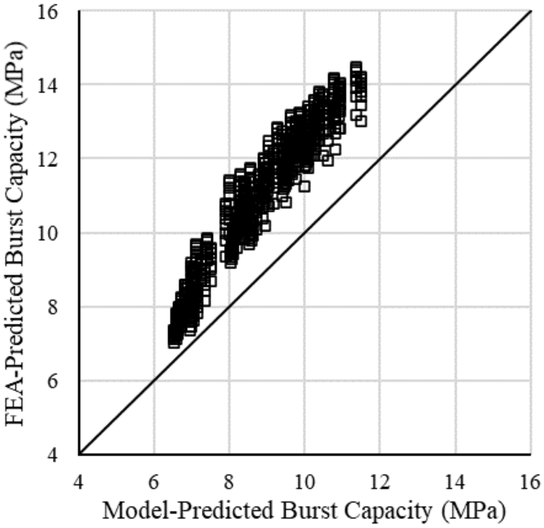

(b) B31G Modified

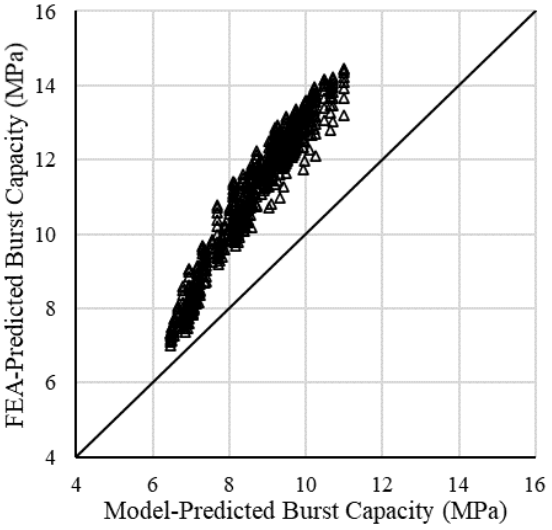

(c) CSA

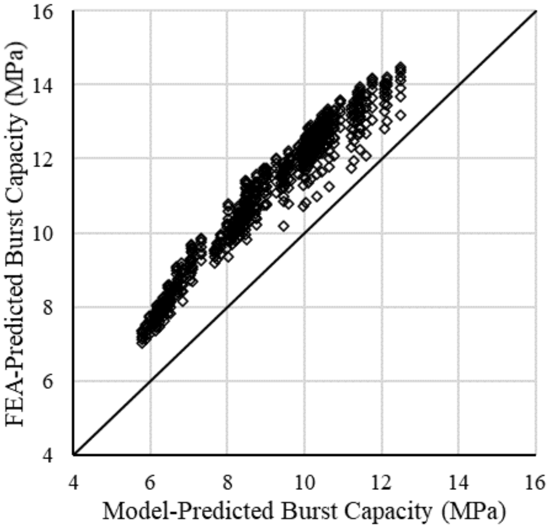

(d) DNV

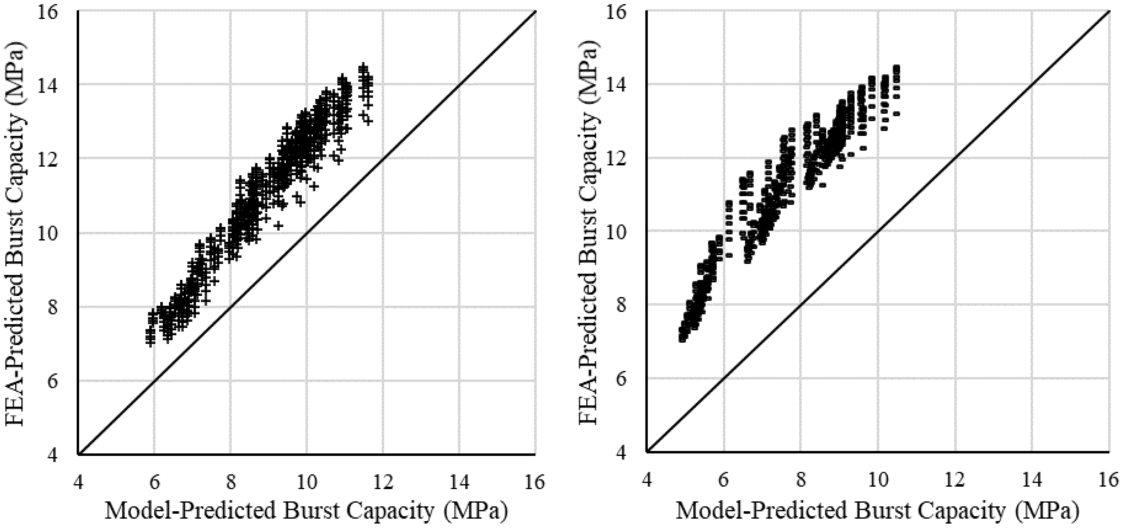

(e) RSTRENG (f) SHELL92

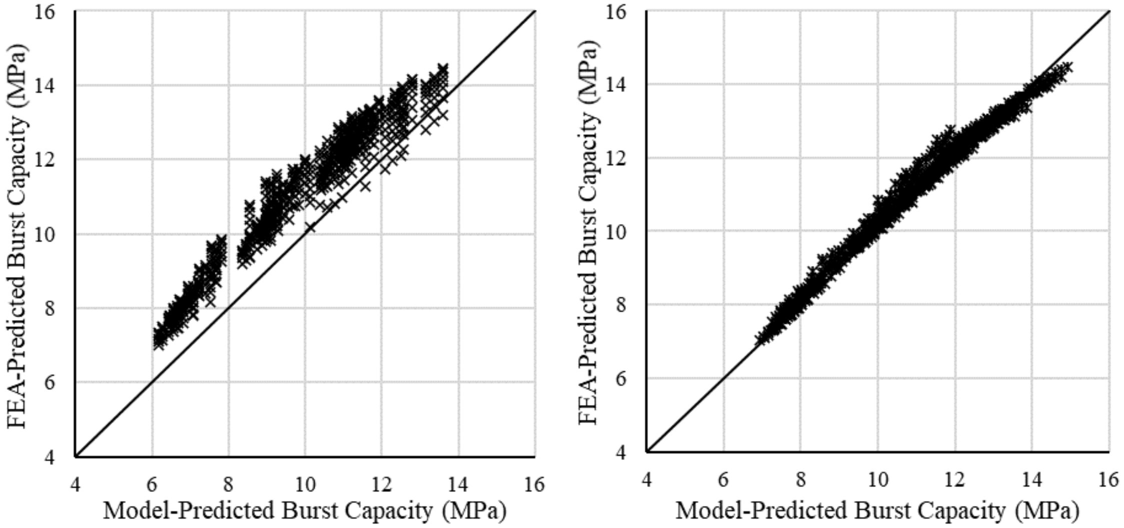

(g) Sun et al.’s model (h) Proposed model

Figure 3.8 Performance of the burst capacity models

The histogram of ratios of burst capacities predicted by FEA and the proposed model for the 477 cases is shown in Fig. 3.9. The figure indicates that about 3% of the model predictions are greater than the corresponding FEA predictions (i.e. non-conservative model predictions) by more than 2%, with the largest over-prediction by the model being about 4%. The FEA-to-model prediction ratios for almost 80% of the 477 cases are in the range of 0.99 – 1.04. These results demonstrate the reliability of the proposed model and its suitability for practical application.

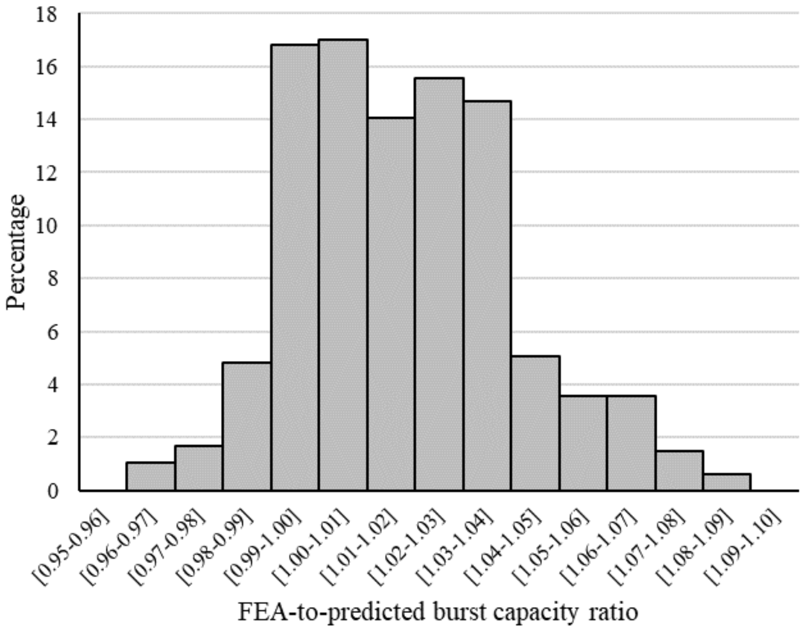

Figure 3.9 Histogram of ratios of burst capacities predicted by FEA and the proposed model for the 477 validation cases

The values of d/t and $l^2/(Dt)$ of the corrosion defects in the above-described 477 validation cases are within the limits of d/t and $l^2/(Dt)$ considered in the model development, i.e. $0.3 \leq d/t \leq 0.6$ and $2 \leq l^2/(Dt) \leq 60$. To validate the proposed model for corrosion defects outside of these limits, 12 additional FEA cases involving deep, long corrosion defects as summarized in Table 3.4 are considered. The attributes of pipe #1 shown in Table 3.2 are employed in the FEA. The burst capacities predicted by the proposed model are summarized in Table 3.4 along with the FEA results. The results indicate that the proposed model can accurately predict the burst capacity, the mean and COV of FEA-to-model prediction ratios equal to 1.02 and 0.8%, respectively, for the additional validation cases. Based on this, it is suggested that the proposed model be applicable for d/t up to 0.65 and $l^2/(Dt)$ up to 100. Such an applicability range is sufficient for the need of practical fitness-for-service assessment of corrosion defects (API RP 579, 2016; BS7910, 2019).

Table 3.4 Predictions by the proposed model and FEA for deep, long defects

d_{max}/t	$l^2/(Dt)$	w/l	P_b^{FEA} (MPa)	P_b (MPa)	P_b^{FEA}/P_b

0.5	80	0.25	9.13	8.89	1.03
		0.5	9.19	8.97	1.02
		0.75	9.30	9.04	1.03
	100	0.25	9.03	8.82	1.02
		0.5	9.05	8.88	1.02
		0.75	9.14	8.93	1.02
0.65	80	0.25	6.80	6.56	1.03
		0.5	6.79	6.64	1.02
		0.75	6.83	6.70	1.01
	100	0.25	6.63	6.55	1.01
		0.5	6.66	6.61	1.01
		0.75	6.70	6.65	1.01
		Mean			1.02
		COV			0.8%

3.5 Conclusion

In this chapter, a burst capacity model is proposed for corroded oil and gas pipelines based on extensive parametric 3D elasto-plastic FEA validated by full-scale burst tests. The proposed model idealizes a corrosion defect to be semi-ellipsoidal-shaped as it better approximates the geometry of real corrosion defects than the commonly used rectangular (or cubic) idealization. The model follows the basic form of the NG-18 equation, and incorporates the defect width effect, a new Folias factor equation that depends on both the defect depth and length, and the flow stress defined as a function of the strain hardening exponent and ultimate tensile strength of the pipe steel. The equations for the Folias factor and defect width effect in the proposed model are developed by nonlinear curve fitting of FEA results. The accuracy of the proposed burst capacity model is demonstrated based on extensive parametric FEA and shown to be higher than those of seven existing burst capacity models for corroded pipelines, including B31G, B31G-M, CSA, DNV, RSTRENG and SHELL92 as well as the model recently developed by Sun et al. The validation of the proposed model further indicates that it can be applied to corrosion defects with d/t ranging from 0.3 to 0.65 and $l^2/(Dt)$ ranging from 2 to 100. These ranges are sufficient for the proposed model to be applied in practical fitness-for-service assessment of corroded pipelines.

References

Al-Owaisi, S. S., Becker, A. A., & Sun, W., 2016. Analysis of shape and location effects of closely spaced metal loss defects in pressurised pipes. *Engineering Failure Analysis, 68,* 172-186.

Al-Owaisi, S., Becker, A. A., Sun, W., Al-Shabibi, A., Al-Maharbi, M., Pervez, T., & Al-Salmi, H., 2018. An experimental investigation of the effect of defect shape and orientation on the burst pressure of pressurised pipes. *Engineering Failure Analysis, 93,* 200-213.

API RP 579, 2016. Fitness for Service, *American Petroleum Institute,* Washington, D.C., US.

ASME, 1991. Manual for determining the remaining strength of corroded pipelines- a supplement to ASME B31 code for pressure piping, The American Society of Mechanical Engineers, New York.

Bao, J., Zhang, S., Zhou, W., & Zhang, S., 2018. Evaluation of Burst Pressure of Corroded Pipe Segments Using Three-Dimensional Finite Element Analyses. In *2018 12th International Pipeline Conference* (pp. V001T03A043-V001T03A043). American Society of Mechanical Engineers.

Benjamin, A. C., de Andrade, E. Q., Jacob, B. P., Pereira, L. C., & Machado, P. R., 2006. Failure behavior of colonies of corrosion defects composed of symmetrically arranged defects. In *2006 International Pipeline Conference* (pp. 417-432). American Society of Mechanical Engineers.

BS7910, B. S., 2019. Guide on methods for assessing the acceptability of flaws in metallic structures. *British Standards Institution,* 389 Chiswick High Road, London, UK.

Chen, Y., Zhang, H., Zhang, J., Li, X., & Zhou, J., 2015. Failure analysis of high strength pipeline with single and multiple corrosions. *Materials & Design*, *67*, 552-557.

Cronin, D. S., 2000. Assessment of corrosion defects in pipelines, PhD thesis, University of Waterloo.

Cronin, D. S., & Pick, R. J., 2000. Experimental database for corroded pipe: evaluation of RSTRENG and B31G. In *2000 3rd International Pipeline Conference*. American Society of Mechanical Engineers Digital Collection.

Canadian Standard Association, (CSA), 2019. Oil and gas pipeline systems. CSA standard Z662-19. *Mississauga, Ontario, Canada*.

Dassault Systèmes, D. S., 2016. Abaqus analysis user's guide. Technical Report Abaqus 2016 Documentation, Simulia Corp.

Det Norske Veritas (DNV), 2017. Recommended practice DNV-RP-F101, corroded pipelines, Hovic, Norway.

Folias, E. S., 1964. The stresses in a cylindrical shell containing an axial crack. APL 64-174, Aerospace Research Laboratories.

Folias, E. S., 1965. An axial crack in a pressurized cylindrical shell. *International Journal of Fracture Mechanics*, *1*(2), 104-113.

Hahn, G. T., Sarrate, M., & Rosenfield, A. R., 1969. Criteria for crack extension in cylindrical pressure vessels. *International Journal of Fracture Mechanics*, *5*(3), 187-210.

Keshtegar, B., & Seghier, M. E. A. B., 2018. Modified response surface method basis harmony search to predict the burst pressure of corroded pipelines. *Engineering Failure Analysis*, *89*, 177-199.

Kiefner, J. F., 1969. Fracture initiation. In *Paper G, Proceedings of the 4th Symposium on Line Pipe Research, Pipeline Research Committee of the American Gas Association, Dallas, Texas, USA, AGA Catalogue* (No. L30075, pp. G1-G36).

Kiefner, J. and Vieth, P., 1989. A modified criterion for evaluating the remaining strength of corroded pipe (No. PR-3-805). Battelle Memorial Institute, OH (USA).

Kiefner, J. and Vieth, P., 1990. PC program speeds new criterion for evaluating corroded pipe, Oil and Gas Journal, August 20, 1990. pp. 91-93.

Leis, B. N., Zhu, X. K., McGaughy, T. (2016). Assessment of Corrosion Model Error for Metal-Loss defects in Pipelines. *Pipeline Research Council International, PR-185-143600-R01*. Project Number: 54922CSP

MATLAB. 2018. Natick, Massachusetts: The MathWorks Inc.

Netto, T. A., 2010. A simple procedure for the prediction of the collapse pressure of pipelines with narrow and long corrosion defects – correlation with new experimental data. *Applied Ocean Research, 32*(1), 132-134.

Ritchie, D., & Last, S., 1995. Burst criteria of corroded pipelines-defect acceptance criteria. In *Proceedings of the EPRG/PRC 10th biennial joint technical meeting on line pipe research*. Cambridge, UK, Paper 32.

Shuai, Y., Shuai, J., & Xu, K., 2017. Probabilistic analysis of corroded pipelines based on a new failure pressure model. *Engineering Failure Analysis*, 81, 216-233.

Su, C. L., Li, X., & Zhou, J., 2016. Failure pressure analysis of corroded moderate-to-high strength pipelines. *China Ocean Engineering*, *30*(1), 69-82

Sun, M., Li, X., & Liu, J., 2020. Determination of Folias Factor for Failure Pressure of Corroded Pipeline. *Journal of Pressure Vessel Technology*, *142*(3).

Zhang, S., & Zhou, W., 2020. Assessment of effects of idealized defect shape and width on the burst capacity of corroded pipelines. *Thin-Walled Structures*, *154*, 106806.

Zhu, X., and Leis, B. N., 2007, Theoretical and Numerical Predictions of Burst Pressure of Pipelines, ASME J. Pressure Vessel Technol., 129(4), pp. 644–652.

Zhu, X. K., & Leis, B. N., 2005. Influence of yield-to-tensile strength ratio on failure assessment of corroded pipelines. *Journal of Pressure Vessel Technology*, 127, pp. 436-442.

4 Development of a Burst Capacity Model for Corroded Pipelines under Internal Pressure and Axial Compression Using Artificial Neural Network

4.1 Introduction

Corrosion defects threaten the structural integrity of oil and gas pipelines as they cause thinning of the pipe wall and therefore reduce the pressure containment capacity, i.e. burst capacity, of the pipeline. In-service pipelines are often subjected to longitudinal forces and bending moments resulting from, for example, ground movement or formation of free spans (Karimian, 2006; Wijewickreme et al., 2009; Meidani et al., 2017; Meidani et al., 2018), in addition to internal pressures. In practice, there are some site-specific cases where corrosion anomalies are present on the pipeline in locations which correspond to external loads. A refined assessment model is required to understand the load carrying capacity of pipe where these interacting conditions exist. As reported in (Chouchaoui, 1995; Bjørnøy et al., 2000; Smith and Waldhart, 2000; Liu et al, 2009; Taylor et al., 2015; Mondal and Dhar, 2019), the burst capacity of a corroded pipeline under the longitudinal compression and internal pressure can be markedly lower than that of the pipeline under the internal pressure only. Note that the longitudinal compression may result from a compressive force or bending moment (with the corrosion defect located on the compression side of the bending). While several methods for the assessment of corroded pipelines are available, such as the B31G (ASME, 1991), B31G Modified (Kiefner and Vieth, 1989), CSA (2019), RSTRENG (Kiefner and Vieth, 1990) and PCORRC (Stephens and Leis, 2000) methods, these methods consider only internal pressure loading. Methods for the assessment of corroded pipelines under combined loading have also been reported in the literature, e.g. the two well-known methods given in DNV RP-F101 (DNV, 2017) and RPA-PLLC (Benjamin, 2008) (RPA stands for rectangular parabolic area, and PLLC stands for pressure loading plus longitudinal compression), respectively. There are however drawbacks in the DNV RP-F101 and RPA-PLLC methods. Both methods include a relatively high threshold compressive stress (typically greater than 30% of the pipe yield strength), below which the compressive stress is considered to have no effect on the burst capacity. This however is inconsistent with observations obtained in the present study (Liu et al., 2009; Mondal and Dhar, 2019). Results of finite element analyses (FEA) indicate that a compressive stress of about 15% of the pipe yield strength can have a significant impact on the burst capacity of corroded pipelines, as discussed in detail in Section 4.3. Therefore, a more accurate method for assessing the burst capacity of corroded pipelines under combined loading is needed.

The three-dimensional (3D) elasto-plastic FEA has proven to be an effective tool to evaluate the burst capacity of corroded pipelines (Chouchaoui, 1995). Although naturally-occurring corrosion defects are irregularly shaped, corrosion defects considered in FEA are often in idealized shapes, such as the semi-ellipsoidal shape illustrated in Fig. 4.1 with given depth (*d*), length (*l*) and width (*w*).

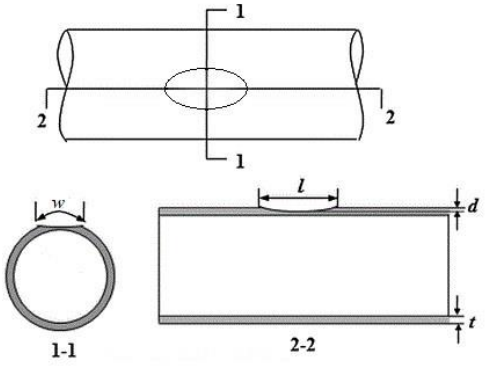

Figure 4.1 Schematic for corrosion defect idealized as semi-ellipsoidal shape

In this chapter, extensive parametric FEA are carried out to evaluate the burst capacity of corroded pipelines under combined internal pressure and axial compression by varying the pipe geometric and material properties, defect depth, length and width, and magnitude of axial compressive stress. The parametric FEA employs the ultimate tensile strength (UTS)-based burst criterion and idealizes corrosion defects as semi-ellipsoidal shaped flaws. Based on the parameter FEA results, an artificial neural network (ANN) model is developed in the open-source platform PYTHON, to predict the burst capacity of pipelines containing single corrosion defects under combined internal pressure and axial compression. The rest of this chapter is organized as follows. Section 4.2 presents details of the finite element model and validation of the model; the effect of longitudinal compression on the burst capacity of corroded pipelines is investigated in Section 4.3; Section 4.4 presents the development of the PYTHON-based ANN model as well as the validation, followed by conclusions in Section 4.5.

4.2 FEA model

4.2.1 General

The FEA analysis is performed by the commercial FEA package ABAQUS (Dassault Systèmes, 2016) in this study. The 8-node solid element (C3D8) with full integration is used in the numerical simulation. The finite-strain elasto-plastic analysis is employed to capture the geometrical and material non-linearity. The von Mises yield criterion and the associated flow rule as well as the isotropic hardening rule are adopted in the numerical simulation.

4.2.2 Material Properties and Failure Criterion

The stress–strain relationship of typical pipe steels can be well represented by a power-law model as given in Eq. (4.1) (Zhu and Leis, 2004; Wang and Zhang, 2011), which is adopted in the present study.

$$\begin{cases} \sigma = E\varepsilon & \sigma < \sigma_y \\ \sigma = K\varepsilon^n & \sigma \geq \sigma_y \end{cases} \tag{4.1}$$

where σ and ε denote the true stress and true strain in the uniaxial tensile test, respectively; E is Young's modulus; σ_y is the yield strength, defined as the stress corresponding to an offset (i.e. plastic) strain of 0.2% or a total strain of 0.5%; K and n are coefficients of the power-law stress-strain relationship in the plastic domain, and n is also known as the strain hardening exponent.

If tensile coupon test results are available, the values of K and n in Eq. (4.1) can be obtained from curve fitting of the test data. Since the stress-strain curve obtained from the tensile coupon test is usually reported in terms of the engineering stress (σ') and engineering strain (ε'), they are converted to the corresponding true stress and true strain, respectively. In the elastic domain, $\sigma(\varepsilon)$ is assumed equal to $\sigma'(\varepsilon')$. In the plastic domain, $\sigma(\varepsilon)$ is converted from $\sigma'(\varepsilon')$ as follows up to the onset of necking:

$$\varepsilon = \ln(1 + \varepsilon') \tag{4.2a}$$

$$\sigma = \sigma'(1 + \varepsilon') \tag{4.2b}$$

If only the yield strength (σ_y) and ultimate tensile strength (UTS), denoted by σ_u, are known while coupon test results are unavailable, the following empirical equation can be used to estimate the value of *n* (Zhu and Leis, 2005):

$$n = 0.239\left(\frac{1}{\sigma_y/\sigma_u} - 1\right)^{0.596} \tag{4.3}$$

Given the value of *n*, *K* can be estimated by using the Considere's criterion (Dowling, 2007):

$$K = \frac{e^n}{n^n}\sigma_u \tag{4.4}$$

where *e* is the base of the natural logarithm.

The UTS-based failure criterion, which has been used in the literature to predict the burst capacity of corroded pipelines (Cronin, 2000; Bao et al., 2018), is adopted in this study. According to this criterion, the burst capacity of a corroded pipe is reached once the maximum von Mises (true) stress at any point within the defected region reaches the true stress corresponding to UTS.

4.2.3 Validation of FEA

Full-scale burst tests reported in the literature involving pipe specimens containing semi-ellipsoid-shaped defects (Al-Owaisi, 2018) are used to validate the finite element model and UTS-based failure criterion. The material properties of the test specimens are summarized in Table 4.1. The outside diameters (*D*) and wall thicknesses (*t*) of the test specimens are summarized in Table 4.2. Four layers of elements are used through the thickness of each defect area to capture the high stress gradient along the radial direction of the defect area. To improve the computational efficiency, the mesh in the FEA model is transitioned from a high density in the defect region to a low density in the defect-free region in the longitudinal, circumferential and radius directions. Because of symmetry, a half of a given specimen is modelled. The mesh density is selected after a convergence study. Figure 4.2 depicts the FEA mesh for a representative pipe specimen, #18, containing a semi-ellipsoid-shaped defect. The mesh in Fig. 4.2 consists of 15645 nodes with the corresponding number of elements equal 9450.

Table 4.1 Material properties of test specimens reported in (Al-Owaisi, 2018)

Steel grade	E (GPa)	σ_y (MPa)	σ_u (MPa)	n
X52	182	372	497.7	0.20

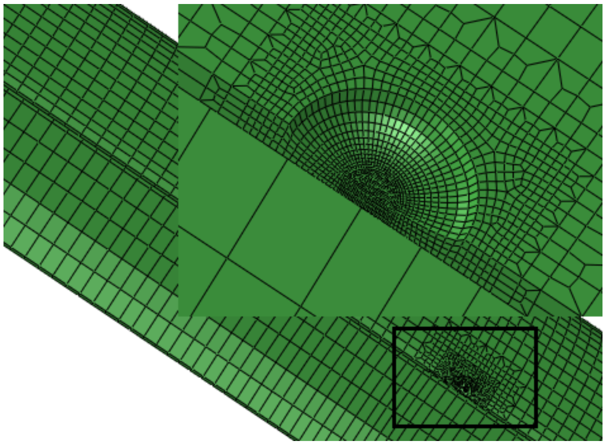

Figure 4.2 FEA mesh for the semi-ellipsoidal-shaped defect in specimen 18 reported in (Al-Owaisi, 2018)

The symmetric constraint is applied to the symmetry plane, and one end of the model is restricted in the longitudinal direction. As the pipe specimens are end-capped during the burst tests, corresponding axial stress is simultaneously applied at the free end of the model while the internal pressure is applied. The FEA-predicted burst capacities (P_{FEA}) for are summarized in Table 4.2, together with the actual burst capacities from tests (P_{test}).

Table 4.2 Comparison of FEA burst prediction and test results

Specimen ID	D (mm)	t (mm)	P_{test} (MPa)	P_{FEA} (MPa)	P_{test}/P_{FEA}
18	508	9.7	19.55	19.83	0.99
19		9.85	19.11	19.15	1.00

20		9.7	19.59	19.39	1.01
21		9.7	19.65	19.48	1.01
22		9.75	20.08	19.65	1.02
23		9.8	20.27	19.80	1.02
30		9.7	20.68	20.06	1.03
		Mean			1.01
		COV			1.4%

The fact that the mean and coefficient of variation (COV) of P_{test}/P_{FEA} are 1.01 and 1.4%, respectively, as presented in Table 4.2 indicates that the FEA-predicted and test burst capacities are in excellent agreement. This provides a strong validation of the finite element model and UTS-based burst criterion employed in the analysis.

4.3 Effect of axial compression on burst capacity of corroded pipelines

Extensive parametric 3D FEA based on the semi-ellipsoidal idealization of the corrosion defect is carried out to investigate the influence of longitudinal compression on the burst capacity.

4.3.1 Analysis Cases

Four different pipe cases were considered in the FEA. The pipe attributes (D, t, Grade, MOP, E, yield strength and tensile strength) for these cases, which are representative of typical oil and gas transmission pipelines, are summarized in Table 4.3, where MOP denotes the maximum operating pressure. For a given analysis case shown in Table 4.3, three loading scenarios are considered: the base case in which the internal pressure is the only load, and two other scenarios involving combined loads with different magnitudes of the longitudinal compression. For the two scenarios involving combined loads, the longitudinal compression is introduced by applying a uniform compressive stress (σ_a) on the corrosion-free pipe cross section at the free end of the pipe model, while keeping the other end longitudinally restrained. The magnitude of the externally-applied longitudinal compression is expressed as the ratio of the corresponding compressive stress to σ_y, i.e. $\sigma_a/\sigma_y = -0.15$ and $\sigma_a/\sigma_y = -0.3$ for the two scenarios respectively (the negative sign indicates compression). The pipe in each analysis has a fixed length (L_{model}), with the defect located on the external surface at the centre of the pipe length, to avoid the effects of the end condition and slenderness as summarized in Table 4.3. Each analysis case contains a single semi-ellipsoidal corrosion defect for which various combinations of the depth, width and length are considered to understand how the severity of corrosion combined with external loading impacts the burst capacity. The corrosion defect parameters considered include defect depth (d/t) equal to 0.3, 0.45 or 0.6, normalized defect length $l^2/(Dt)$ equal to 2, 5, 15, 20, 30, 40, 50 or 60, and width-to-length ratio (w/l) equal to 0.25, 0.5, 0.75, 1, 1.25, 1.5, 1.75 or 2. The maximum w/l value considered in FEA is 2 for $l^2/(Dt)$ = 2 and 5, 1.75 for $l^2/(Dt)$ = 15, and 1.5 for the other values of $l^2/(Dt)$. Note that $l^2/(Dt)$ is commonly employed in semi-empirical burst capacity models, e.g. the B31G (ASME, 1991), B31G Modified (Kiefner and Vieth, 1989) and DNV (2017) models, as a dimensionless measure of the defect length and also adopted in the present study. Note further that $l^2/(Dt)$ = 20 is used to distinguish between short and long defects in the B31G model. Considering the permutations of above-described parameters, a total of 1905 FEA models were created and are used in the following analyses as well as the training and validation of the ANN model described in Section 4.4.

The power-law stress-strain relationship expressed by Eq. (4.1) is employed in the FEA. The values of n and K in Eq. (4.1) are determined using Eqs. (4.3) and (4.4), respectively.

Table 4.3 Attributes of the analysis cases considered in parametric FEA

Pipe group	Steel grade	D (mm)	t (mm)	L_{model} (mm)	E (GPa)	σ_y (MPa)	σ_u (MPa)	MOP (MPa)
1	X52	406	6.0	3000	200	359	455	5.3
2	X60	508	6.4	3400	200	414	517	6.5
3	X65	610	7.1	4000	200	448	531	6
4	X70	914	10.6	6000	200	483	565	6

To obtain the burst capacity of a corroded pipeline under combined loads, a three-step loading sequence is employed in FEA as follows.

1. Increase the internal pressure from zero to MOP under the longitudinally fully-restrained boundary condition.

2. Deactivate the longitudinal restraint of one end of the pipe model and increase the

longitudinal compressive stress to its target value (i.e. σ_a/σ_y = -0.15 or -0.30) while holding the internal pressure constant at MOP.

3. Increase the internal pressure from MOP until burst while holding σ_a constant at the level achieved at the end of step 2 and keeping the boundary conditions unchanged.

4.3.2 Analysis Results

A large amount of data is generated from the analysis; for brevity, only part of the results are depicted in figures presented below. Figure 4.3 depicts the FEA-predicted burst capacities (P_b) after applying longitudinal compression for Pipe 1 with varying defect depth of d/t=0.3, 0.45, 0.6 and lengths of $l^2/(Dt)$=2 and 20 compared with the burst capacities under the internal pressure only.

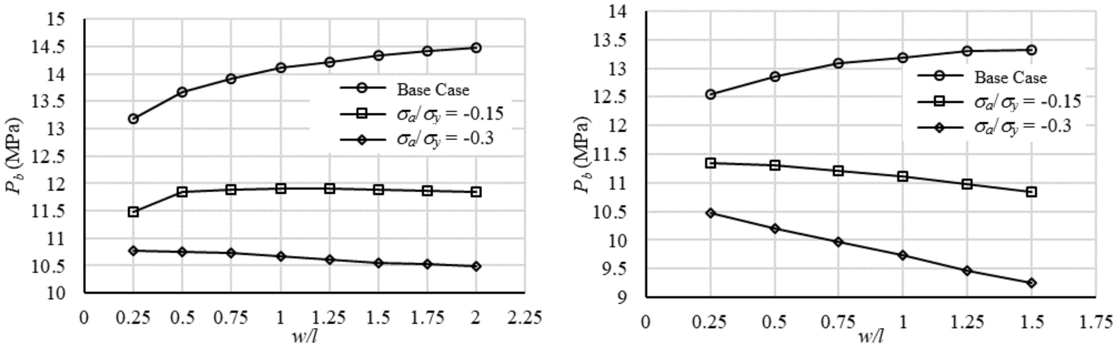

(a) d/t=0.3, $l^2/(Dt)$=2 (b) d/t=0.3, $l^2/(Dt)$=20

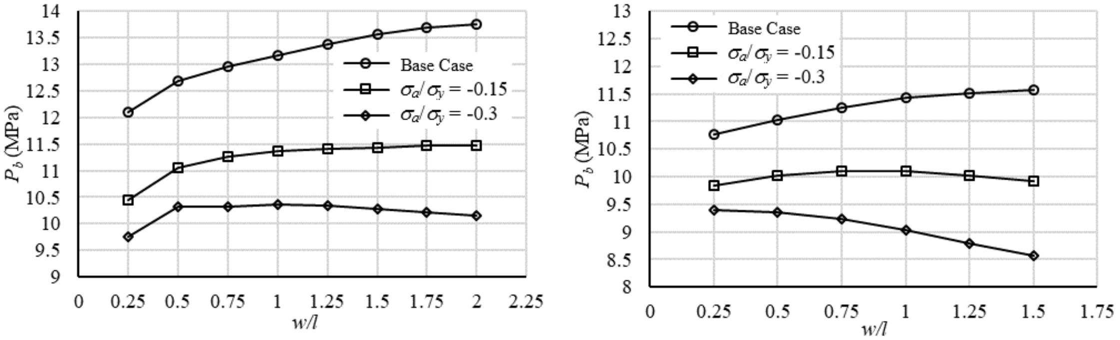

(c) d/t=0.45, $l^2/(Dt)$=2 (d) d/t=0.45, $l^2/(Dt)$=20

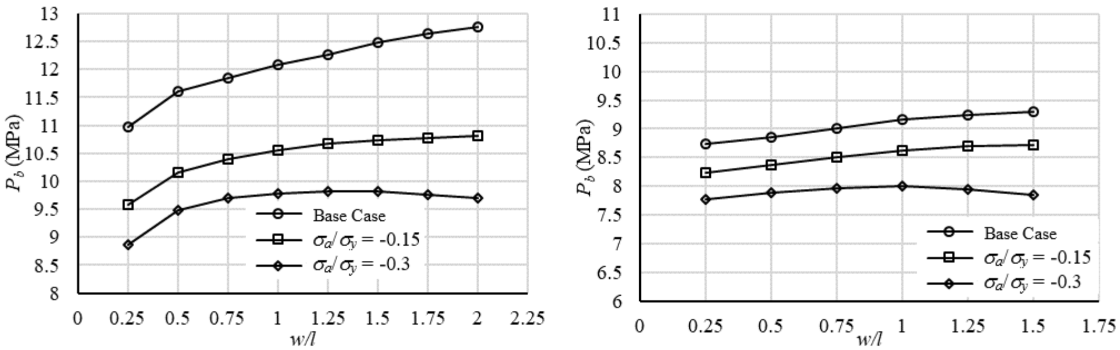

(e) d/t=0.6, $l^2/(Dt)$=2

(f) d/t=0.6, $l^2/(Dt)$=20

Figure 4.3 The influence of longitudinal compression on burst capacity (Pipe 1)

As shown in Figure 4.3, the burst capacity decreases with the application of the longitudinal compression. The maximum reduction in the burst capacity from that of the base case can be as much as 19% and 30% corresponding to the longitudinal compression level of σ_a/σ_y = -0.15 and σ_a/σ_y = -0.3, respectively. The reduction in the burst capacity due to the longitudinal compression is observed in all the analysis cases considered. It is worth mention that the cases under internal pressure loading only (base case), as depicted in Fig. 4.3, indicate that the burst capacity in general increases as the defect width increases with the defect depth and length remaining the same. This can be explained by the contributions of the membrane and bending components to the hoop stress in the defect region (Zhang and Zhou, 2020).

In order to illustrate the inter-dependent influence of the defect depth on the longitudinal compression effect on the burst capacity, cases with the same defect length and width are depicted together in Figure 4.4. To facilitate the comparison, the burst capacity corresponding to axial compression (P_{Comp}) is normalized by the burst capacity (P_{Base}) of the corresponding base case.

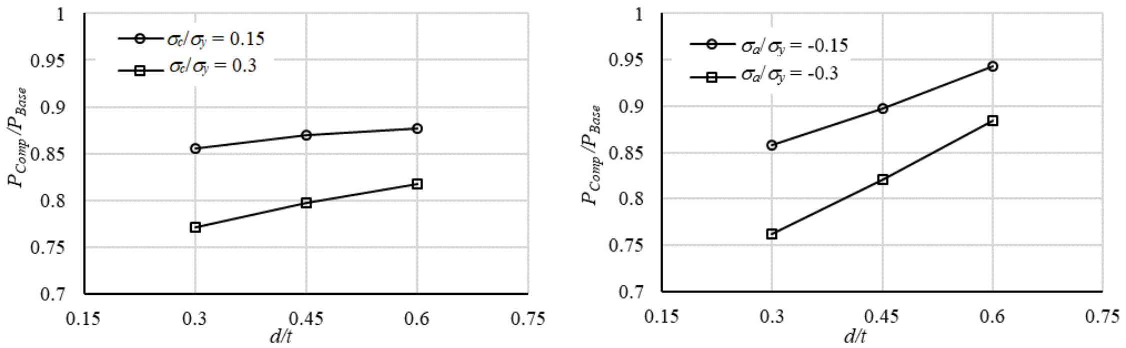

(a) $l^2/(Dt)=2$, $w/l=0.75$

(b) $l^2/(Dt)=20$, $w/l=0.75$

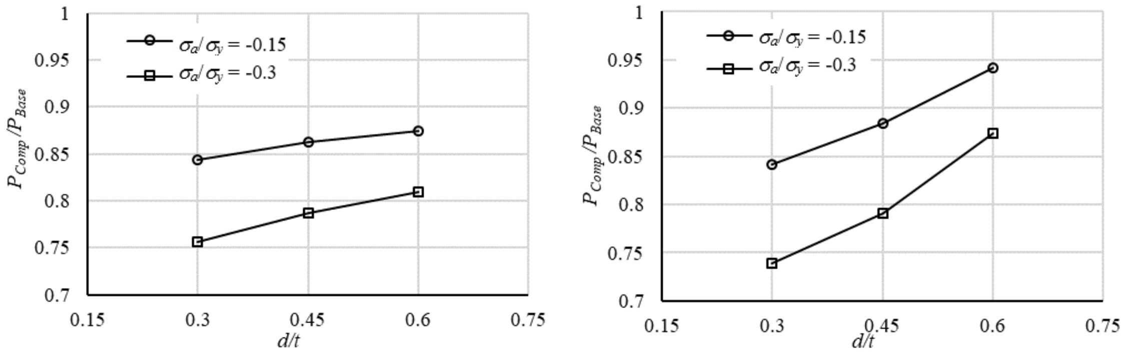

(c) $l^2/(Dt)=2$, $w/l=1$

(d) $l^2/(Dt)=20$, $w/l=1$

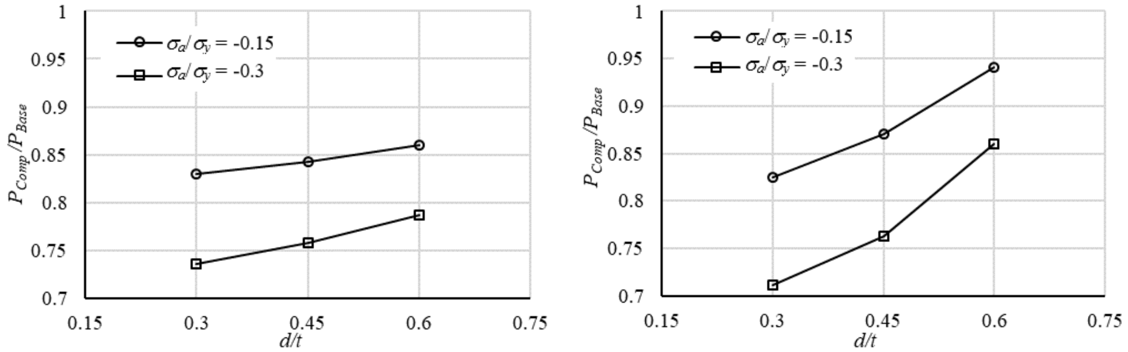

(e) $l^2/(Dt)=2$, $w/l=1.25$

(f) $l^2/(Dt)=20$, $w/l=1.25$

Figure 4.4 The longitudinal compression effect as a function of the defect depth (Pipe 1)

As shown in Fig. 4.4, the longitudinal compression effect on the burst capacity is dependent on the defect depth. All else being the same, the longitudinal compression effect is weakened with the increase of the defect depth. As shown in Fig. 4.4(f), $P_{Comp}/P_{Base} = 0.71$ for d/t=0.3, $l^2/(Dt)$=20 and w/l=1.25, whereas $P_{Comp}/P_{Base} = 0.86$ for $d/t = 0.6$, $l^2/(Dt)$=20 and w/l=1.25. This implies that for two corrosion anomalies with the same length and width, the impact of longitudinal compression on the burst pressure reduction is higher (i.e. lower P_{Comp}/P_{Base} ratio) for the shallow corrosion and lower (i.e. higher P_{Comp}/P_{Base} ratio) for the deep corrosion. This is because the uncorroded region for the cases with deep defects is generally elastic at burst, and the longitudinal compressive load is mainly resisted by the uncorroded region and does not greatly influence the corroded region. For analysis cases with shallow defects, however, due to the relatively high burst capacity, both the uncorroded and corroded regions are in the plastic domain at burst, meaning that the axial load is distributed more uniformly between the uncorroded and corroded regions. As a result, the longitudinal compression effect on the burst capacity is stronger for shallow defects. Furthermore, the longitudinal compression effect becomes stronger as the compressive stress increases. As depicted in Fig. 4.4(a), P_{Comp}/P_{Base} = 0.86 and 0.88, corresponding to d/t=0.3 and 0.6 ($l^2/(Dt)$=2 and w/l=0.75), respectively, under the axial compressive stress of σ_a/σ_y = -0.15, whereas P_{Comp}/P_{Base} = 0.77 and 0.82, corresponding to d/t=0.3 and0.6 ($l^2/(Dt)$=2 and w/l=0.75), respectively, under the axial compressive stress of σ_a/σ_y = -0.3.

Figure 4.5 indicates that the longitudinal compression effect is weakened with the increase of the defect length for relatively deep defects. For cases with shallow defects (i.e. d/t = 0.3), the longitudinal compression effect appears to be largely independent of the defect length.

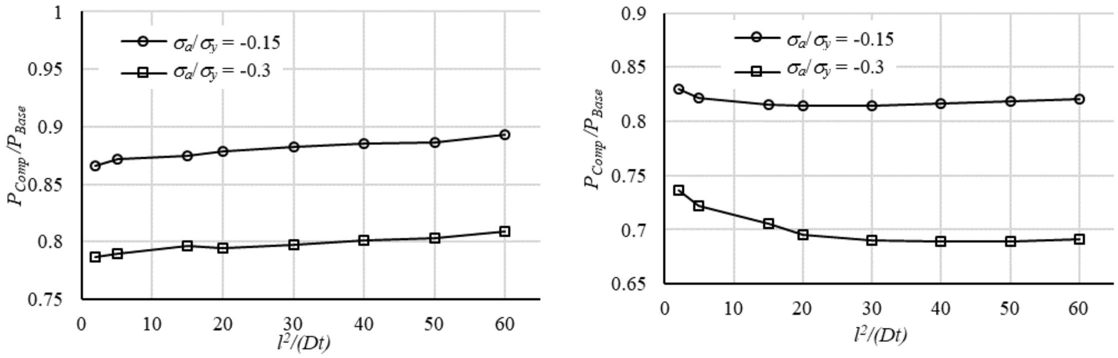

(a) d/t=0.3, w/l=0.5 (b) d/t=0.3, w/l=1.5

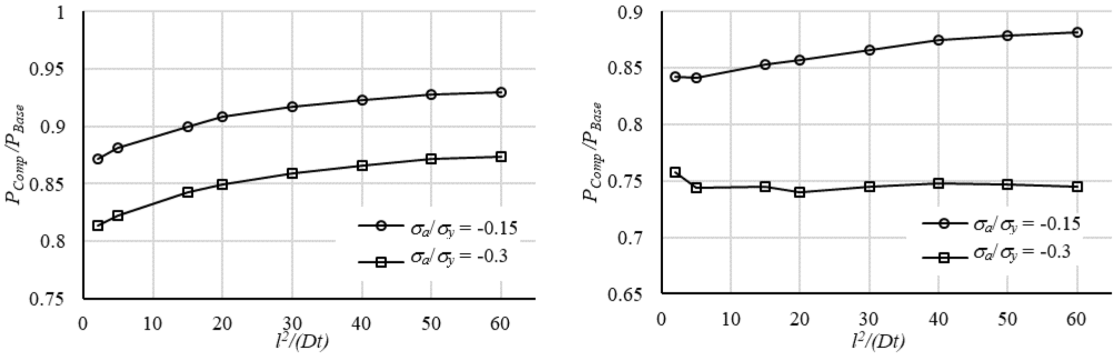

(c) d/t=0.45, w/l=0.5 (d) d/t=0.45, w/l=1.5

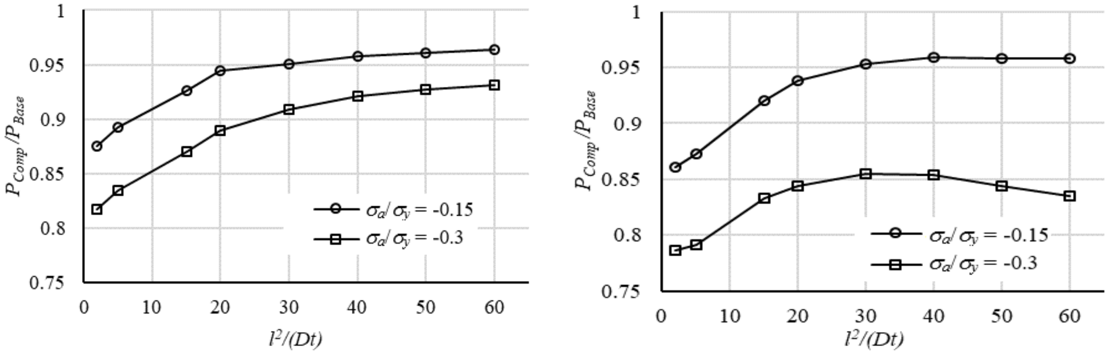

(e) d/t=0.6, w/l=0.5 (f) d/t=0.6, w/l=1.5

Figure 4.5 The longitudinal compression effect as a function of the defect length (Pipe 1)

Figure 4.6 indicates that the longitudinal compression effect is strongly dependent on the defect width-to-length ratio. All else being the same, the longitudinal compression effect is stronger as the width-to-length ration increases. This becomes more evident for shallow and/or short defects, and for cases with a high level of longitudinal compression.

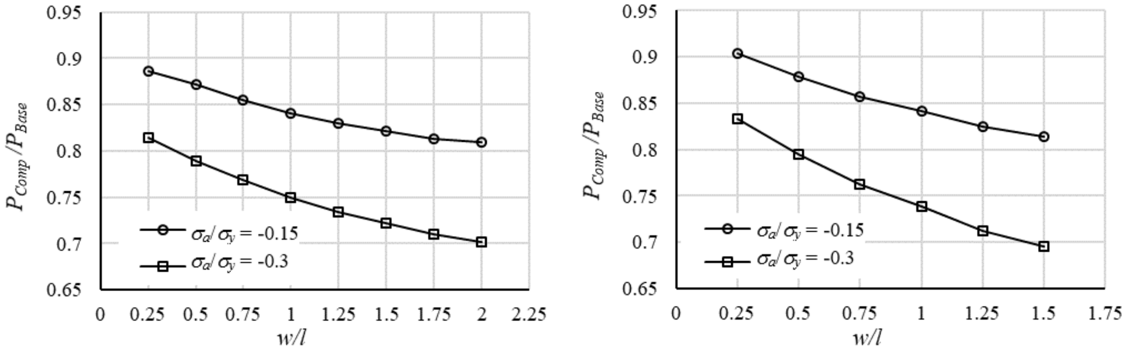

(a) d/t=0.3, $l^2/(Dt)$=2 (b) d/t=0.3, $l^2/(Dt)$=20

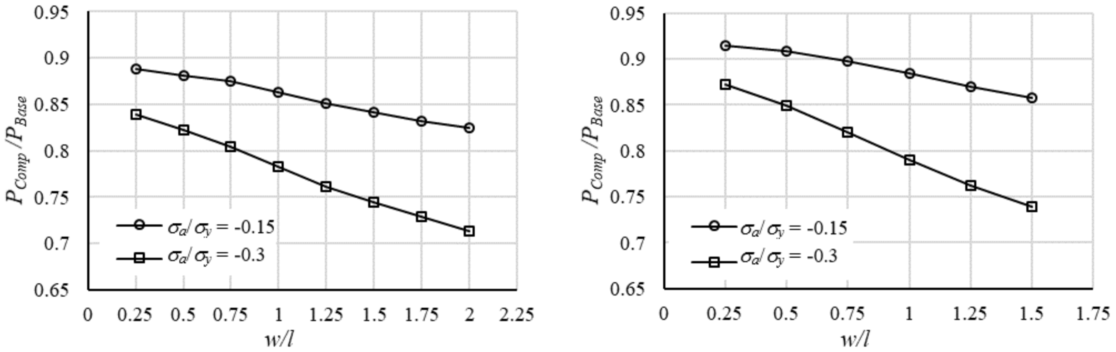

(c) d/t=0.45, $l^2/(Dt)$=2 (d) d/t=0.45, $l^2/(Dt)$=20

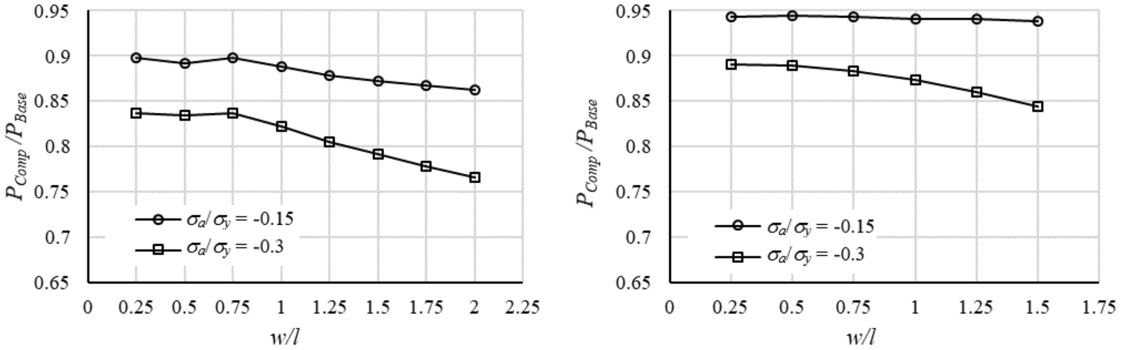

(e) d/t=0.6, $l^2/(Dt)$=2 (f) d/t=0.6, $l^2/(Dt)$=20

Figure 4.6 The longitudinal compression effect as a function of the defect width-to-length ratio (Pipe Group 1)

4.4 Development of ANN model

4.4.1 Setup of ANN Model

Based on the results of extensive parametric FEA, the Artificial Neural Network (ANN) is employed in the present study to develop a burst capacity model for corroded pipelines under combined internal pressure and longitudinal compression. ANN is a biologically inspired mathematical algorithm designed to simulate the structure and abilities of human brain in information processing (Zurada, 1992). ANN can gain knowledge by detecting the patterns and relationships between the input and output parameters and be trained from the training cases instead of traditional programming (Haykin,2009). Given the pipe attributes, as well as the corrosion defect and loading information, a well-trained ANN model can accurately and efficiently predict the burst capacity.

The present ANN model is built and trained on the open-source platform PYTHON. A three-layer feedforward network with backpropagation learning containing 6, 8 and 1 neurons in input, hidden, and output layers, respectively, is structured as shown in Fig. 4.7, considering most functions can be approximated using a single hidden layer (Ripley, 1996). The numbers of the input and output units are dependent on the particular problem. Normally, the number of the hidden units (G) is defined by the following empirical equation:

$$G = \sqrt{g_1 + g_2} + a \tag{4.5}$$

where g_1 and g_2 are the number of input and output units, respectively, and a is in the range of 0~10. The considered parameters for the burst capacity prediction of corroded pipelines under combined internal pressure and axial loading are shown in Fig. 4.7.

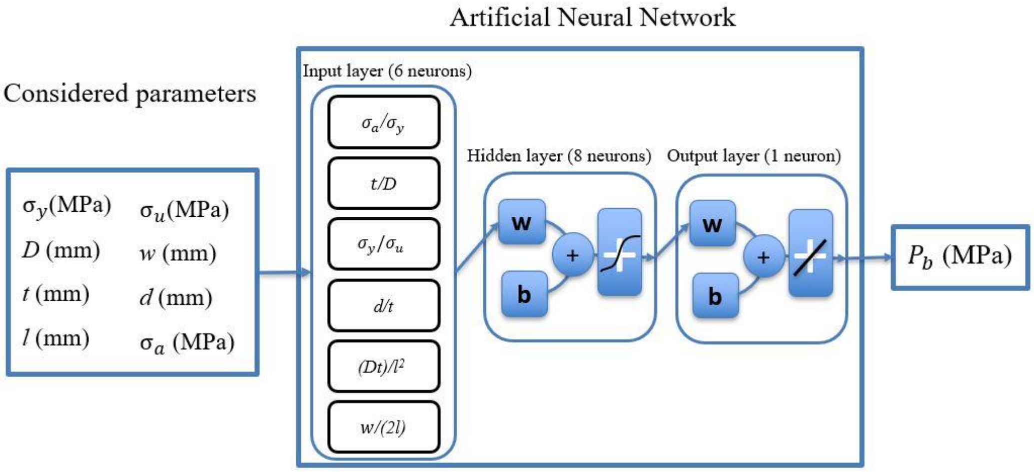

Figure 4.7 Three-layered ANN model for burst capacity under combined loading

4.4.2 Training of ANN Model

The ANN model is used to estimate the burst capacity of corroded pipelines under the combined internal pressure and longitudinal compression. Therefore, a total of 1905 FEA cases were generated based on the parameters described in Section 4.3.1 and are used as the database to train and validate the ANN model. In this study, 1800 cases randomly selected from the 1905 FEA cases are used as the training dataset for the ANN training, and the remaining 105 cases are used to validate the well-trained ANN model. After 10,000 training epochs, the mean-square error is 0.000047 and the performance of the proposed ANN algorithm on the training database (1800 cases) is excellent as shown in Fig. 4.8.

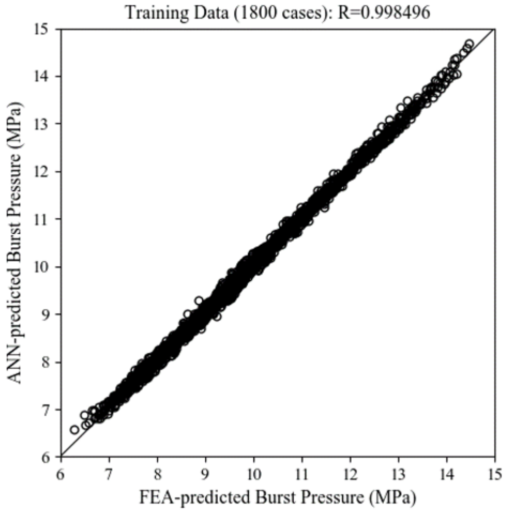

Figure 4.8 ANN training results

4.4.3 Validation with FEA Results

The 105 arbitrarily selected analysis cases, which are not used in the training process, are used to validate the well-trained ANN model. From the unit plot shown in Fig. 4.9, we can see an excellent agreement between the ANN model-predicted burst capacities and corresponding FEA-predicted capacities.

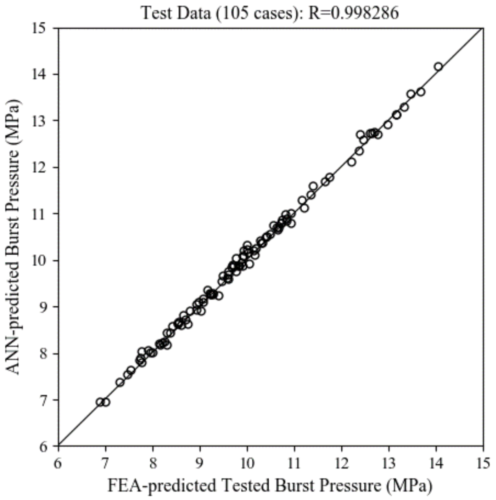

Figure 4.9 Comparison between the ANN model-predicted and FEA-predicted burst capacities for 105 validation cases

4.4.4 Validation with DNV test results

Further validations of the ANN-based model are carried out by employing the full-scale burst tests conducted by DNV (Bjørnøy et al., 2000). Note that a total of 12 burst test specimens are reported in (Bjørnøy et al., 2000). Specimens #10, 11, and 12 are excluded because each of them contains a single full-circumferential defect to simulate the girth weld corrosion defect, which is out of the scope of this study. The test specimens have a 324 mm nominal outside diameter, a 10.3 mm nominal wall thickness, and are made of Grade X52 steel with the yield and tensile strengths equal to 380 and 514 MPa, respectively, determined from the tensile coupon test. The defect geometries and the magnitudes of the longitudinal compressive force (F_a) or bending moment (M_b) for the test specimens are summarized in Table 4.4. Note that the defects in the test specimens are artificially-induced, rectangular-shaped, whereas the ANN-based model is developed based on semi-ellipsoidal-shaped defects. Therefore, the burst prediction through the ANN model is also performed after converting the rectangular-shaped defect into equivalent semi-ellipsoidal shape. In the converting process, the depth and width of the rectangular-shaped defect are kept constant while the defect length is converted to the length of the equivalent semi-ellipsoidal-shaped defect by maintaining the total volume of the metal loss.

Table 4.4 Burst prediction compared with test results

Specimen ID	d (mm)	l (mm)	w (mm)	M_b or F_a	P_{test} (MPa)	P_{ANN} (MPa)	P_{test}/P_{ANN}
1	5.15	243	154.5	--	23.20	20.89	1.11
2	5.15	243	154.5	129 kNm	21.90	20.76	1.05
3	5.15	243	154.5	212 kNm	19.50	19.77	0.99
4	3.09	121.5	30.9	73 kNm	29.00	29.3	0.99
5	3.09	121.5	30.9	2563 kN	28.60	26.98	1.06
6	3.09	121.5	30.9	2943 kN	28.70	25.7	1.12
7	5.15	243	30.9	3000 kN	18.60	20.6	0.90
8	5.15	243	30.9	--	22.00	20.51	1.07
9	0.86	243	30.9	2070 KN	12.30	14.27	0.86
			Mean				1.02
			COV				8.28%

The comparison between the ANN-predicted burst capacities (P_{ANN}) and the testing results (P_{test}) is shown in Table 4.6 with the corresponding unit plot shown in Fig. 4.10. The mean value of the test-to-ANN-predicted burst capacity ratios is 1.02, with the corresponding COV value equal to 8.28%. The results indicate a good accuracy of the ANN model. It should be noted that the yield strength as opposed to the specified minimum yield strength (SMYS) was used in the ANN model to predict the burst pressure. This consideration was to isolate the uncertainties associated with other parameters and quantify the uncertainty associated with the model only. To provide safety of using the assessment model (i.e. in the model implementation stage), the SMYS will be used in predicting the burst pressure and a safety factor will be further utilized to provide safety. A data-driven validation process for safe implementation of an assessment model is reported in IPC 2020 (Kariyawasam et al., 2020).

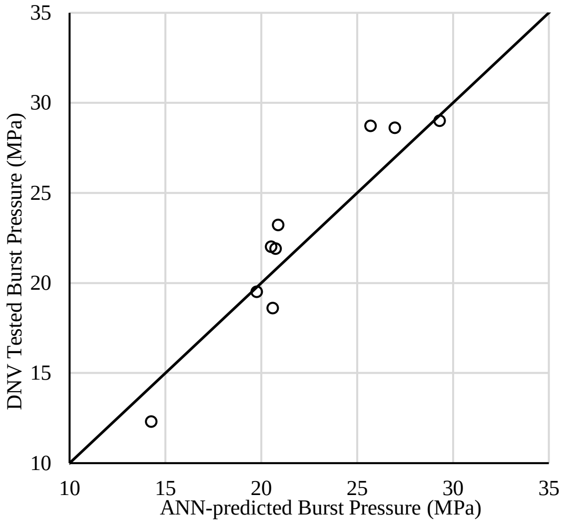

Figure 4.10 Comparison between ANN burst capacities and testing results

4.5 Conclusion

This chapter investigated the burst capacity of corroded pipelines under combined internal pressure and longitudinal compression loading condition based on extensive parametric 3D elastic-plastic FEA and artificial neural network technique. The accuracy of the FE model and failure criterion adopted in the analysis are validated by comparing FEA-predicted burst capacities with corresponding test results for full-scale pipe specimens containing semi-ellipsoidal defects reported in the literature.

Extensive parametric FEA is carried out to investigate the reduction of the burst capacity of pipelines containing individual corrosion defects under combined internal pressure and longitudinal compression by employing the semi-ellipsoidal defect idealization. It is observed that the longitudinal compressive stress can markedly reduce the burst capacity of corroded pipelines. The adverse effect of the compressive stress on the burst capacity is the strongest for wide, relatively shallow defects, and relatively insensitive to the defect length.

Based on the parametric FEA results, an ANN model is developed in the open-source platform PYTHON, to predict the burst capacity of pipelines containing single corrosion defects under internal pressure only or combined internal pressure and axial compression. The ANN model is validated using 105 FEA cases and 9 full-scale burst tests conducted by DNV and the results indicates good accuracy of the ANN model.

REFERENCES

Al-Owaisi, S., Becker, A. A., Sun, W., Al-Shabibi, A., Al-Maharbi, M., Pervez, T., & Al-Salmi, H., 2018. An experimental investigation of the effect of defect shape and orientation on the burst pressure of pressurised pipes. Engineering Failure Analysis, 93, 200-213.

ASME, 1991. “Manual for determining the remaining strength of corroded pipelines- a supplement to ASME B31 code for pressure piping”, The American Society of Mechanical Engineers, New York.

Bao, J., Zhang, S., Zhou, W., & Zhang, S., 2018. Evaluation of Burst Pressure of Corroded Pipe Segments Using Three-Dimensional Finite Element Analyses. In 2018 12th International Pipeline Conference (pp. V001T03A043-V001T03A043). American Society of Mechanical Engineers.

Benjamin, A.C., 2008. Prediction of the Failure Pressure of Corroded Pipelines Subjected to a Longitudinal Compressive Force Superimposed to the Pressure Loading, in: 2008

7th Int. Pipeline Conf. Vol. 2, ASME: pp. 179–189.

Bjørnøy, O. H., Sigurdsson, G., & Cramer, E., 2000. Residual strength of corroded pipelines, DNV test results. In The Tenth International Offshore and Polar Engineering Conference. International Society of Offshore and Polar Engineers.

Chouchaoui, B., 1995. Evaluating the remaining strength of corroded pipelines, PhD thesis, University of Waterloo.

Cronin, D. S., 2000. Assessment of corrosion defects in pipelines, PhD thesis, University of Waterloo.

Canadian Standard Association, (CSA), 2019. Oil and gas pipeline systems. CSA standard Z662-19. *Mississauga, Ontario, Canada*.

Dassault Systèmes, D. S., 2016. Abaqus analysis user's guide. Technical Report Abaqus 2016 Documentation, Simulia Corp.

Det Norske Veritas (DNV), 2017. “Recommended practice DNV-RP-F101, corroded pipelines”, Hovic, Norway.

Dowling, N. E., 2007. Mechanical behavior of materials. Prentice Hall, New Jersey.

Haykin, S., 2009. Neural networks and learning machines (Vol. 3). Upper Saddle River, NJ, USA: Pearson

Karimian, S. A., 2006. Response of buried steel pipelines subjected to longitudinal and transverse ground movement (Doctoral dissertation, University of British Columbia).

Kariyawasam, S., Zhang, S., & Yan, J., 2020, September. Safe Implementation of a Corrosion Assessment Model, a Data Driven Validation. In *Proceedings of the 2020 13th International Pipeline Conference*.

Kiefner, J. and Vieth, P., 1989. “A modified criterion for evaluating the remaining strength of corroded pipe, Final Report on Project PR 3-805”, Battelle Memorial Institute, Columbus, OH, 1989.

Kiefner, J. and Vieth, P., 1990. “PC program speeds new criterion for evaluating corroded pipe”, Oil and Gas Journal, August 20, 1990. pp. 91-93.

Liu, J., Chauhan, V., Ng, P., Wheat, S., & Hughes, C., 2009. Remaining strength of corroded pipe under secondary (biaxial) loading (No. Report No. R9068). GL Industrial Services UK Ltd.

Meidani, M., Meguid, M. A., & Chouinard, L. E., 2017. Evaluation of soil–pipe interaction under relative axial ground movement. Journal of Pipeline Systems Engineering and Practice, 8(4), 04017009.

Meidani, M., Meguid, M. A., & Chouinard, L. E., 2018. Estimating earth loads on buried pipes under axial loading condition: insights from 3D discrete element analysis. International Journal of Geo-Engineering, 9(1), 5.

Mondal, B. C., & Dhar, A. S., 2019. Burst pressure of corroded pipelines considering combined axial forces and bending moments. Engineering Structures, 186, 43-51.

Ripley, B.D., 1996. Pattern Recognition and Neural Networks, Cambridge University Press, Cambridge.

Smith, M. Q., & Waldhart, C. J., 2000. Combined loading tests of large diameter corroded pipelines. In 2000 3rd International Pipeline Conference. American Society of Mechanical Engineers Digital Collection.

Stephens, D. R., & Leis, B. N., 2000. Development of an alternative criterion for residual strength of corrosion defects in moderate-to high-toughness pipe. In 2000 3rd International Pipeline Conference (pp. V002T06A012-V002T06A012). American Society of Mechanical Engineers.

Taylor, N., Clubb, G., & Matheson, I., 2015. The Effect of Bending and Axial Compression on Pipeline Burst Capacity. In SPE Offshore Europe Conference and Exhibition. Society of Petroleum Engineers.

Wang, L., & Zhang, Y., 2011. Plastic collapse analysis of thin-walled pipes based on unified yield criterion. International Journal of Mechanical Sciences, 53(5), 348-354.

Wijewickreme, D., Karimian, H., & Honegger, D., 2009. Response of buried steel pipelines subjected to relative axial soil movement. Canadian Geotechnical Journal, 46(7), 735-752.

Zhang, S., & Zhou, W., 2020. Assessment of effects of idealized defect shape and width on the burst capacity of corroded pipelines. Thin-Walled Structures, 154, 106806.

Zhu, X. K., & Leis, B. N., 2004. Strength criteria and analytic predictions of failure pressure in line pipes. International Journal of Offshore and Polar Engineering, 14(02), 125-131.

Zhu, X. K., & Leis, B. N., 2005. Influence of yield-to-tensile strength ratio on failure assessment of corroded pipelines. Journal of Pressure Vessel Technology, 127(4), 436-442.

Zurada, J.M., 1992. Introduction to Artificial Neural System, PWS, Boston.

5 A Burst Capacity Model for Corroded Pipelines Subjected to Combined Internal Pressure and Longitudinal Compression

5.1 Introduction

Corrosion defects threaten the structural integrity of oil and gas pipelines as they cause thinning of the pipe wall and therefore reduce the pressure containment capacity, i.e. burst capacity, of the pipeline. Corroded in-service pipelines may be subjected to longitudinal tensile or compressive forces and bending moments resulting from, for example, ground movement or formation of free spans (Karimian, 2006; Wijewickreme et al., 2009; Meidani et al., 2017, 2018), in addition to internal pressures. A displacement-controlled longitudinal loading (strain) has been reported in (Taylor, 2015; Cunha, 2016) to have a negligible effect on the burst capacity of corroded pipelines. On the other hand, the burst capacity of a corroded pipeline under the load-controlled longitudinal compression and internal pressure, referred to, for brevity, as combined loads in the following, can be markedly lower than that of the pipeline under the internal pressure only as confirmed by both experimental and numerical studies reported in the literature (Chouchaoui, 1995; Bjørnøy et al., 2000; Smith and Waldhart, 2000; Liu et al., 2009; Mondal, 2018; Zhang and Zhou, 2020a). Note that the longitudinal compression may result from a compressive force or bending moment (with the corrosion defect located on the compression side of the bending).

Finite element analyses (FEA) are conducted in (Liu et al., 2009) to investigate the burst capacity of corroded pipelines subjected to the internal pressure combined with axial compressive force or bending moment, and interaction diagrams (or failure loci) for the burst capacity and compression are developed. A similar study was conducted by Mondal and Dhar as reported in (Mondal and Dhar, 2019). However, the interaction diagrams developed in (Liu et al., 2009; Mondal and Dhar, 2019) are associated with specific pipe material and geometric properties and defect dimensions as considered in the FEA, which markedly restricts their applicability in practice. In (Shim et al., 2005; Yu et al., 2012; Chen et al., 2014; Mohd et al., 2015; Gao et al., 2018; Cai et al., 2018, 2019), full-scale burst tests and FEA are employed to investigate the capacity of corroded pipelines under combined loads; however, these studies were focused on the effect of the internal pressure on the bending capacity of corroded pipelines as opposed to the influence of the axial force and bending moment on the burst capacity.

Widely-used semi-empirical fitness-for-service (FFS) assessment models for corroded pipelines, such as the B31G (1991), B31G Modified (Kiefner and Vieth, 1989), CSA (2019), RSTRENG (Kiefner and Vieth, 1990) and SHELL92 (Ritchie and Last, 1995) models, consider the internal pressure only. Practical FFS assessment models for corroded pipelines under combined loads have been reported in the literature; the two most well-known models are the one recommended in DNV RP-F101 (DNV, 2017) and the RPA-PLLC model proposed in (Benjamin, 2008) (RPA stands for the rectangular parabolic area, and PLLC stands for the pressure loading plus longitudinal compression). Both models include a relatively high threshold compressive stress (typically greater than 30% of the pipe yield strength), below which the compressive stress is considered to have no effect on the burst capacity. This however is inconsistent with observations obtained in recent studies (Liu et al., 2009; Mondal and Dhar, 2019; Zhang and Zhou, 2020a). Results of FEA (Mondal and Dhar, 2019) indicate that a compressive stress equal to about 15% of the pipe yield strength can result in a 8~17% reduction in the burst capacity of corroded pipelines. This suggests that the DNV and RPA-PLLC models do not adequately capture the effect of compressive stress on the burst capacity of corroded pipelines. Arumugam et al. (2020) proposed an empirical equation to evaluate the burst capacity of corroded pipelines under combined loads based on multivariate nonlinear regression analyses of parametric FEA results. End-capped finite element pipe models are considered in (Arumugam et al., 2020); however, the internal pressure-induced axial tensile stress corresponding to the end-capped boundary condition is not accounted for in the proposed empirical burst capacity model. This casts doubts on the validity and accuracy of the model for practical applications. Based on a limited number of parametric FEA cases, Zhou et al. (2018) proposed an equation to evaluate the burst capacity of corroded pipelines under high longitudinal compressive strains. The equation is applicable under limited conditions in terms of the size of the corrosion defect on the pipeline. Furthermore, the proposed equation is unsuitable for corroded pipelines under load-controlled longitudinal compression.

The objective of the present study in this chapter is to develop a new burst capacity model for corroded pipelines subjected to combined loads. A recently-developed semi-empirical burst capacity model (Zhang and Zhou, 2021) for corroded pipelines under internal pressure only is multiplied by a correction factor to account for the impact of the longitudinal compression on the burst capacity. The correction factor, which is a function of the corrosion defect size as well as magnitude of the longitudinal compressive stress, is developed by using MATLAB (2018) to carry out multivariate nonlinear regression analyses of results from a large set of parametric FEA; the accuracy of FEA is validated by full-scale tests reported in the literature. The corrosion defect in the finite element model is idealized as semi-ellipsoidal-shaped as it has been demonstrated (Zhang and Zhou, 2020b) that such an idealization better approximates the geometry of real corrosion defects than the commonly used rectangular (or cubic) idealization. The proposed burst capacity model is further validated by parametric FEA and full-scale burst tests. The rest of this chapter is organized as follows: Section 5.2 briefly reviews the DNV and RPA-PLLC models, in particular the effect of the longitudinal compression on the burst capacity; details of the proposed burst capacity model are described in Section 5.3, and Section 5.4 presents the validation of the proposed model and its comparison with the DNV and RPA-PLLC models, followed by conclusions in Section 5.5.

5.2 Review of DNV and RPA-PLLC models

The predictive equations associated with the DNV (DNV, 2017) and RPA-PLLC (Benjamin, 2008) models are given as follows.

DNV model

$$P_{DNV}^{comb} = f_{DNV} P_{DNV} = f_{DNV} \frac{2t\sigma_f}{(D-t)} \frac{1-\frac{d}{t}}{1-\frac{d}{tM_1}} \tag{5.1}$$

$$f_{DNV} = min\left(1,\ \frac{1+\frac{\sigma_a}{\sigma_u}\frac{1}{1-\frac{dw}{\pi Dt}}}{1-\frac{1}{2\left(1-\frac{dw}{\pi Dt}\right)}\frac{1-\frac{d}{t}}{1-\frac{d}{tM_1}}}\right) \tag{5.2}$$

$$M_1 = \sqrt{1 + \frac{0.31l^2}{Dt}} \tag{5.3}$$

where P_{DNV}^{comb} and P_{DNV} are burst capacities of the corroded pipeline under combined loads and internal pressure only, respectively; f_{DNV} is the correction factor to account for the effect of the axial compression on the burst capacity; D and t are the pipe outside diameter and wall thickness, respectively; σ_f is the flow stress, assumed to equal the ultimate tensile strength (σ_u) of the pipe steel; d, l and w denote the defect depth (in the through wall thickness direction), length (in the pipe longitudinal direction) and width (in the pipe circumferential direction), respectively; M_1 is the Folias (bulging) factor, and σ_a is the nominal longitudinal compressive stress (i.e. the longitudinal compressive stress computed by assuming the pipeline to be corrosion-free), expressed as a negative value.

RPA-PLLC model

$$P_{RPA}^{comb} = f_{RPA} P_{RPA} = f_{RPA} \frac{2t\sigma_f}{D} \frac{1-\alpha_{area}\frac{d}{t}}{1-\alpha_{area}\frac{d}{tM_2}} \tag{5.4}$$

$$f_{RPA} = min\left(1,\ \frac{1+\frac{\sigma_a}{\sigma_y+69}\frac{1}{1-\frac{dw}{\pi Dt}}}{1-\frac{1}{2\left(1-\frac{dw}{\pi Dt}\right)}\frac{1-\alpha_{area}\frac{d}{t}}{1-\alpha_{area}\frac{d}{tM_2}}}\right) \tag{5.5}$$

$$\alpha_{area} = \begin{cases} 0.85 & \frac{l^2}{Dt} \le 20 \\ 1 - \frac{9.6\times10^6}{\left(\frac{l^2}{Dt}\right)^6} & \frac{l^2}{Dt} > 20 \end{cases} \tag{5.6}$$

$$M_2 = \begin{cases} \sqrt{1 + 0.6275\frac{l^2}{Dt} - 0.003375\left(\frac{l^2}{Dt}\right)^2} & \frac{l^2}{Dt} \le 20 \\ 2.1 + 0.07\frac{l^2}{Dt} & \frac{l^2}{Dt} > 20 \end{cases} \tag{5.7}$$

where P_{RPA}^{comb} and P_{RPA} are burst capacities of the corroded pipeline under combined loads and internal pressure only, respectively, associated with the RPA-PLLC model; f_{RPA} is the correction factor to account for the effect of the axial compression on the burst capacity; σ_f is the flow stress, assumed to equal the yield strength (σ_y) of the pipe steel plus 69 MPa;

α_{area} is a factor that depends on the area of the metal loss projected on the longitudinal plane, and M_2 is the Folias (bulging) factor.

To demonstrate the correction factors quantified by the DNV (Eq. (5.2)) and RPA-PLLC (Eq. (5.5)) models, we consider a representative pipeline made of the X65 steel (σ_y and σ_u equal to 448 and 531 MPa, respectively) with D = 610 mm and t = 7.1 mm (D/t = 86). The values of f_{DNV} and f_{RPA} for the pipeline are plotted versus $|\sigma_a|/\sigma_y$ in Fig. 5.1 for different values of the defect depth, length and width. The results in Figure 5.1 indicate that f_{DNV} and f_{RPA} are equal to unity, i.e. the longitudinal compression resulting in no reduction of the burst capacity, if $|\sigma_a|/\sigma_y$ is lower than about 0.35 for wide ranges of the defect depth, length and width. These results are inconsistent with observations reported in (Liu et al., 2009; Mondal and Dhar, 2019; Zhang and Zhou, 2020a), as already described in the Introduction. It is noted that the defect width has a negligible effect on f_{DNV} and f_{RPA} as suggested in Figs. 5.1(e) and 5.1(f). This again is inconsistent with the previous studies (Stephens et al., 1995; Zhang and Zhou, 2020a). For example, it is pointed out in (Stephens et al., 1995) that the defect width is an important parameter to consider for corroded pipelines under combined loads.

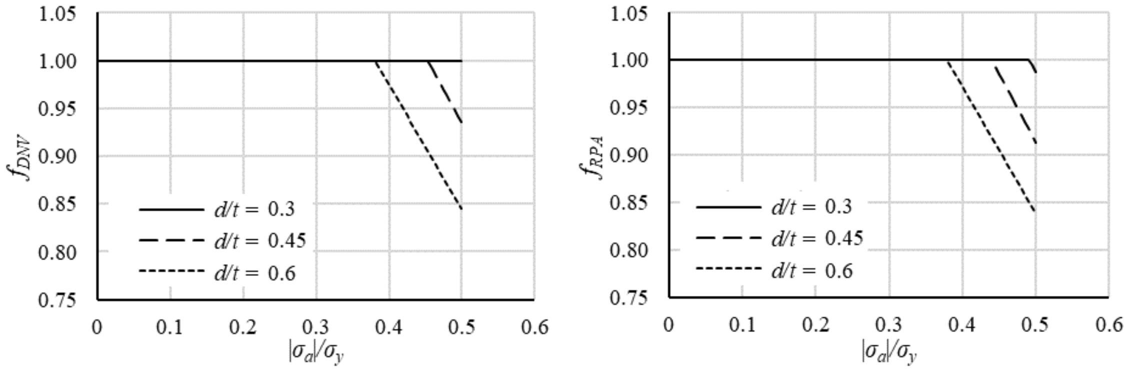

(a) DNV, $l^2/(Dt)$ = 5, w/l = 0.5

(b) RPA-PLLC, $l^2/(Dt)$ = 5, w/l = 0.5

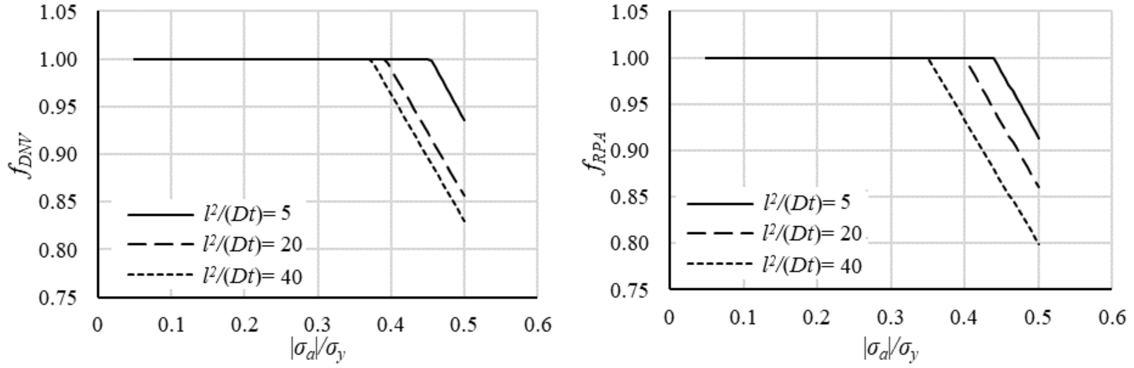

(c) DNV, *d/t* = 0.45, *w/l* = 0.5

(d) RPA-PLLC, *d/t* = 0.45, *w/l* = 0.5

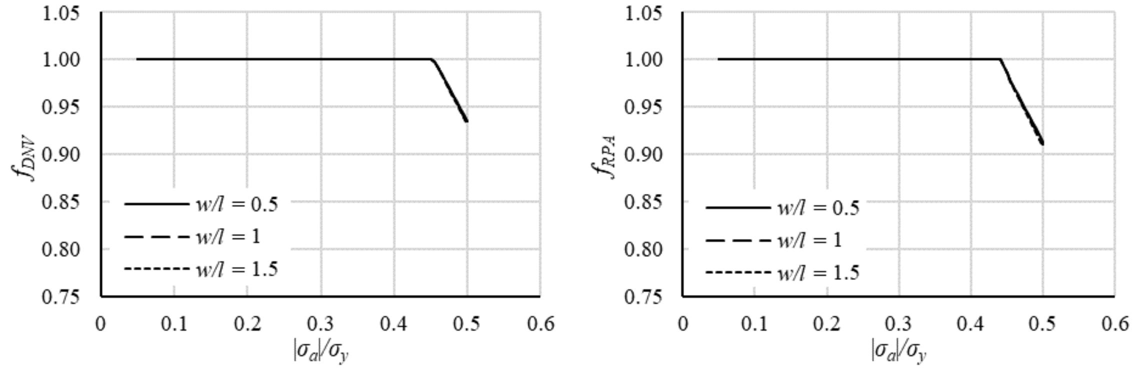

(e) DNV, *d/t* = 0.45, $l^2/(Dt)$ = 5

(f) RPA-PLLC, *d/t* = 0.45, $l^2/(Dt)$ = 5

Figure 5.1 Values of f_{DNV} and f_{RPA} corresponding to different defect sizes and values of $|\sigma_a|/\sigma_y$ for a representative X65 pipeline with D = 610 mm and t = 7.1 mm

5.3 Proposed burst capacity model

5.3.1 Basic equation

Similar to the DNV and RPA-PLLC models, the burst capacity model proposed in the present study considers that the burst capacity of a corroded pipeline under combined loads, P_b^{comb}, is expressed as the burst capacity of the pipeline under internal pressure only, P_b, multiplied by a correct factor, f_{comb}, to account for the effect of the longitudinal compressive stress, i.e.

$$P_b^{comb} = f_{comb} P_b \tag{5.8}$$

The value of P_b is evaluated using Eq. (5.9), which is proposed in a recent study (Zhang and Zhou, 2021) and follows the well-known NG-18 format (Kiefner, 1969). The accuracy of Eq. (5.9) for corroded pipelines under internal pressure only has been validated by extensive parametric FEA (Zhang and Zhou, 2021) and is shown to be markedly higher than those of commonly used models such as B31G, B31G Modified, CSA, RSTRENG and SHELL92. Therefore, Eq. (5.9) provides a good basis for predicting the burst capacity of corroded pipelines under combined loads.

$$P_b = f_w \left(\frac{1}{\sqrt{3}}\right)^{n+1} \frac{4t\sigma_u}{D} \frac{1-\frac{d}{t}}{1-\frac{d}{tM}} \tag{5.9}$$

$$f_w = \begin{cases} 1 & \frac{w}{l} \leq 0.25 \\ \sqrt{1 + \left[0.6215\frac{d}{t}\left(\frac{w}{l} - 0.25\right) - 0.2866\frac{d^2}{t^2}\left(\frac{w}{l} - 0.25\right)^2\right] e^{-0.01719\frac{l^2}{Dt}}} & \frac{w}{l} > 0.25 \end{cases} \tag{5.10}$$

$$M = \sqrt{1 + 0.3498 e^{\frac{d}{t}}\left(\frac{l^2}{Dt}\right)^{-0.01792\frac{d}{t}} + 0.24\frac{d}{t}\frac{l^2}{Dt} - 0.001993\left(\frac{d}{t}\frac{l^2}{Dt}\right)^2} \tag{5.11}$$

In Eqs. (5.9) – (5.11), *n* is the strain hardening exponent of the pipe steel; *M* is the Folias factor, and f_w is the corrosion width factor to account for the beneficial effect of the defect width on the burst capacity of corroded pipelines (Zhang and Zhou, 2021). Equation (5.11) for computing the Folias factor is more advantageous than the Folias factor equations in the DNV and RPA-PLLC models (i.e. Eqs. (5.3) and (5.7)) in that Eq. (5.11) incorporates the defect depth and length, and therefore more accurately captures the bulging effect for a part-through wall corrosion defect. Details of the development of Eqs. (5.9), (5.10) and (5.11) are described in (Zhang and Zhou, 2021). The value of *n* can be estimated from the following empirical equation (Zhu and Leis, 2005), if the stress-strain relationship of the pipe steel is unavailable.

$$n = 0.239\left(\frac{1}{\sigma_y/\sigma_u} - 1\right)^{0.596} \tag{5.12}$$

5.3.2 Correction factor f_{comb} for longitudinal compression

In this study, the correction factor (f_{comb}) in Eq. (5.8) to account for the influence of longitudinal compression on the burst capacity is developed based on the results of 477 parametric FEA cases. The pipeline considered in the parametric FEA is assumed to be made of the X65 steel (σ_y = 448 MPa and σ_u = 531 MPa) with *D* = 610 mm and *t* = 7.1 mm. A power-law stress-strain relationship for the pipe steel is adopted in the FEA, with the value of n estimated from Eq. (5.12). The corrosion defect on the pipe model is idealized to be semi-ellipsoidal-shaped, which is consistent with the shape of the corrosion defect considered in the development of Eq. (5.9) for P_b (Zhang and Zhou, 2021). The corrosion defect geometry considered in the parametric cases include the depth (*d/t*) equal to 0.3, 0.45 or 0.6 (*d* is the maximum depth of the semi-ellipsoid), normalized defect length

$l^2/(Dt)$ equal to 2, 5, 15, 20, 30, 40, 50 or 60, and with-to-length ratio (w/l) equal to 0.25, 0.5, 0.75, 1, 1.25, 1.5, 1.75 or 2. The maximum w/l value considered in FEA is 2 for $l^2/(Dt)$ = 2 and 5, 1.75 for $l^2/(Dt)$ = 15, and 1.5 for the other values of $l^2/(Dt)$.

The commercial FEA package ABAQUS (Dassault Systèmes, 2016) is employed to develop and analyze the finite element models. Four layers of the 8-node solid elements (C3D8) are used through the ligament of each defect area to ensure the high stress gradient along the radial direction of the defect area to be accurately captured. The mesh in the FEA model is transitioned from a high density in the defected region to a low density in the defect-free region in the longitudinal, circumferential and radius directions. The mesh densities for the models are selected following mesh convergence studies. Two representative finite element models are depicted in Fig. 5.2. The von Mises yield criterion, associated flow rule and isotropic hardening rule are adopted to characterize the material nonlinearity. The finite-strain configuration is employed to capture the geometrical non-linearity in the analysis.

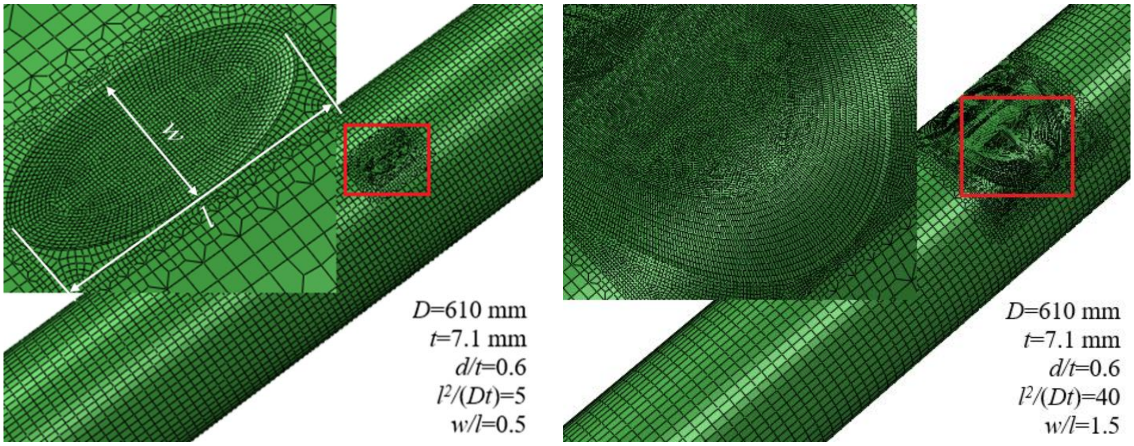

Figure 5.2 Representative finite element mesh used in the analysis

Three loading scenarios are considered in the FEA: the base case in which the internal pressure is the only load, and the other two scenarios involving combined loads with σ_a/σ_y = -0.15 and -0.3 respectively. In the base case, the pipe model is assumed to be longitudinally fully-restrained and no additional axial stress is involved other than that induced by internal pressure due to the boundary condition. For the two scenarios involving combined loads, the longitudinal compression is introduced by applying a uniform compressive stress (σ_a) on the corrosion-free pipe cross section at the free end of the pipe model, while keeping the other end of the pipe model longitudinally restrained. A total of 159 cases involving the internal pressure only are analyzed, whereas 318 cases involving combined loads are analyzed. The burst capacity of a given analysis case (involving internal pressure only or combined loads) is determined as the pressure at which the nodal von Mises stress anywhere within the corrosion defect reaches the true stress corresponding to σ_u. The finite element model as well as failure criterion for determining the burst capacity has been validated by using seven full-scale burst tests of pipe specimens containing semi-ellipsoidal-shaped defects reported in (Al-Owaisi et al., 2018). The pipe specimens are made of the X52 steel with the material properties (E =182 GPa, σ_y = 372 MPa, σ_u = 497.7 MPa and n = 0.20) obtained from the tensile coupon test results reported in (Al-Owaisi et al., 2018). The outside diameters (D) and wall thicknesses (t) of the test specimens are summarized in Table 5.1 as well as the FEA predicted burst capacities together with the actual burst capacities from tests. As demonstrated in Table 5.1, the mean and coefficient of variation (COV) of ratios of test-to-FEA predicted burst capacities are 1.01 and 1.4%, respectively. This provides a strong validation of the finite element model and burst criterion employed in the analysis.

Table 5.1 Comparison of FEA burst prediction and test results

Specimen ID	D (mm)	t (mm)	P_{test} (MPa)	P_{FEA} (MPa)	P_{test}/P_{FEA}
18	508	9.7	19.55	19.83	0.99
19		9.85	19.11	19.15	1.00
20		9.7	19.59	19.39	1.01
21		9.7	19.65	19.48	1.01
22		9.75	20.08	19.65	1.02
23		9.8	20.27	19.80	1.02
30		9.7	20.68	20.06	1.03
		Mean			1.01
		COV			1.4%

The value of f_{comb} is considered to depend on the defect size (i.e. depth, length and width) as well as σ_a/σ_y. To develop an empirical equation to evaluate f_{comb}, the burst capacity of a given parametric FEA case involving combined loads, denoted by P_{b-FEA}^{comb}, is normalized by the burst capacity (P_{b-FEA}) of the corresponding base case with the same defect geometry. Given the values of $f_{comb}^{FEA} = P_{b-FEA}^{comb}/P_{b-FEA}$ for a total of 318 analysis cases, the following equation for f_{comb} is developed based on nonlinear curve fitting:

$$f_{comb} = 1 + 0.7567M\frac{\sigma_a}{\sigma_y}q^{0.3295}e^{\left(-0.8509\left(\frac{d}{t}\right)^2\frac{l}{\sqrt{Dt}}\right)} \quad (q = \max\{w/l, 0.25\}) \qquad (5.13)$$

where M is evaluated using Eq. (5.11). Equation (5.13) is applicable for $w/l \le 2$, $2 \le l^2/(Dt) \le 60$ and $-0.3 \le \sigma_a/\sigma_y \le 0$. The use of parameter q in Eq. (5.13) is compatible with the way w/l is incorporated in P_b (i.e. Eq. (10)). Figure 5.3 depicts the fitting accuracy of Eq. (5.13), where f_{comb} values obtained from Eq. (5.13) are compared with the corresponding values of f_{comb}^{FEA}. For brevity, only the cases with $l^2/(Dt)$= 20 and 40 (w/l=0.25, 0.5, 0.75, 1, 1.25 and 1.5) with d/t = 0.3, 0.45 and 0.6 and σ_a/σ_y = -0.15 and -0.3 are shown in Fig. 5.3. The fitting accuracy of Eq. (5.13) for the other cases is similar. As depicted in Fig. 5.3, the f_{comb} values corresponding to σ_a/σ_y = -0.3 are lower than those corresponding to σ_a/σ_y = -0.15 (all else being the same). This indicates that the longitudinal compression effect on the burst capacity becomes stronger as the compressive stress increases. All else being the same, f_{comb} increases as d/t increases, i.e. the longitudinal compression effect weakens as d/t increases. This is because the corrosion-free region for the cases with deep defects is generally elastic at burst. As a result, the longitudinal compressive load is mainly resisted by the corrosion-free region and has a small effect on the corrosion defect. For the cases with shallow defects, the relatively high burst capacity means that both the corrosion-free and corroded regions are in the plastic regime at burst; as a result, the axial load is distributed more uniformly between the corrosion-free and corroded regions. Therefore, the longitudinal compression effect is stronger for shallow defects. The longitudinal compression effect is stronger, i.e. f_{comb} decreases, as the width-to-length ratio increases. This is more evident for shallow defects with a high level of longitudinal compression. The influence of the defect length on f_{comb} is relatively weak compared with that of the defect depth and width-to-length ratio.

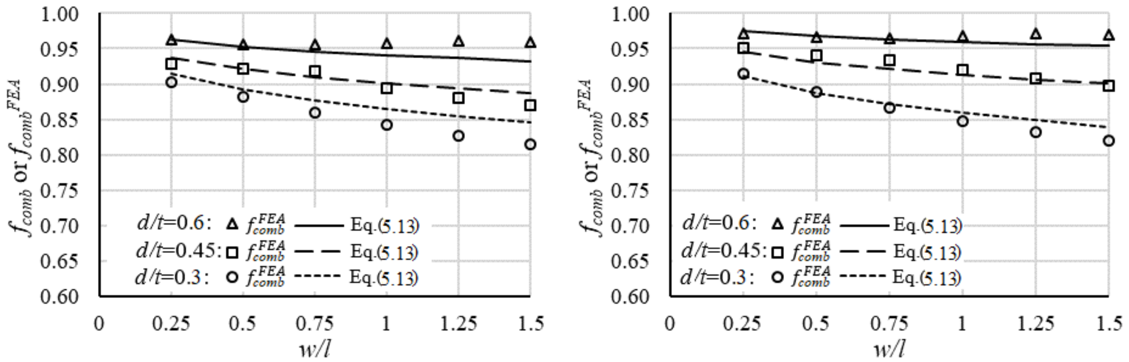

(a) $l^2/(Dt)=20$, $\sigma_a/\sigma_y = -0.15$ (b) $l^2/(Dt)=40$, $\sigma_a/\sigma_y = -0.15$

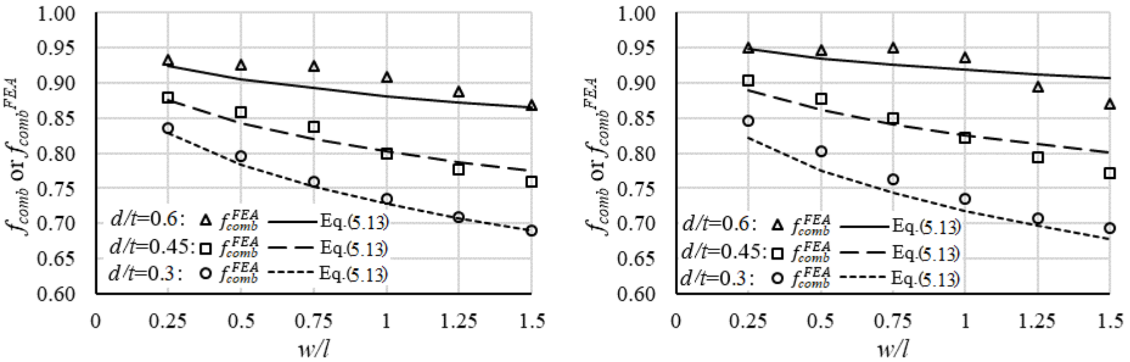

(c) $l^2/(Dt)=20$, $\sigma_a/\sigma_y = -0.3$ (d) $l^2/(Dt)=40$, $\sigma_a/\sigma_y = -0.3$

Figure 5.3 Comparison of f_{comb} and f_{comb}^{FEA} for different values of d/t, $l^2/(Dt)$, w/l and σ_a/σ_y

By substituting f_{comb} (Eq. (5.13)) into Eq. (5.8), the burst capacities of corroded pipelines under combined loads can be predicted. Figure 5.4 shows that the burst capacities predicted by Eq. (5.8) are in good agreement with the corresponding burst capacities obtained from FEA for the 318 analysis cases involving combined loads used to develop Eq. (5.13).

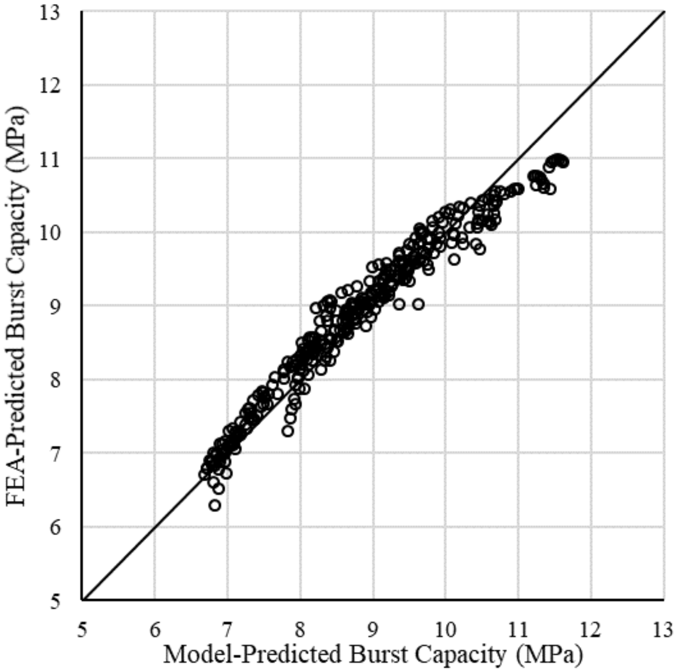

Figure 5.4 Comparison of burst capacities predicted by Eq. (5.8) and FEA for the 318 parametric FEA cases

5.4 Validation of the proposed burst capacity model

5.4.1 Validation with FEA results

A total of 1431 additional parametric FEA cases involving three different pipes are employed to validate the proposed burst capacity model, i.e. Eqs. (5.8)-(5.13). The corresponding pipe attributes, i.e. D, t, steel grade, E, σ_y and σ_u, are summarized in Table 5.2 and representative of typical oil and gas transmission pipelines. The 1431 analysis cases consist of 477 cases involving internal pressure only and 954 cases involving combined loads (477 cases with σ_a/σ_y = -0.15 and 477 cases with σ_a/σ_y = -0.30). Each analysis case contains a semi-ellipsoidal corrosion defect with d/t equal to 0.3, 0.45 or 0.6, $l^2/(Dt)$ equal to 2, 5, 15, 20, 30, 40, 50 or 60, and w/l equal to 0.25, 0.5, 0.75, 1, 1.25, 1.5, 1.75 or 2. The maximum w/l value considered in FEA is 2 for $l^2/(Dt)$ = 2 and 5, 1.75 for $l^2/(Dt)$ = 15, and 1.5 for the other values of $l^2/(Dt)$. Figure 5.5 depicts the burst capacities predicted by FEA (P_{b-FEA}^{comb}) and the proposed model (P_b^{comb}) for the 954 analysis cases involving combined loads. For comparison, the burst capacities predicted by the DNV and

RPA-PLLC models (P_{DNV}^{comb} and P_{RPA}^{comb}) are also shown in the figure. The predictions by the proposed model are in good agreement with the FEA predictions as shown in Fig. 5.5(a), in which the data points straddle the 1:1 line (the diagonal line) within a small band. The mean and coefficient of variation (COV) of the FEA-to-model prediction ratios for the 954 cases corresponding to the DNV, RPA-PLLC and proposed models are summarized in Table 5.3. The results in Table 5.3 clearly demonstrate the high accuracy of the proposed model and its advantages over the other two models: the mean and COV of the FEA-to-predicted burst capacity ratios are 1.01 and 3.1%, respectively. The DNV and RPA-PLLC models lead to on average more conservative predictions with greater variability: the COV of the FEA-to-model prediction ratios equal to 10.5% and 11.4%, respectively (Figs. 5.5(b) and 5.5(c)).

Table 5.2 Pipe attributes considered in parametric FEA

Pipe	Steel grade	*D* (mm)	*t* (mm)	*E* (GPa)	σ_y (MPa)	σ_u (MPa)
1	X52	406	6.0	200	359	455
2	X60	508	6.4	200	414	517
3	X70	914	10.6	200	483	565

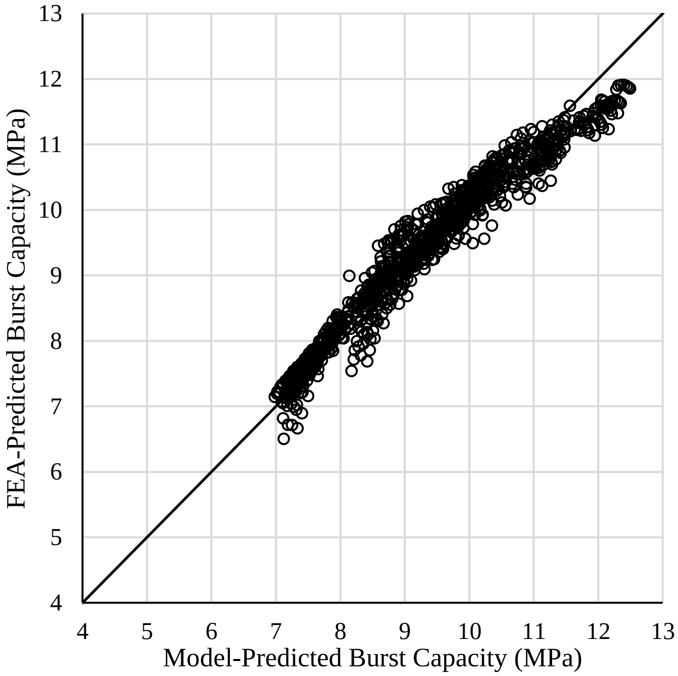

(a) Proposed model

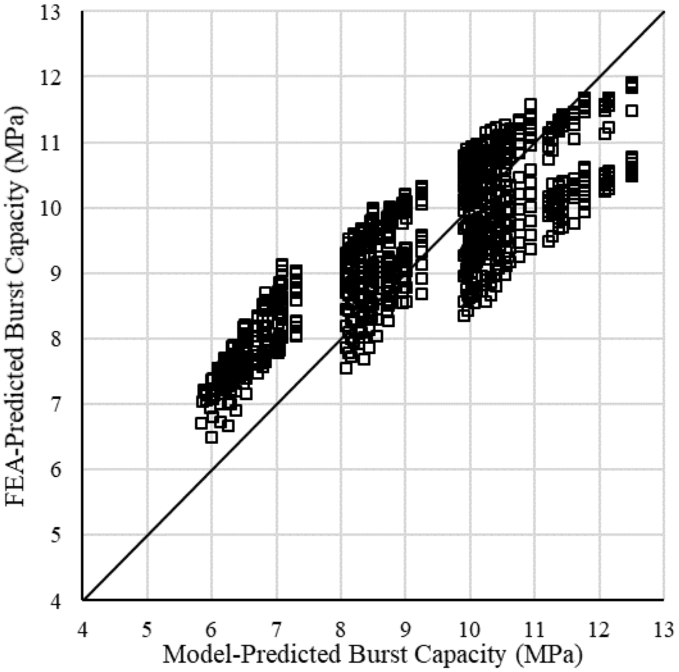

(b) DNV

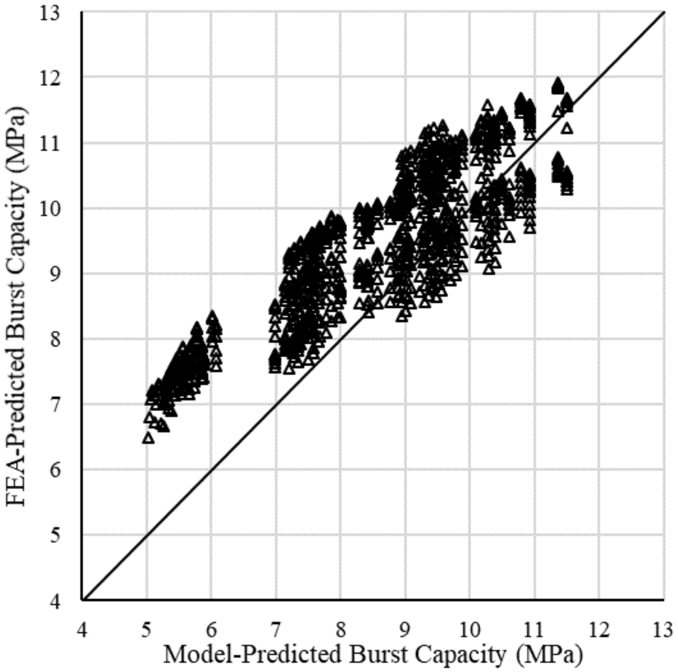

(c) RPA-PLLC

Figure 5.5 Predictive accuracy of the proposed model, DNV, PRA-PLLC for the 954 analysis cases involving combined loads

Table 5.3 Mean and COV of the FEA-to-model predicted burst capacity ratios for 954 FEA analysis cases involving combined loads

	$P_{b-FEA}^{comb}/P_{b}^{comb}$	$P_{b-FEA}^{comb}/P_{DNV}^{comb}$	$P_{b-FEA}^{comb}/P_{RPA}^{comb}$
Mean	1.01	1.05	1.13
COV	3.1%	10.5%	11.4%

The proposed model is further validated by focusing on the correction factor, f_{comb}, for the longitudinal compression. To this end, the values of f_{comb}^{FEA} for the 954 cases involving combined loads are computed by normalizing the burst capacities of these cases by those of the corresponding base cases. Figure 5.6(a) depicts the values of f_{comb}^{FEA} in comparison with the corresponding values of f_{comb} predicted by Eq. (5.13). In addition, the values of correction factors f_{DNV} given by Eq. (5.2) and f_{RPA} given by Eq. (5.5) are also computed and plotted with f_{comb}^{FEA} in Figs. 5.6(b) and 5.6(c), respectively. The mean values and COVs of f_{comb}^{FEA}/f_{comb}, f_{comb}^{FEA}/f_{DNV} and f_{comb}^{FEA}/f_{RPA} are summarized in Table 5.4. Figure 5.6 and Table 5.4 demonstrate that f_{comb} accurately quantifies the effect of the longitudinal compression on the burst capacity as values of f_{comb} are in excellent agreement with the corresponding values of f_{comb}^{FEA}; on the other hand, f_{DNV} and f_{RPA} poorly quantify the effect of the longitudinal compression. In fact, f_{DNV} is less than 1.0 for only 5.4% of the 954 cases and equals 1.0 for the other 94.6% of the cases; f_{RPA} is less than 1.0 for 7.6% of the cases and equals unity for the other 92.4% of the cases. That is, f_{DNV} and f_{RPA} do not at all account for the effect of the longitudinal compression for over 90% of the 954 analysis cases, some of which have f_{comb}^{FEA} values substantially lower than 1.0. This serious deficiency in f_{DNV} and f_{RPA} is somewhat masked by the conservatism in P_{DNV} and P_{RPA} (i.e. burst capacity for internal pressure only) such that P_{DNV}^{comb} and P_{RPA}^{comb} do not markedly over-predict the burst capacity under combined loads as reflected by the results in Table 5.3.

Table 5.4 Mean and COV of the FEA-to-model predicted reduction factor ratios for the 954 validation cases

	f_{comb}^{FEA}/f_{comb}	$f_{comb}^{FEA}/f_{comb}^{DNV}$	$f_{comb}^{FEA}/f_{comb}^{RPA}$

Mean	0.99	0.85	0.85
COV	2.6%	8.6%	8.9%

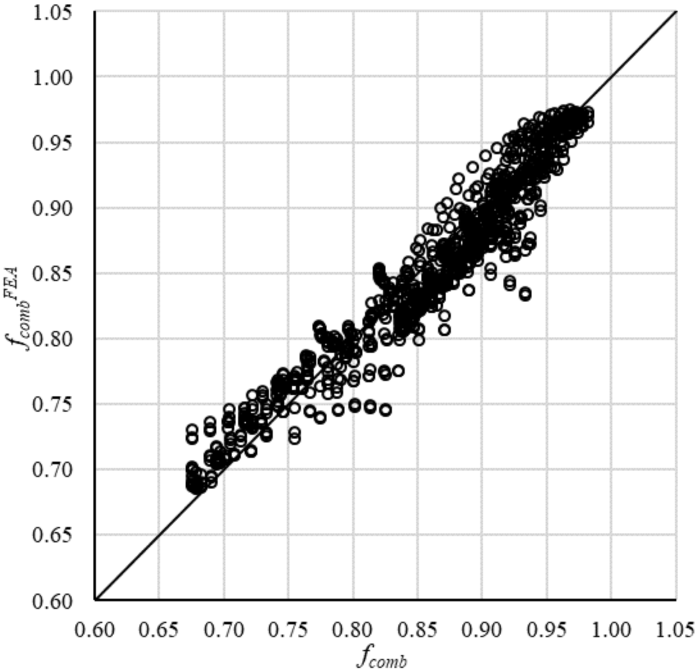

(a) Proposed model

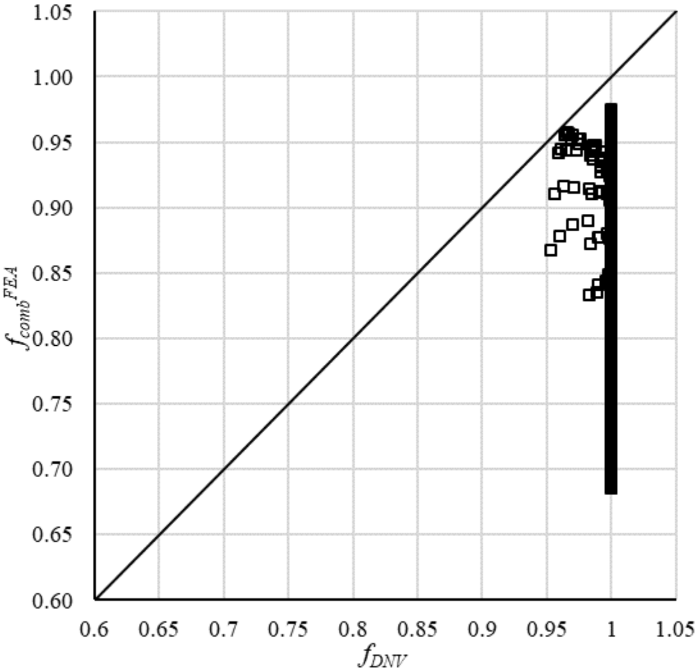

(b) DNV

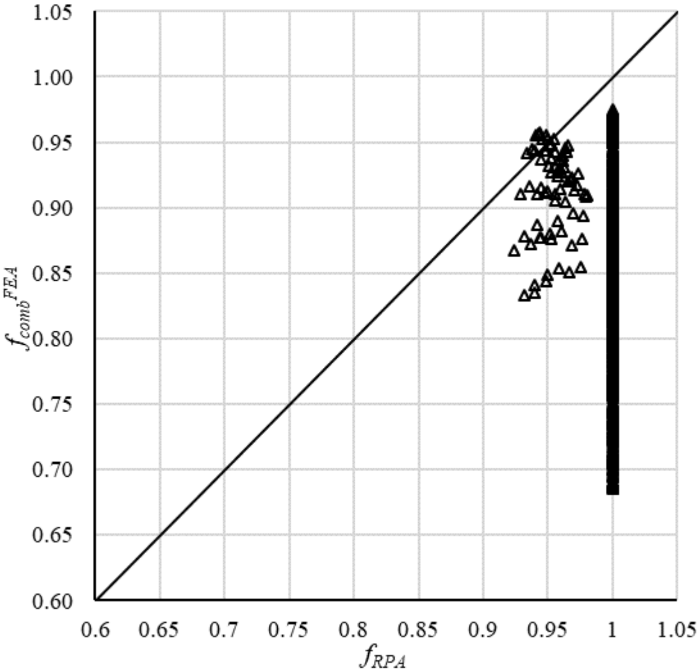

(c) RPA-PLLC

Figure 5.6 Predicted reduction factors of the DNV, PRA-PLLC and proposed models for the 954 analysis cases involving combined loads

5.4.2 Validation with DNV test results

Further validation of the proposed model is carried out by employing the full-scale burst tests reported in (Bjørnøy et al., 2000), which includes a total of 12 test specimens. All the specimens have D = 324 mm and t = 10.3 mm, and are made of the X52 steel with σ_y and σ_u equal to 380 and 514 MPa, respectively, determined from the tensile coupon test. Each specimen contains a rectangular-shaped defect that is spark eroded on the pipe outside surface. The defects are manufactured with a smooth contour surface with all edges made with a small radius. At each end of the test specimen a 50 mm thick end-plate is welded to the pipe. Each of the test specimen is subjected to the internal pressure only or combined loads, the latter involving longitudinal compressive force (F_a) or bending moment (M_b). For the specimens under combined internal pressure and bending moment, the simulated corrosion defect is located on the compressive side of the specimen. The defect geometry and magnitudes of the longitudinal compressive force (F_a) or bending moment (M_b) for the five test specimens included in the present study are summarized in Table 5.5.

Although specimens #1 and #8 are subjected to internal pressure only, they are selected because specimen #1 is the base case for specimens #2 and #3 (i.e. the three specimens are identical except that specimen #1 is subjected to internal pressure only and the latter two subjected to combined loads) and specimen #8 is the base case for specimen #7. Therefore, the impact of the longitudinal compression on the burst capacity can be quantified for specimens #2, #3 and #7 based on test results for specimens #1 and #8. Specimens #4, #5 and #6 are excluded from the present study because they do not have the corresponding base cases such that it is not possible to quantify the impact of the longitudinal compression on the burst capacities of these three specimens. Specimen #9 is excluded because it failed under the increasing axial compression and a constant internal pressure during the test. Finally, specimens #10, #11, and #12 are excluded because each of them contains a single full-circumferential defect to simulate the girth weld corrosion defect, which is out of the scope of the present study.

Table 5.5 Geometry of defects and loading information of the full-scale test specimens reported in (Bjørnøy et al., 2000) and included in the present study

Specimen ID	d (mm)	l (mm)	w (mm)	M_b or F_a	σ_a/σ_y (%)
1	5.15	243	154.5	--	0
2	5.15	243	154.5	129 kNm	-3.0
3	5.15	243	154.5	212 kNm	-35.8
7	5.15	243	30.9	3000 kN	-41.6
8	5.15	243	30.9	--	0

By following the guidelines provided in DNV RP-F101 (2017), the nominal longitudinal compressive stress in the pipe specimens subjected to combined loads is calculated as $\sigma_a = -\left(\frac{F_x}{\pi(D-t)t} + \frac{4M_b}{\pi(D-t)^2 t}\right)$, where F_x is the resultant of the externally applied axial compressive force (F_a) and internal pressure-induced tensile force (F_p) due to the end-cap effect, i.e. $F_x = F_a - F_P$. Note that F_p for a given specimen is computed using the burst pressure of the specimen observed in the test. Table 6 summarizes the observed (P_{test}) and model-predicted burst capacities for the five specimens considered. The results indicate that the variability of the burst capacities predicted by the proposed model is markedly lower than that of the DNV and RPA-PLLC models. The predictions by the DNV model on average agree with the test results. This is not surprising given that the development of the DNV model incorporates the test results. The proposed model is on average slightly non-conservative, as the mean of P_{test}/P_b^{comb} equals 0.94. This can be explained by the fact that the proposed model is developed by considering semi-ellipsoidal-shaped corrosion defects, whereas the corrosion defects on the test specimens are rectangular-shaped.

Since specimen #1 is the base case for specimens #2 and #3, the reduction in the burst capacity due to longitudinal compression is quantified for specimens #2 and #3 by calculating $P_{test,2}/P_{test,1}$ and $P_{test,3}/P_{test,1}$. By the same consideration, the reduction in the burst capacity due to longitudinal compression for specimen #7 is quantified by calculating $P_{test,7}/P_{test,8}$. The above-indicated reduction factors are then compared in Table 5.7 with corresponding values of f_{comb}, f_{DNV} and f_{RPA} computed using Eqs. (5.13), (5.2) and (5.5), respectively. Similar to Table 5.4, the results in Table 5.7 again clearly demonstrate that f_{DNV} and f_{RPA} are unable to capture the impact of longitudinal compression on the burst capacity, whereas the proposed longitudinal compression factor f_{comb} provides a markedly improved quantification of the longitudinal compression effect. It is worth noting that the values of σ_a/σ_y for specimens #3 and #7 are outside of the suggested applicability range (i.e. $-0.3 \leq \sigma_a/\sigma_y \leq 0$) for f_{comb}; however, the values of f_{comb} for the two specimens are still in good agreement with the corresponding reduction factors obtained from the test results. This suggests that the proposed burst capacity model can potentially be applicable for σ_a/σ_y equal to about -0.4.

Table 5.6 Observed and predicted burst capacities for the DNV full-scale test specimens

Specimen ID	P_{test} (MPa)	P_{DNV}^{comb}[1] (MPa)	P_{RPA}^{comb}[1] (MPa)	P_b^{comb}[1] (MPa)	P_{test}/P_b^{comb}	P_{test}/P_{DNV}^{comb}	P_{test}/P_{RPA}^{comb}
1	23.20	21.00	18.82	24.41	0.95	1.10	1.23
2	21.90	21.00	18.82	24.04	0.91	1.04	1.16
3	19.50	21.00	18.82	20.04	0.97	0.93	1.04
7	18.60	21.00	18.17	19.89	0.94	0.89	1.02
8	22.00	21.00	18.82	23.48	0.94	1.05	1.17
		Mean			0.94	1.00	1.12
		COV			2.2%	8.1%	7.2%

1. The burst capacities of specimens #1 and #8 are predicted using the burst capacity model for internal pressure only.

Table 5.7 Observed and predicted reduction factors due to longitudinal compression for the DNV full-scale test specimens involving combined loads

Specimen ID	Reduction factor due to compression based on test results	f_{comb}	f_{DNV}	f_{RPA}
2	0.94	0.98	1	1
3	0.84	0.82	1	1
7	0.85	0.85	1	0.97

5.5 Conclusion

In this chapter, a semi-empirical burst capacity model is proposed for corroded oil and gas pipelines subjected to the combined internal pressure and longitudinal compression. The proposed model is expressed as the burst capacity for corroded pipelines under internal pressure only multiplied by a correction factor to account for the adverse impact of the longitudinal compression on the burst capacity. The burst capacity model for the internal pressure only, which has been developed in a previous study, follows the well-known NG-18 format and takes into account the depth, length and width of the corrosion defect. The correction factor for the longitudinal compression is considered as a function of the defect depth, length and width as well as the magnitude of the longitudinal compressive stress, and developed based on multivariate nonlinear regression analyses of results of 477 parametric FEA cases. The accuracy of the proposed model is validated by 1431 additional parametric FEA cases and full-scale burst tests of corroded pipe specimens reported in the literature. In particular, the proposed model is shown to be markedly more accurate than the DNV and RPA-PLLC models in terms of quantifying the influence of longitudinal compression on the bust capacity of corroded pipelines. The DNV and RPA-PLLC models are found to be inadequate to quantify the longitudinal compression effect on the burst capacity based. The proposed model is a viable practical tool to carry out fitness-for-service assessments of corroded pipelines subjected to combined internal pressure and longitudinal compression.

References

Al-Owaisi, S., Becker, A. A., Sun, W., Al-Shabibi, A., Al-Maharbi, M., Pervez, T., & Al-Salmi, H., 2018. An experimental investigation of the effect of defect shape and orientation on the burst pressure of pressurised pipes. *Engineering Failure Analysis, 93,* 200-213.

Arumugam, T., Karuppanan, S., & Ovinis, M., 2020. Finite element analyses of corroded pipeline with single defect subjected to internal pressure and axial compressive stress. *Marine Structures, 72*, 102746.

ASME, 1991. “Manual for determining the remaining strength of corroded pipelines- a supplement to ASME B31 code for pressure piping”, The American Society of Mechanical Engineers, New York.

Benjamin, A. C., 2008. Prediction of the failure pressure of corroded pipelines subjected to a longitudinal compressive force superimposed to the pressure loading. In *International Pipeline Conference* (Vol. 48586, pp. 179-189).

Bjørnøy, O. H., Sigurdsson, G., & Cramer, E., 2000, January. Residual strength of corroded pipelines, DNV test results. In *The Tenth International Offshore and Polar Engineering Conference*. International Society of Offshore and Polar Engineers.

Cai, J., Jiang, X., Lodewijks, G., Pei, Z., & Wu, W., 2018. Residual ultimate strength of damaged seamless metallic pipelines with metal loss. *Marine Structures, 58*, 242-253.

Cai, J., Jiang, X., Lodewijks, G., Pei, Z., & Zhu, L., 2019. Experimental investigation of residual ultimate strength of damaged metallic pipelines. *Journal of Offshore Mechanics and Arctic Engineering, 141*(1).

Chen, Y., Zhang, H., Zhang, J., Liu, X., Li, X., & Zhou, J., 2014. Residual bending capacity for pipelines with corrosion defects. *Journal of Loss Prevention in the Process Industries, 32*, 70-77.

Chouchaoui, B., 1995. Evaluating the remaining strength of corroded pipelines, PhD thesis, University of Waterloo.

Canadian Standard Association, (CSA), 2019. Oil and gas pipeline systems. CSA standard Z662-19. *Mississauga, Ontario, Canada*.

Cunha, S. B., Pacheco, M., & da Silva, A. B., 2016. Numerical Simulations of Burst of Corroded Pipes With Thermally Induced Compressive Axial Strain. *In International Pipeline Conference* (Vol. 50251, p. V001T03A002). American Society of Mechanical Engineers.

Dassault Systèmes, D. S., 2016. Abaqus analysis user's guide. Technical Report Abaqus 2016 Documentation, Simulia Corp.

Det Norske Veritas (DNV), 2017. “Recommended practice DNV-RP-F101, corroded pipelines”, Hovic, Norway.

Gao, J., Peng, Z., Li, X., Zhou, J., & Zhou, W., 2018. Bending Capacity of Corroded Pipeline Subjected to Internal Pressure and Axial Loadings. In *International Conference on Offshore Mechanics and Arctic Engineering* (Vol. 51227, p. V003T02A084). American Society of Mechanical Engineers.

Karimian, S. A., 2006. Response of buried steel pipelines subjected to longitudinal and transverse ground movement (Doctoral dissertation, University of British Columbia).

Kiefner, J. F., 1969. Fracture initiation. In *Paper G, Proceedings of the 4th Symposium on Line Pipe Research, Pipeline Research Committee of the American Gas Association, Dallas, Texas, USA, AGA Catalogue* (No. L30075, pp. G1-G36).

Kiefner, J. and Vieth, P., 1989. “A modified criterion for evaluating the remaining strength of corroded pipe (No. PR-3-805). Battelle Memorial Institute, OH (USA).

Kiefner, J. and Vieth, P., 1990. “PC program speeds new criterion for evaluating corroded pipe”, Oil and Gas Journal, August 20, 1990. pp. 91-93.

Liu, J., Chauhan, V., Ng, P., Wheat, S., & Hughes, C., 2009. Remaining strength of corroded pipe under secondary (biaxial) loading (Report No. R9068). GL Industrial Services UK Ltd.

MATLAB. 2018. Natick, Massachusetts: The MathWorks Inc.

Meidani, M., Meguid, M. A., & Chouinard, L. E., 2017. Evaluation of soil–pipe interaction under relative axial ground movement. *Journal of Pipeline Systems Engineering and Practice, 8*(4), 04017009.

Meidani, M., Meguid, M. A., & Chouinard, L. E., 2018. Estimating earth loads on buried pipes under axial loading condition: insights from 3D discrete element analysis. *International Journal of Geo-Engineering, 9*(1), 5.

Mohd, M. H., Lee, B. J., Cui, Y., & Paik, J. K., 2015. Residual strength of corroded subsea pipelines subject to combined internal pressure and bending moment. *Ships and offshore Structures*, *10*(5), 554-564.

Mondal B. C., 2018. Remaining Strength Assessment of Deteriorating Energy Pipelines. PhD thesis, Faculty of Engineering and Applied Science, Memorial University of Newfoundland, St. John's, NL, Canada.

Mondal, B. C., & Dhar, A. S., 2019. Burst pressure of corroded pipelines considering combined axial forces and bending moments. *Engineering Structures*, *186*, 43-51.

Ritchie, D., & Last, S., 1995. Burst criteria of corroded pipelines-defect acceptance criteria. In *Proceedings of the EPRG/PRC 10th biennial joint technical meeting on line pipe research*. Cambridge, UK, Paper 32.

Shim, D. J., Kim, Y. J., & Kim, Y. J., 2005. Reference stress based approach to predict failure strength of pipes with local wall thinning under combined loading. *J. Pressure Vessel Technol., 127*(1), 76-83.

Smith, M. Q., & Waldhart, C. J., 2000. Combined loading tests of large diameter corroded pipelines. In *2000 3rd International Pipeline Conference*. American Society of Mechanical Engineers Digital Collection.

Stephens, D. R., Bubenik, T. A., & Francini, R. B., 1995. Residual strength of pipeline corrosion defects under combined pressure and axial loads. Final report (No. AGA-96005964). Battelle, Columbus, OH (United States).

Taylor, N., Clubb, G., & Matheson, I., 2015. The Effect of Bending and Axial Compression on Pipeline Burst Capacity. In *SPE Offshore Europe Conference and Exhibition*. Society of Petroleum Engineers.

Wijewickreme, D., Karimian, H., & Honegger, D., 2009. Response of buried steel pipelines subjected to relative axial soil movement. *Canadian Geotechnical Journal, 46*(7), 735-752.

Yu, W., Vargas, P. M., & Karr, D. G., 2012. Bending capacity analyses of corroded pipeline. *Journal of offshore mechanics and Arctic engineering, 134*(2).

Zhang, S. & Zhou, W., 2020a, Development of a burst capacity model for corroded pipelines under internal pressure and axial compression using artificial neural network, Proceedings of the 2020 13th International Pipeline Conference,September 28 – October 2, 2020, Calgary, Alberta, Canada, IPC2020-9690

Zhang, S., & Zhou, W., 2020b. Assessment of effects of idealized defect shape and width on the burst capacity of corroded pipelines. *Thin-Walled Structures*, *154*, 106806.

Zhang, S. & Zhou, W., 2021. Development of a burst capacity model for corroded pipelines considering corrosion defect width and a revised Folias factor equation. *Journal of Natural Gas Science and Engineering*, accepted.

Zhou, H., Wang, Y. Y., Stephens, M., Bergman, J., & Nanney, S., 2018. Burst Pressure of Pipelines With Corrosion Anomalies Under High Longitudinal Strains. In *International Pipeline Conference* (Vol. 51876, p. V002T06A008). American Society of Mechanical Engineers.

Zhu, X. K., & Leis, B. N., 2005. Influence of yield-to-tensile strength ratio on failure assessment of corroded pipelines. *Journal of Pressure Vessel Technology*, 127, pp. 436-442.

6 Assessment of the Interaction of Corrosion Defects on Steel Pipelines under Combined Internal Pressure and Longitudinal Compression Using Finite Element Analysis

6.1 Introduction

Corrosion defects threaten the structural integrity of oil and gas pipelines as they cause thinning of the pipe wall and therefore reduce the pressure containment capacity, i.e. burst capacity, of the pipeline. Multiple corrosion defects often exist in close proximity on a given pipeline. This can lead to the so-called interaction effect; that is, the burst capacity of the pipeline containing multiple closely-spaced defects is lower than those of the same pipeline containing each of the defects individually. Extensive experimental and numerical studies have been reported in the literature to investigate the interaction of two closely-spaced corrosion defects on pipelines subjected to the internal pressure only (Benjamin et al., 2005, 2006; Silva et al, 2007; Li et al., 2016; Xu et al., 2017; Al-Owaisi et al., 2018; Sun and Cheng, 2018). These studies indicate that the interaction between two closely-spaced defects oriented in the pipe circumferential direction is weak, whereas the interaction between closely-spaced defects oriented in the pipe longitudinal direction is marked. As the separation distance between longitudinally-oriented defects increases, the interaction between defects, as intuitively expected, decreases. Simple-to-use (generally conservative) defect interaction rules have also been suggested in various standards and recommended practice to facilitate the integrity assessment of corroded pipelines in practice (Kiefner and Vieth, 1990; ASME, 2017; DNV, 2017; CSA, 2019). These interaction rules are generally expressed in terms of the circumferential and longitudinal separation distances between two neighbouring defects. For example, the widely used $3t \times 3t$ rule as recommended in (ASME, 2017) states that two defects interact with each other if their circumferential and longitudinal separation distances (S_C and S_L as depicted in Fig. 6.1) are respectively less than or equal to $3t$, where t denotes the pipe wall thickness. For a group of three or more closely-spaced defects, the interaction rule is applied successively to different sets of two neighbouring defects until all the interacting defects are identified.

In-service pipelines are often subjected to longitudinal forces or bending moments resulting from, for example, ground movement or formation of free spans (Karimian, 2006;

Wijewickreme et al., 2009; Meidani et al., 2017, 2018), in addition to internal pressures. As reported in (Chouchaoui, 1995; Bjørnøy et al., 2000; Smith and Waldhart, 2000; Liu et al., 2009; Taylor et al., 2015; Mondal and Dhar, 2019), the burst capacity of a corroded pipeline under the longitudinal compression and internal pressure can be markedly lower than that of the pipeline under the internal pressure only. Note that the longitudinal compression may result from a compressive force or bending moment (with the corrosion defect located on the compression side of the bending). It is therefore important to investigate the interaction effects between closely-spaced corrosion defects under longitudinal compression and internal pressure (referred to, for brevity, as combined loads in the following). Kuppusamy et al. (2016) studied the interaction effect of corrosion defects on pipelines under combined loads; they however focused on the interaction effect on the buckling strength as opposed to burst capacity of corroded pipelines. Arumugam et al. (2020) carried out finite element analyses (FEA) to investigate the interaction effect of corrosion defects on the burst capacity of pipelines under combined loads by comparing the burst capacity of two longitudinally-aligned defects with that of three longitudinally-aligned defects. Since the interaction effect is typically quantified by using the burst capacity of a single defect as the benchmark, the study in (Arumugam et al., 2020) did not offer a clear understanding of the interaction effect under combined loads. Furthermore, the interaction of circumferentially-aligned defects under combined loads is not considered in (Arumugam et al., 2020). Bruère et al. (2019) conducted FEA to investigate the burst capacity of corroded pipelines under combined internal pressure and thermal expansion-induced axial compressive stress. The analysis in (Bruère et al., 2019) is limited to two specific defect configurations, consisting of two and three defects respectively, and the interaction effect is not discussed or quantified. Furthermore, it is worth noting that the thermal expansion-induced axial compression is a displacement-controlled loading condition, which has been reported (Taylor et al., 2015; Cunha et al., 2016) to have a negligible effect on the burst capacity of corroded pipelines.

In this study, parametric three-dimensional (3D) elastoplastic FEA is carried out to investigate the interaction effects of closely-spaced corrosion defects on pipelines under combined loads. To have a clear, fundamental understanding of the interaction effect under combined loads without analyzing an onerously large number of parametric cases, we focus on cases involving two identical, longitudinally- or circumferentially-aligned defects in the present study. The axial compression on the corroded pipeline is applied as a load-controlled (as opposed to displacement-controlled) process. Full-scale burst tests of corroded pipe specimens reported in the literature are used to validate the finite element models and failure criterion employed in the present study. Semi-ellipsoidal-shaped corrosion defects with various depths (in the through wall thickness direction), lengths (in the pipe longitudinal direction), widths (in the circumferential direction), S_C and S_L are considered in FEA. The analysis results shed light on the similarity and difference between the defect interaction effects for pipelines subjected to the internal pressure only and combined loads, respectively. Based on the analysis results, the underlying mechanisms for the interaction effect are explained. The adequacy of the commonly used defect interaction rules for the combined loading condition is also examined. The rest of the chapter is organized as follows. Section 6.2 presents details of the finite element model and model validation; Section 6.3 presents the parametric FEA cases and analysis results in terms of the interaction between circumferentially- and longitudinally-aligned corrosion defects, as well as the underlying mechanisms for the interaction, and Section 6.4 discusses the adequacy of the existing interaction rules for combined loads, followed by concluding remarks in Section 6.5.

6.2 Finite Element Model

6.2.1 General

The 3D elasto-plastic FEA has proven to be an effective tool to evaluate the burst capacity of corroded pipelines (Chouchaoui, 1995). The commercial FEA code ABAQUS (Dassault Systèmes, 2016) is employed in this study, and the 8-node solid element (C3D8) with full integration is selected. The finite-strain configuration is employed to capture the geometric non-linearity at internal pressure levels close to burst. The von Mises yield criterion, associated flow rule as well as isotropic hardening rule are adopted in the numerical simulation.

6.2.2 Material properties and failure criterion

The true stress–strain relationship of typical pipe steels can be well represented by a power-law model (Zhu and Leis, 2004; Wang and Zhang, 2011) in the plastic domain as given by Eq. (6.1).

$$\begin{cases} \sigma = E\varepsilon & \sigma < \sigma_y \\ \sigma = K\varepsilon^n & \sigma \geq \sigma_y \end{cases} \tag{6.1}$$

where σ and ε denote the true stress and true strain in uniaxial tensile test, respectively; E is Young's modulus; σ_y is the yield strength, corresponding to a 0.2% offset strain or 0.5% total strain; K and n are coefficients of the power-law stress-strain relationship in the plastic domain, and n is also known as the strain hardening exponent. If tensile coupon test results are available, the values of K and n in Eq. (6.1) can be obtained from curve fitting of the test data. If only the yield strength (σ_y) and ultimate tensile strength (UTS), denoted by σ_u, are known while coupon test results are unavailable, the following empirical equation can be used to estimate the value of n (Zhu and Leis, 2005):

$$n = 0.239\left(\frac{1}{\sigma_y/\sigma_u} - 1\right)^{0.596} \tag{6.2}$$

Given the value of n, K can be estimated by using the Considere's criterion (Dowling, 2007):

$$K = \frac{e^n}{n^n}\sigma_u \tag{6.3}$$

where e is the base of the natural logarithm.

The ultimate tensile strength (UTS)-based failure criterion, which has been shown to adequately predict the burst capacity of corroded pipelines (Cronin, 2000; Bao et al., 2018; Zhang and Zhou, 2020), is adopted in this study. According to this criterion, the burst capacity of a corroded pipe is obtained once the maximum nodal von Mises stress anywhere within the defected region reaches the true stress corresponding to UTS.

6.2.3 Validation of FEA

The finite element model and UTS-based failure criterion should ideally be validated by full-scale burst tests of pipe specimens containing closely-spaced defects and subjected to combined loads. There is however a lack of such test data in the literature. As a result, six full-scale burst tests involving pipe specimens containing closely-spaced defects under internal pressure only (Benjamin et al., 2005; Al-Owaisi et al., 2018), and six pipe specimens containing single defects under combined loads (Bjørnøy et al., 2000) are employed in the validation. The defects in all 12 specimens are artificially induced: three specimens containing semi-ellipsoidal-shaped defects and nine specimens containing rectangular-shaped defects. Three of the six specimens selected from (Benjamin et al., 2005; Al-Owaisi et al., 2018) contain circumferentially-aligned defects, whereas the other three specimens contain longitudinally-aligned defects. Note that a total of 12 burst test specimens are reported in (Bjørnøy et al., 2000). Specimens #1 and #8 are excluded from the present study because they are subjected to internal pressure only. Specimens #10, 11, and 12 are also excluded because each of them contains a single full-circumferential defect located on the pipe girth weld. Finally, specimen #9 is excluded because it failed under the increasing axial compression and a constant internal pressure.

Table 6.1 summarizes the basic geometric and material properties of the 12 pipe specimens, including the outside diameter (D), wall thickness (t), steel grade, σ_y, σ_u, E and n (σ_y, σ_u, E and n are obtained from tensile coupon tests). Table 6.2 summarizes the geometry of defects on the 12 specimens, including the maximum defect depth (d), defect length (l) and width (w), values of S_C and S_L for the specimens containing two defects, and magnitudes of the longitudinal compressive force (F_a) or bending moment (M_b) for the specimens subjected to combined loads. The burst pressures observed in the tests (P_{test}) as well as those predicted by FEA (P_{FEA}) are also included in Table 6.2. For the six specimens subjected to combined loads, the loading sequences employed in the tests (see (Bjørnøy et al., 2000) for details) are replicated in FEA. In general, the last loading step for each specimen involves increasing the internal pressure until burst while holding the compressive force/bending moment unchanged as the corresponding value indicated in Table 6.2. For the six specimens under internal pressure only, one end of the model is restricted in the longitudinal direction and corresponding axial stress is simultaneously applied at the freed end of the model while the internal pressure is applied, as the pipe specimens are end-capped during the burst tests. For the six specimens subjected to combined loads, reference points are created for each end of the model with the end-section constrained to the reference point by "coupling" under the Interaction-Module in ABAQUS. The longitudinal compressive force or bending moment is then applied to the reference point. Note that the six specimens are end-capped during the test, and the end cap is included in the finite element model. Figure 6.1 depicts finite element models for three representative specimens that contain, respectively, a single defect, circumferentially-aligned defects, and longitudinally-aligned defects. The total numbers of elements (E-#) in the representative models are also indicated in Fig. 6.1. Four layers of elements are used through the ligament of each defect area to ensure the high stress gradient along the radial direction of the defect area to be accurately captured. The mesh in the FEA model is transitioned from a high density in the defected region to a low density in the defect-free region in the longitudinal, circumferential and radius directions. The mesh densities for the models are selected following mesh convergence studies.

The fact that the mean and coefficient of variation (COV) of P_{test}/P_{FEA} are 1.00 and 3.4%, respectively, as presented in Table 6.2 indicates that the FEA-predicted and observed burst capacities are in excellent agreement. This provides a strong validation of the finite element model and UTS-based burst criterion employed in the analysis.

Table 6.1 Geometric and material properties of burst test specimens reported in the literature

Source	Steel grade	E (GPa)	σ_y (MPa)	σ_u (MPa)	n	D (mm)	t (mm)
6.A	X52	200	380	514	0.18	324	10.3
6.B	X80	200	534.1	661.4	0.08	458.8	8.1
6.C	X52	182	372	497.7	0.20	508	9.7

Note: Source 6.A, 6.B and 6.C refer to Ref (Bjørnøy et al., 2000), Ref (Benjamin et al., 2005) and Ref (Al-Owaisi, 2018), respectively.

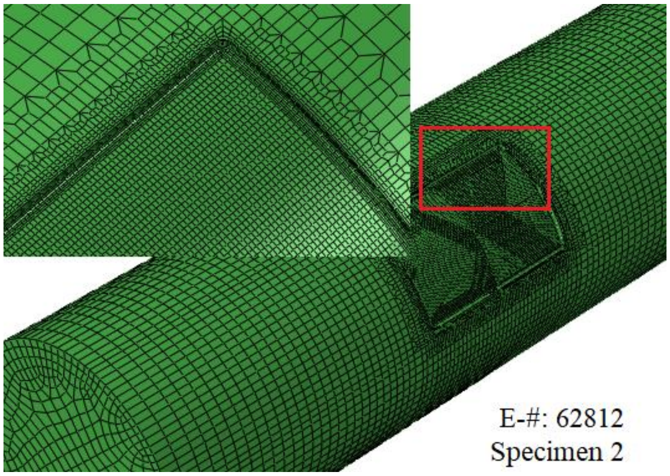

(a) Specimen with a single defect

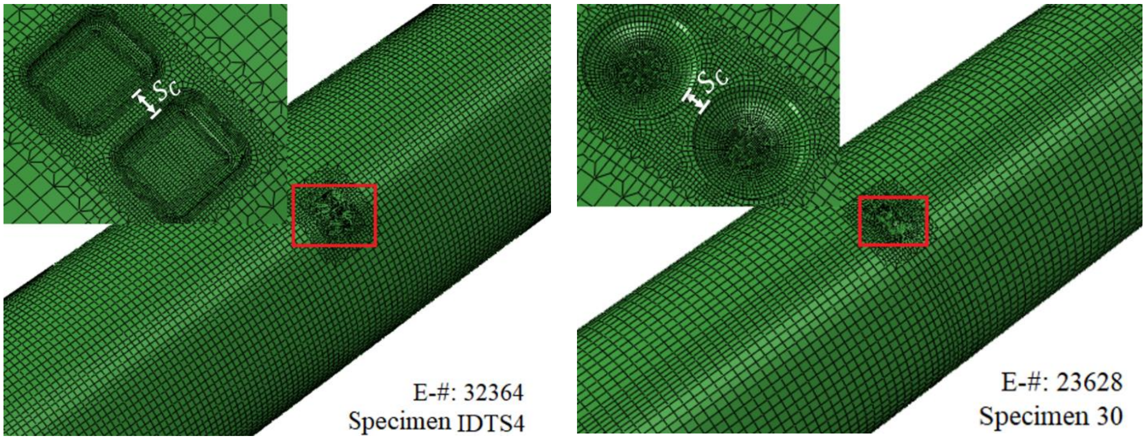

(b) Specimens with circumferentially-aligned defects

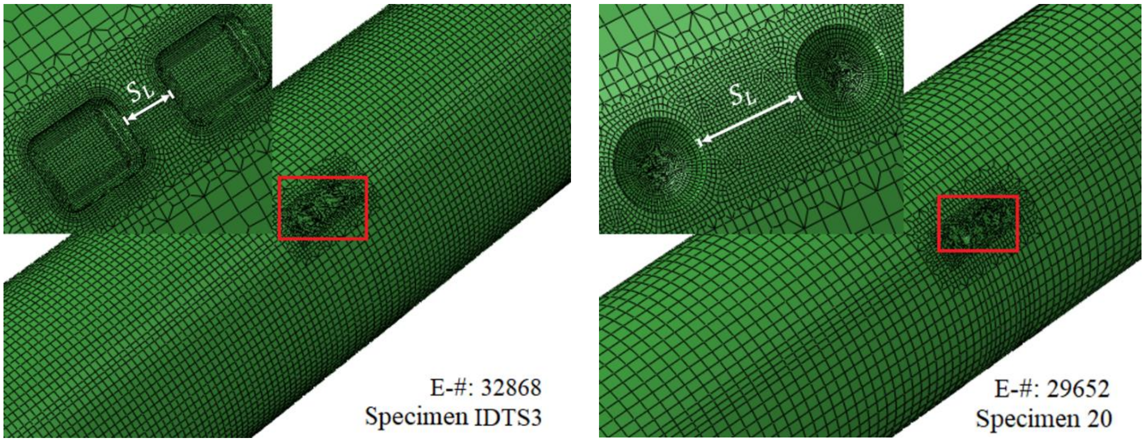

(c) Specimens with longitudinally-aligned defects

Figure 6.1 FEA meshes for representative full-scale pipe specimens in Table 6.2

Table 6.2 Geometry of defects, as well as observed and FEA-predicted burst capacities for the pipe specimens

Source	Specimen ID	d (mm)	l (mm)	w (mm)	S_C (mm)	S_L (mm)	M_b or F_a	P_{test} (MPa)	P_{FEA} (MPa)	P_{test}/P_{FEA}
6.A	2	5.15	243	154.5	--	--	129 kNm	21.9	21.62	1.01
	3	5.15	243	154.5	--	--	212 kNm	19.5	20.26	0.96
	4	3.09	121.5	30.9	--	--	73 kNm	29	29.55	0.98
	5	3.09	121.5	30.9	--	--	2563 kN	28.6	27.26	1.05
	6	3.09	121.5	30.9	--	--	2943 kN	28.7	26.99	1.06
	7	5.15	243	30.9	--	--	3000 kN	18.6	19.66	0.95
6.B	IDTS4	5.62	39.6	32.0	9.9	--	--	21.14	21.57	0.98
6.C	29	4.9	35	35	9.75	--	--	19.55	20.23	0.97
	30	4.85	35.5	33.7	4.8	--	--	20.68	20.06	1.03
6.B	IDTS3	5.32	39.6	31.9	--	20.5	--	20.31	19.80	1.03
6.C	20	4.85	35.5	35.5	--	38.7	--	19.59	19.39	1.01
	21	4.85	35.5	33.6	--	48.7	--	19.65	19.48	1.01
Mean										1.00
COV										3.4%

Note: Specimens 20, 21 and 30 contain semi-ellipsoidal-shaped defects, and the other specimens contain rectangular-shaped defects. Source 6.A, 6.B and 6.C refer to Ref (Bjørnøy et al., 2000), Ref (Benjamin et al., 2005) and Ref (Al-Owaisi, 2018), respectively.

6.3 Defect Interaction Effects under Combined Loads

6.3.1 Parametric FEA cases

The validated finite element model and failure criterion are used to carry out extensive parametric analyses to investigate the defect interaction effects under combined loads. The attributes of the pipeline considered in the analysis, which are representative of those of oil and gas transmission pipelines, are summarized in Table 6.3, where MOP denotes the maximum operating pressure. For a given analysis case, three loading scenarios are considered: the base case in which the internal pressure is the only load, and two other scenarios involving combined loads with different magnitudes of the longitudinal compression. In the base case, the pipe model is assumed to be longitudinally fully-restrained and no additional axial stress is involved other than that induced by internal pressure due to the boundary condition. For the two scenarios involving combined loads, the longitudinal compression is introduced by applying a uniform compressive stress (σ_a) on the corrosion-free pipe cross section at the free end of the pipe model, while keeping the other end longitudinally restrained. The magnitude of the externally-applied longitudinal compression is expressed as the ratio of the corresponding compressive stress to σ_y, i.e. σ_a/σ_y = -0.15 and σ_a/σ_y = -0.3 for the two scenarios respectively (the negative sign indicates compression).

The pipe model has a fixed length of 3 m to minimize the effects of the end condition and slenderness. The corrosion defects on the pipe model are idealized to be semi-ellipsoidal-shaped. Although naturally-occurring corrosion defects are irregular-shaped, it is common practice to idealize corrosion defects to be rectangular- or semi-ellipsoidal-shaped in the literature, e.g. (Benjamin et al., 2005, 2006; Silva et al, 2007; Li et al., 2016; Xu et al., 2017; Al-Owaisi et al., 2018; Sun and Cheng, 2018), to facilitate the finite element analysis of the burst capacity of corroded pipelines. The adequacy of the semi-ellipsoidal idealization of naturally-occurring corrosion defects has been reported in a recent study (Zhang and Zhou, 2020), which compares the FEA-predicted burst capacities of idealized corrosion defects with experimentally-observed burst capacities of pipe specimens containing naturally-occurring corrosion defects. Furthermore, the semi-ellipsoidal idealization is reported (Zhang and Zhou, 2020) to be a more accurate approximation of naturally-occurring corrosion defects than the rectangular idealization. To shed light on the interaction effect and its underlying mechanism for corrosion defects under combined loads, the present study is focused on two defects that are aligned circumferentially or longitudinally on the external surface of the pipe model with different spacing. The values of the normalized defect depth (d/t), length ($l^2/(Dt)$), width (w/l) and spacing between the defects ($S_C/\sqrt{Dt}$ and $S_L/\sqrt{Dt}$) for the parametric FEA cases are summarized in Table 6.4. In total, there are 360 analysis cases with circumferentially-aligned defects, 480 cases with longitudinally-aligned defects, and 60 cases with a single defect. Two representative finite element models containing circumferentially (longitudinally) -aligned defects are depicted in Fig. 6.2(a) (Fig. 6.2(b)). To improve the computational efficiency, the FEA is conducted with a half model based on the longitudinal symmetric plane. The corresponding symmetric boundary condition is applied on the longitudinal plane.

Table 6.3 Pipe attributes considered in parametric FEA

Steel grade	D (mm)	t (mm)	E (GPa)	σ_y (MPa)	σ_u (MPa)	MOP (MPa)
X52	406	6.0	200	359	455	5.3

Table 6.4 Defect geometry and spacing considered in parametric FEA

d/t	$l^2/(Dt)$	w/l	Circumferentially aligned defects	Longitudinally aligned defects
			$S_C/\sqrt{Dt}$	$S_L/\sqrt{Dt}$
0.3, 0.6	2, 20	0.5, 1, 1.5	0.5, 1, 2, 3, 4, 5	0.5, 1, 2, 3, 4, 5, 7, 10
	10	0.5, 1.5	0.5, 1, 2, 3, 4, 5	0.5, 1, 2, 3, 4, 5, 7, 10
0.45	2, 20	0.5, 1.5	0.5, 1, 2, 3, 4, 5	0.5, 1, 2, 3, 4, 5, 7, 10

To obtain the burst capacity of a pipe model under combined loads (i.e. σ_a/σ_y = -0.15 or -0.3), a three-step loading sequence is employed in FEA as follows.

1. Increase the internal pressure from zero to MOP under the longitudinally fully-restrained boundary condition.

2. Deactivate the longitudinal restraint of one end of the pipe model and increase the longitudinal compressive stress to its target value (i.e. σ_a/σ_y = -0.15 or -0.30) while holding the internal pressure constant at MOP.

3. Increase the internal pressure from MOP until burst while holding σ_a constant at the level achieved at the end of step 2 and keeping the boundary conditions unchanged.

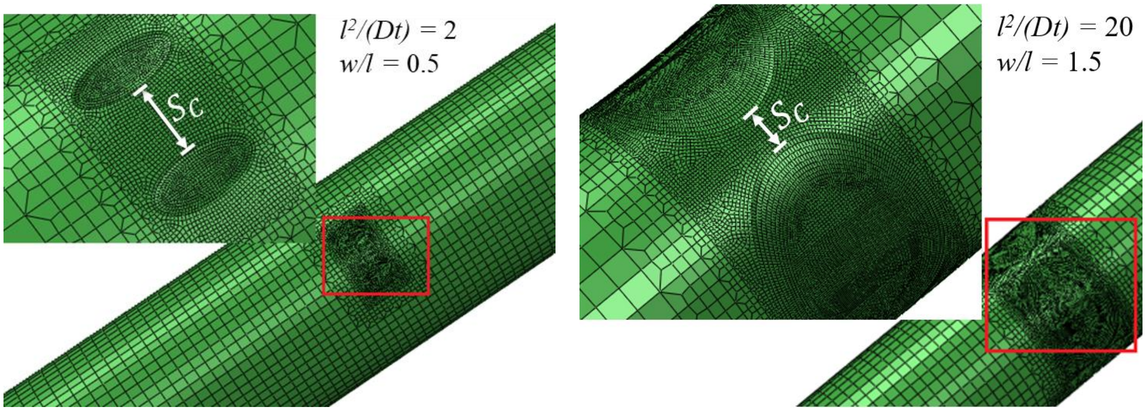

(a) Circumferentially-aligned defects

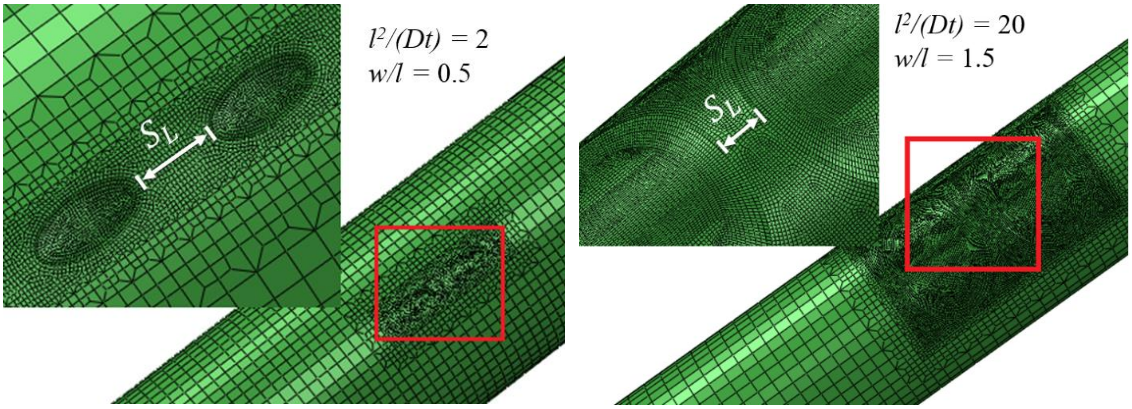

(b) Longitudinally-aligned defects

Figure 6.2 Representative finite element models containing circumferentially- and longitudinally-aligned defects

6.3.2 Interaction effects of circumferentially-aligned defects

To clearly quantify the interaction effects, the predicted burst capacity of an analysis case containing two defects (P_b) is normalized by the predicted burst capacity of the corresponding single-defect case (P_{bs}) under the same loading condition (i.e. internal pressure only or combined loads with σ_a/σ_y = -0.15 or -0.30). Figure 6.3 depicts P_b/P_{bs} for representative cases resulting from eight different combinations of d/t = 0.3 and 0.6, $l^2/(Dt)$= 2 and 20, and w/l= 0.5 and 1.5. The vertical lines in the figure correspond to a number of practical interaction rules and are discussed in detail in Section 6.4. The values of P_b/P_{bs} for the other cases, which show a similar trend as in Fig. 6.3, are depicted in Fig. C.1 of Appendix C. Figure 6.3 indicates that P_b/P_{bs} approximately equals 1.0 at $S_C/\sqrt{Dt}$ = 5; this suggests that the interaction between circumferentially aligned defects is negligible for $S_C/\sqrt{Dt} \geq 5$.

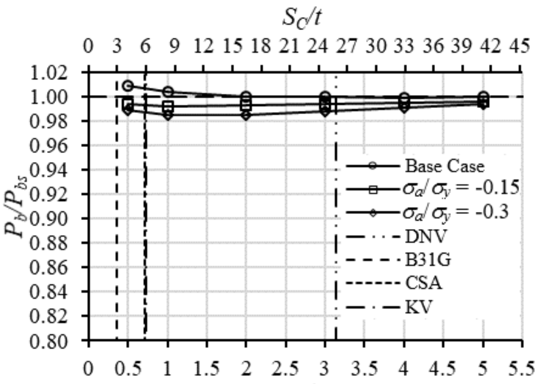

(a) *d/t*=0.3, $l^2/(Dt)$=2, *w/l*=0.5

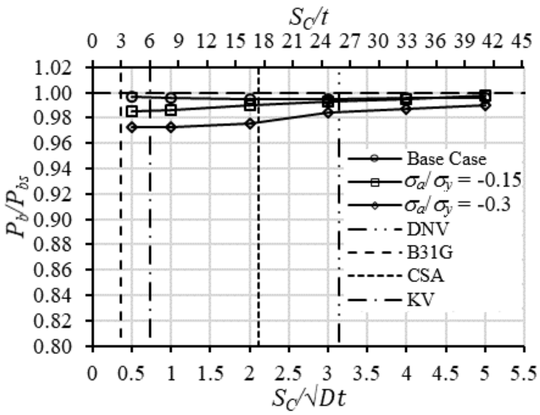

(b) *d/t*=0.3, $l^2/(Dt)$=2, *w/l*=1.5

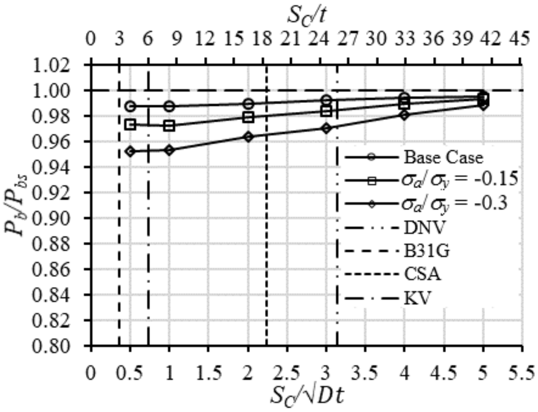

(c) *d/t*=0.3, $l^2/(Dt)$=20, *w/l*=0.5

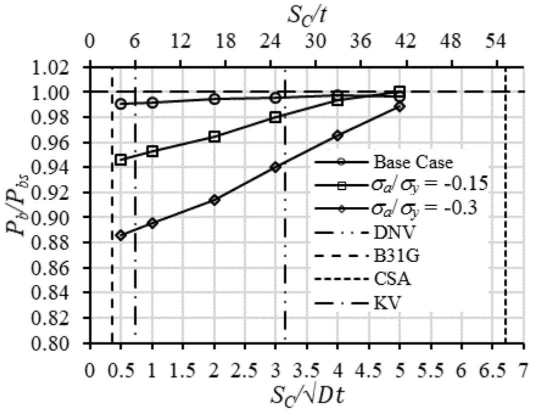

(d) *d/t*=0.3, $l^2/(Dt)$=20, *w/l*=1.5

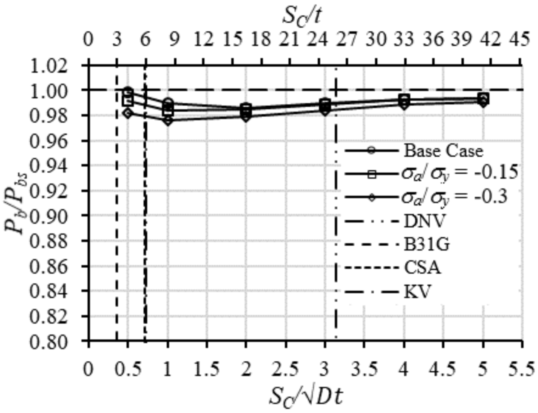

(e) *d/t*=0.6, $l^2/(Dt)$=2, *w/l*=0.5

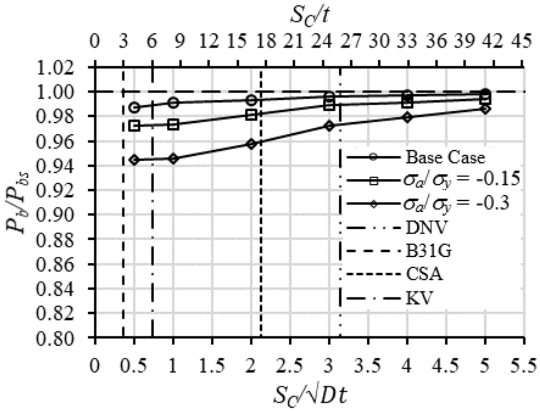

(f) *d/t*=0.6, $l^2/(Dt)$=2, *w/l*=1.5

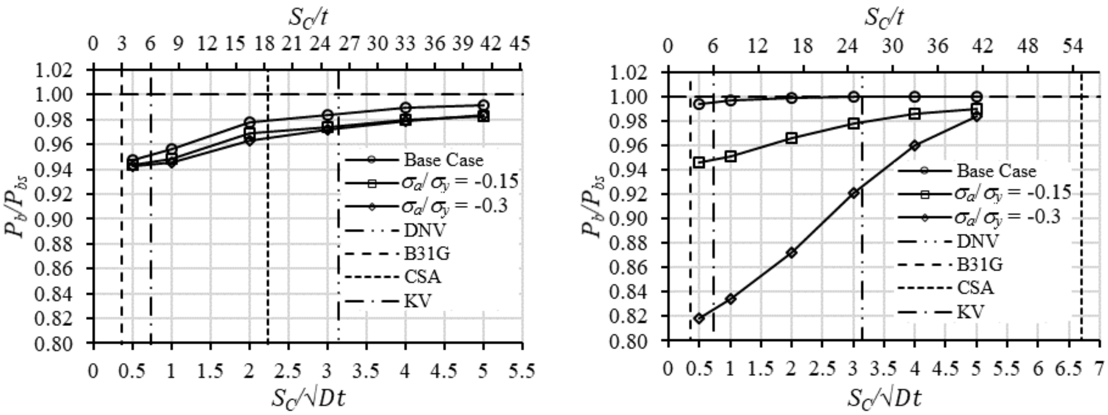

(g) d/t=0.6, $l^2/(Dt)$=20, w/l=0.5 (h) d/t=0.6, $l^2/(Dt)$=20, w/l=1.5

Figure 6.3 The interaction effect for circumferentially-aligned defects under combined loads for various combinations of d/t, $l^2/(Dt)$ and w/l

Under the internal pressure only (i.e. base case), there is no significant decrease in P_b/P_{bs} (within 5%) for all the analysis cases considered. This is consistent with the observations reported in the literature (Xu et al., 2017; Al-Owaisi et al., 2018; Sun and Cheng, 2018). Furthermore, Fig. 6.3(a) indicates that P_b is in fact slightly higher than P_{bs} for relatively shallow and narrow defects (d/t = 0.3 and w/l = 0.5) with a small separation distance ($S_C/\sqrt{Dt} < 2$). Leis and Stephens (1997) reported a similar observation and suggested that this can be explained by the local increase in the compliance of the pipe wall if a defect is circumferentially aligned with an adjacent defect. The interaction effect under the internal pressure only becomes weaker as the defect width increases with the other parameters unchanged. Overall, the interaction effect of circumferentially aligned defects is negligible under the internal pressure only. The corroded area projected on the longitudinal plane is unchanged by aligning another identical defect in the circumferential direction; therefore, the hoop stress remains more or less the same due to the circumferential equilibrium condition. As no additional axial stress is involved other than that induced by the internal pressure, the axial stress also remains unchanged. The above explanation is illustrated by the FEA results for the representative analysis cases with d/t=0.6, $l^2/(Dt)$=20, w/l = 1.5 and $S_C/\sqrt{Dt}$ = 0.5, 1, 2, 3, 4 and 5, respectively, at a fixed internal pressure of 9 MPa (Fig. 6.4). For all these cases, the critical point is the defect centre (i.e. the deepest point within the defected region), which is subjected to the maximum von Mises stress at a given internal pressure. This is consistent with observations obtained from full-scale burst tests of pipe specimens containing semi-ellipsoidal-shaped defects (Al-Owaisi et al., 2018). As illustrated in Fig. 6.4, the hoop, axial and von Mises stresses at the critical point of circumferentially aligned defects are practically identical to those in the corresponding single-defect case. Figure 6.5 depicts contours of the true von Mises stress on the pipe external surface for cases containing a single defect and circumferentially aligned defects with $S_C/\sqrt{Dt}$ = 0.5, 1 and 2, respectively (The contours are depicted in full model, as opposed to the half model, by employing the symmetry property through the ODB-Display-Options in ABAQUS). This figure clearly shows that the von Mises stresses for the two-defect cases are practically the same as those for the single-defect case under the internal pressure only.

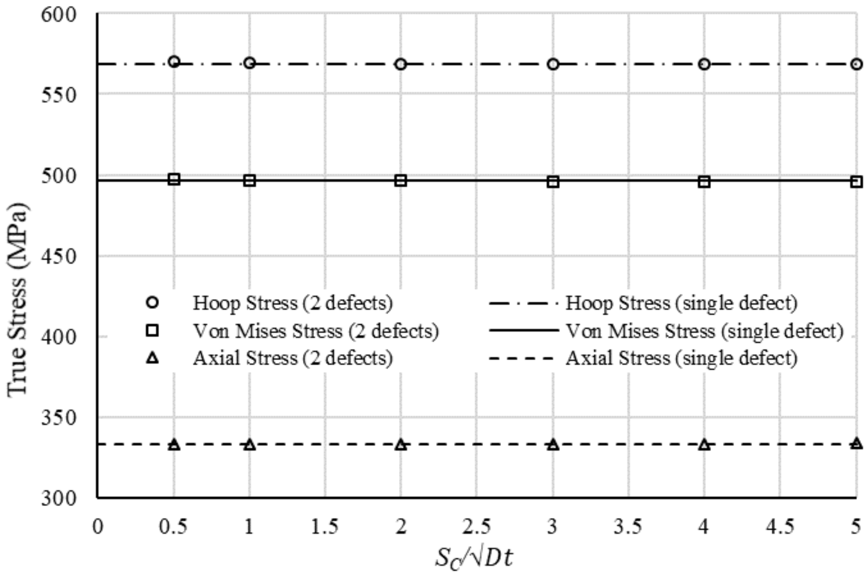

Figure 6.4 True hoop, axial and von Mises stresses at defect centre as a function of $S_C/\sqrt{Dt}$ for *d/t*=0.6, *l*^{2}/(*Dt*)=20 and *w/l* = 1.5 under the internal pressure (9 MPa) only

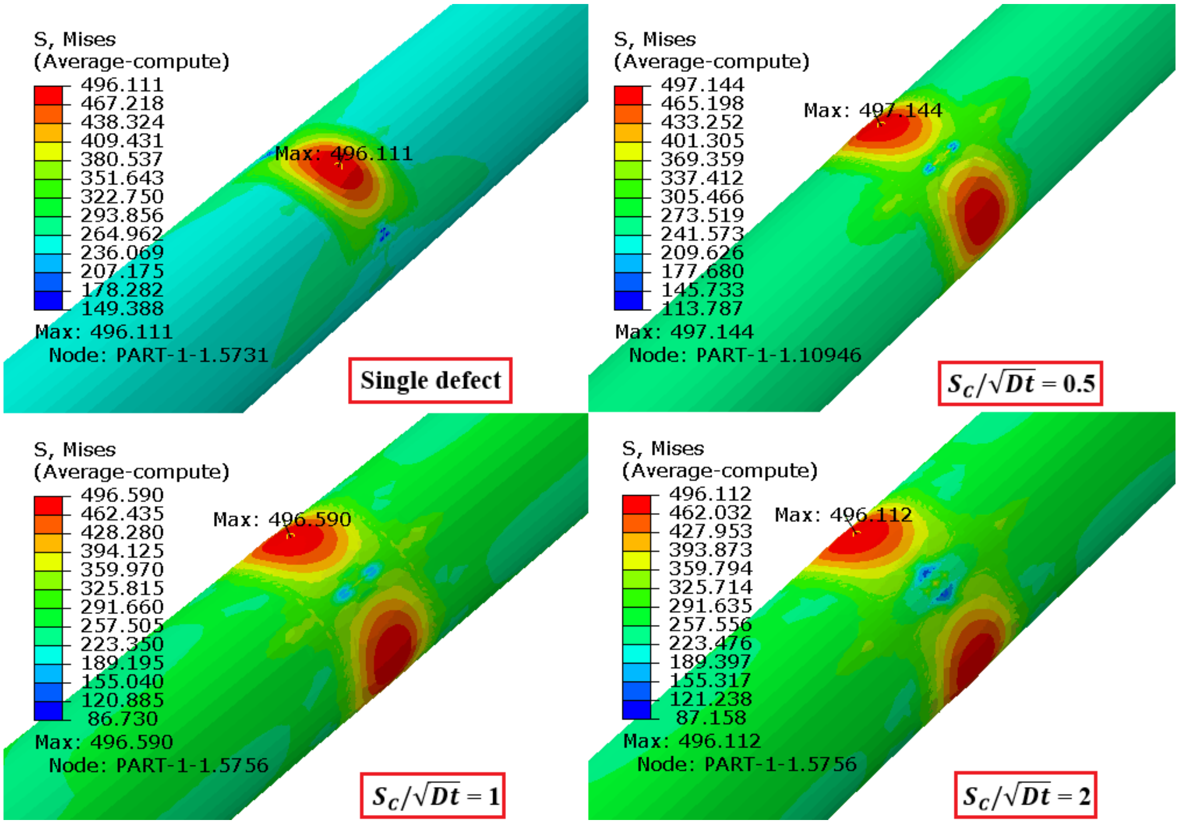

Figure 6.5 Contours of the von Mises stress for defect of *d*/*t*=0.6, $l^2/(Dt)$=20 and *w*/*l* = 1.5 under internal pressure (9 MPa) loading only

Figure 6.3 indicates that the interaction of circumferentially aligned defects is stronger under combined loads than that under the internal pressure only. The longitudinal compression enhances the interaction effect: the higher is the magnitude of σ_a, the greater is the interaction effect (all else being the same). Furthermore, the interaction of deep, long and wide defects is stronger than that of shallow, short and narrow defects: P_b/P_{bs} = 0.82 for the analysis case with *d*/*t* = 0.6, $l/\sqrt{Dt}$ = 20, *w*/*l* = 1.5, $S_C/\sqrt{Dt}$ = 0.5 and σ_a/σ_y = -0.3 (Fig. 6.3(h)), whereas P_b/P_{bs} = 0.99 for the case with *d*/*t* = 0.3, $l/\sqrt{Dt}$ = 2, *w*/*l* = 0.5, $S_C/\sqrt{Dt}$ = 0.5 and σ_a/σ_y = -0.3 (Fig. 6.3(a)). It is worth noting that the interaction effect under combined loads becomes stronger as the defect width increases. This is opposite to the influence of the defect width on the interaction effect under the internal pressure only.

Under a given set of combined loads, the pipe containing two closely-spaced circumferentially-aligned defects undergoes more significant bulging in the defected region than the pipe containing a single defect, as a result of reduced net cross-sectional area for the two-defect case. The enhanced bulging has the following effects on the stress field in the defected region as illustrated in Fig. 6.6: 1) it increases the maximum hoop stress within the region (Figs. 6.6(a) and 6.6(b)); 2) it causes the point of the maximum hoop stress to shift from the defect centre in the single-defect case toward the centre of the defect group in the two-defect case (Figs. 6.6(a) and 6.6(b)), and 3) it results in compressive axial stress on the internal surface of the pip wall in the two-defect case due to significant bending caused by the axial compression (Figs. 6.6(c) and 6.6(d)). As a result of these effects, the maximum von Mises stress in the two-defect case is markedly higher than that in the single-defect case (Figs. 6.6(e) and 6.6(f)). Furthermore, the location of the maximum von Mises stress shifts from the defect center (on the external surface) in the single-defect case toward the centre of the defect group on the internal surface of the pipe wall in the two-defect case (Figs. 6.6(e) and 6.6(f)). As the separation distance ($S_C/\sqrt{Dt}$) between the two defects increases, the defect-free region between the two defects becomes more effective in reducing the bulging of the defected region, thus reducing the maximum von Mises stress in the defected region and consequently interaction between the defects (Fig. 6.7). The maximum von Mises stress for the two-defect case with $S_C/\sqrt{Dt}$ = 5 (Fig. 6.7(e)) is almost the same as that for the single-defect case (Fig. 6.6(a)) under the same set of combined loads, indicating a negligible interaction between the defects.

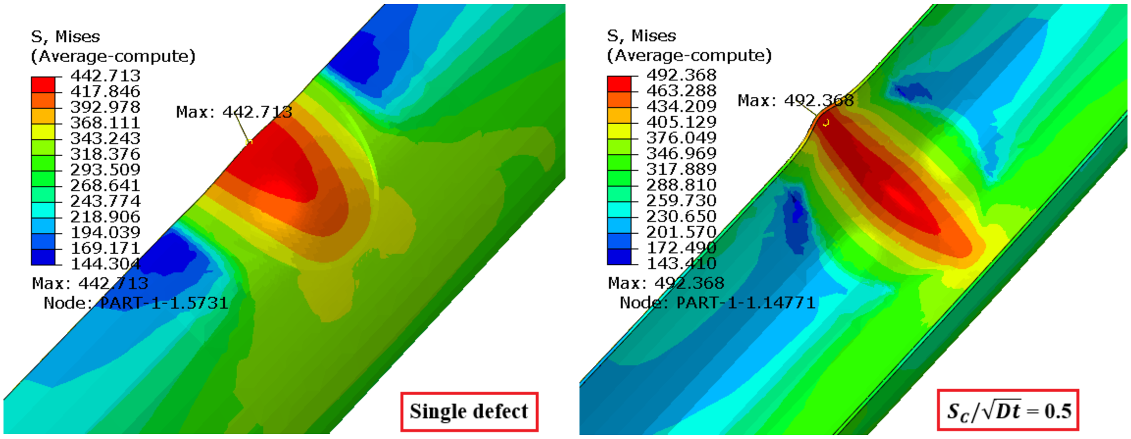

(a) von Mises stress in the single-defect case

(b) von Mises stress in the two-defect case

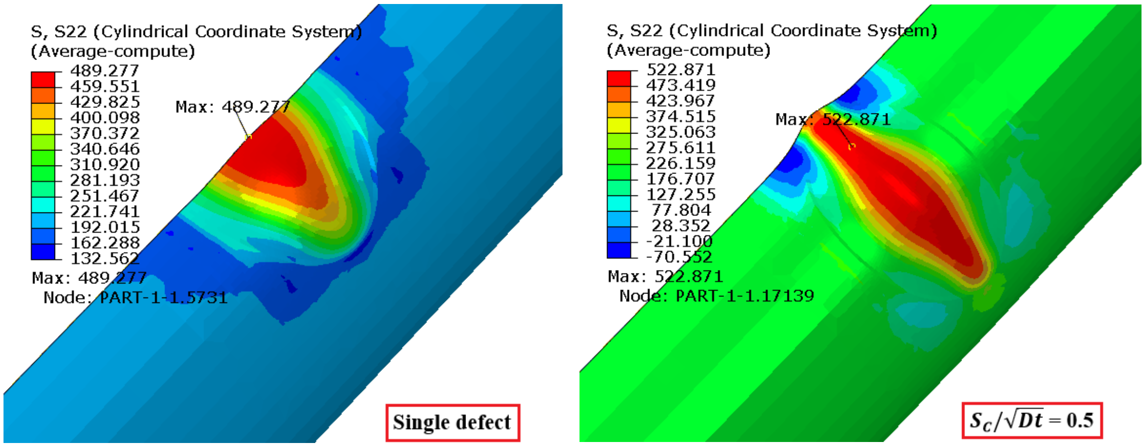

(c) Hoop stress in the single-defect case

(d) Hoop stress in the two-defect case

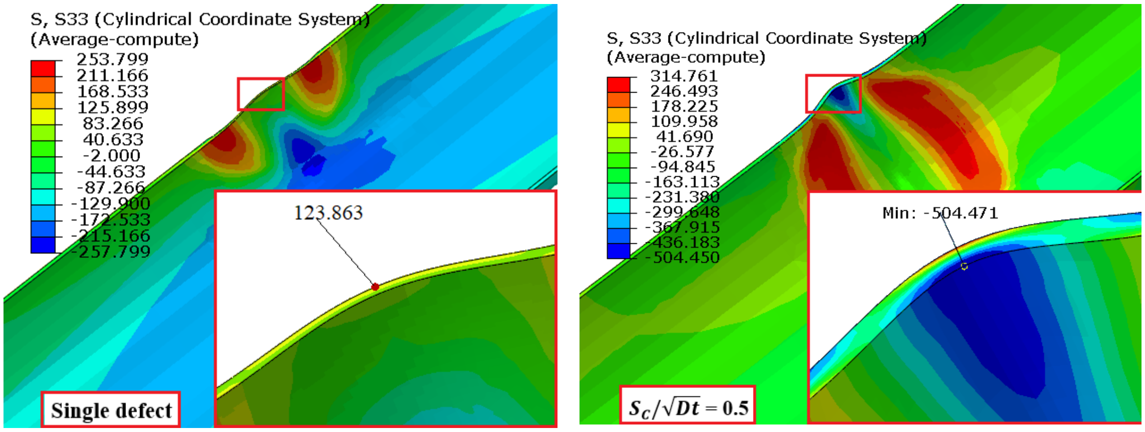

(e) Axial stress in the single-defect case

(f) Axial stress in the two-defect case

Figure 6.6 Contours of stress distribution patterns of cases containing single defect and circumferentially-closely-aligned defects ($S_C/\sqrt{Dt}$=0.5) under combined loads (internal pressure = 6.4 MPa and σ_a/σ_y = -0.3)

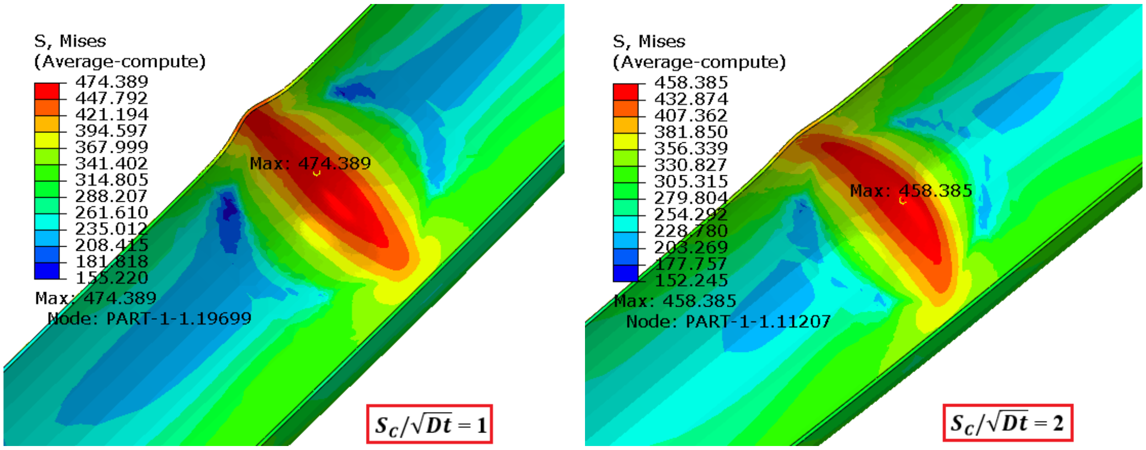

(a) von Mises stress in the two-defect case with $S_C/\sqrt{Dt}$=1

(b) von Mises stress in the two-defect case with $S_C/\sqrt{Dt}$=2

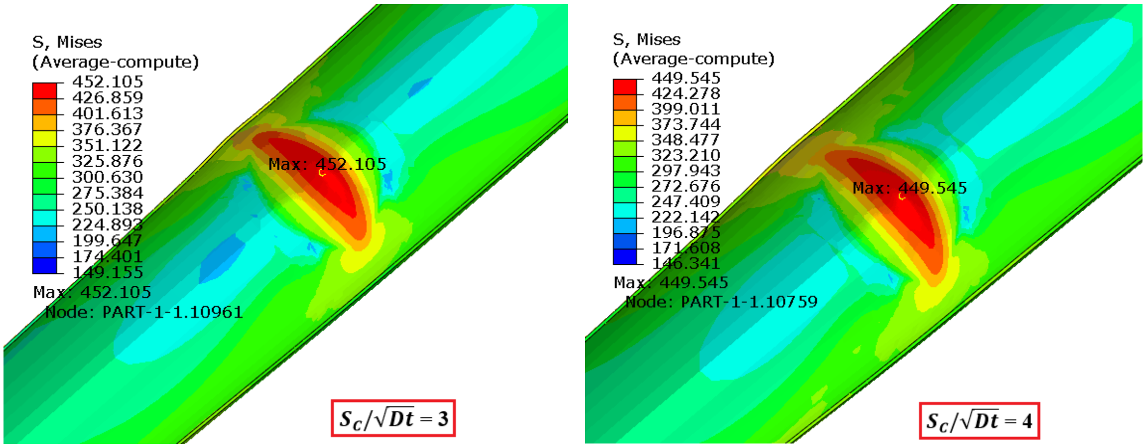

(c) von Mises stress in the two-defect case with $S_C/\sqrt{Dt}$=3

(d) von Mises stress in the two-defect case with $S_C/\sqrt{Dt}$=4

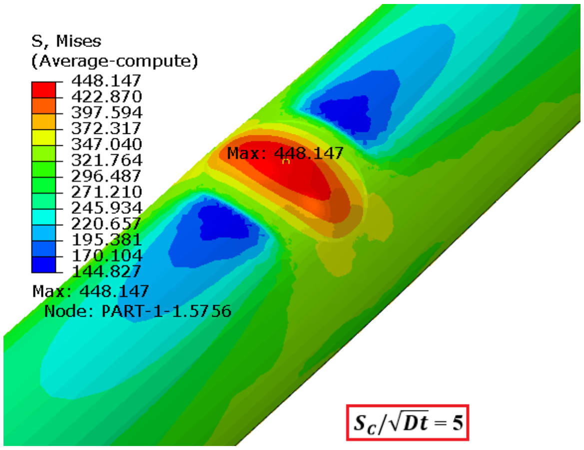

(e) von Mises stress in the two-defect case with $S_C/\sqrt{Dt}$=5

Figure 6.7 Contours of the von Mises stress distribution in the defected region for cases containing circumferentially-aligned defects ($S_C/\sqrt{Dt}$=1, 2, 3, 4 and 5) under combined loads (internal pressure = 6.4 MPa and σ_a/σ_y = -0.3)

6.3.3 Interaction effects of longitudinally-aligned defects

For brevity, P_b/P_{bs} for eight representative analysis cases are depicted in Fig. 6.8 corresponding to different combinations of d/t = 0.3 and 0.6, $l^2/(Dt)$= 2 and 20 and w/l= 0.5 and 1.5. The vertical lines in the figure correspond to four practical interaction rules and are explained in detail in Section 6.4. The results for the rest of the cases, for which the same trend of P_b/P_{bs} can be observed, are organized in Fig. D.1 of Appendix D. Figure 6.8 indicates that the interaction between longitudinally-aligned defects is negligible for $S_L/\sqrt{Dt} \geq 3$, regardless of the defect size and loading condition (i.e. internal pressure only or combined loads).

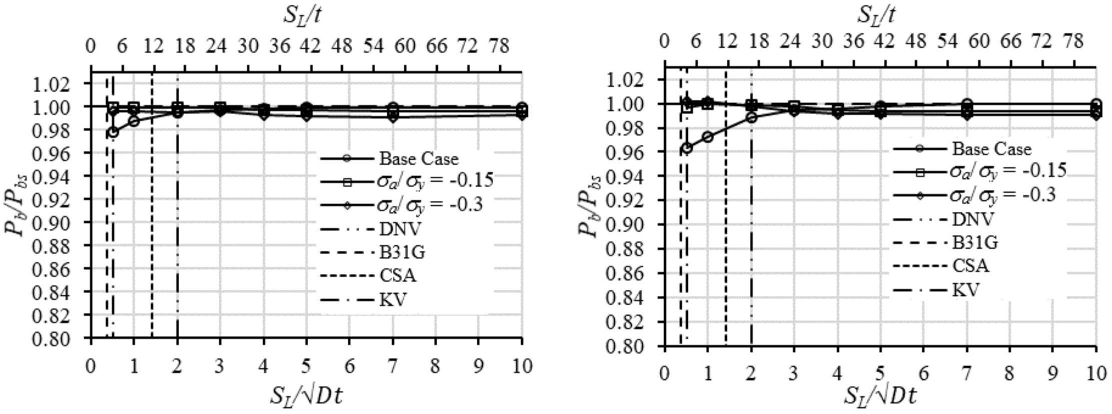

(a) *d/t*=0.3, $l^2/(Dt)$=2, *w/l*=0.5 (b) *d/t*=0.3, $l^2/(Dt)$=2, *w/l*=1.5

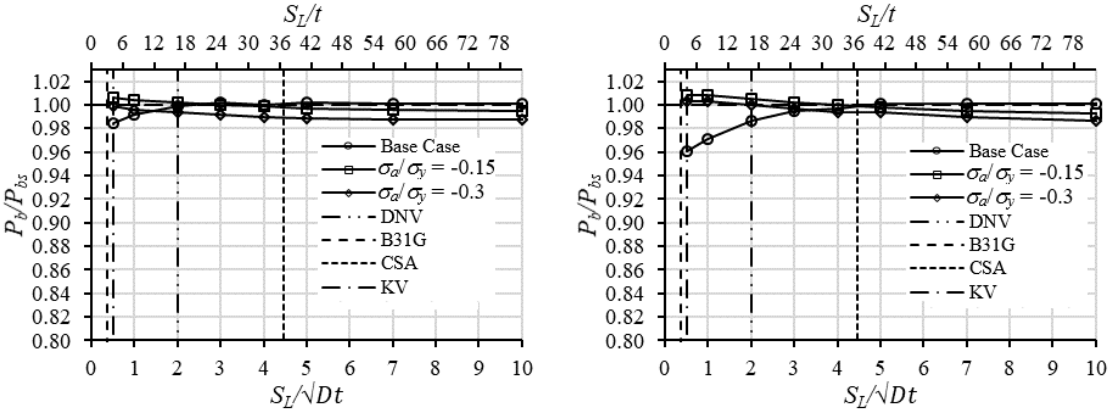

(c) *d/t*=0.3, $l^2/(Dt)$=20, *w/l*=0.5 (d) *d/t*=0.3, $l^2/(Dt)$=20, *w/l*=1.5

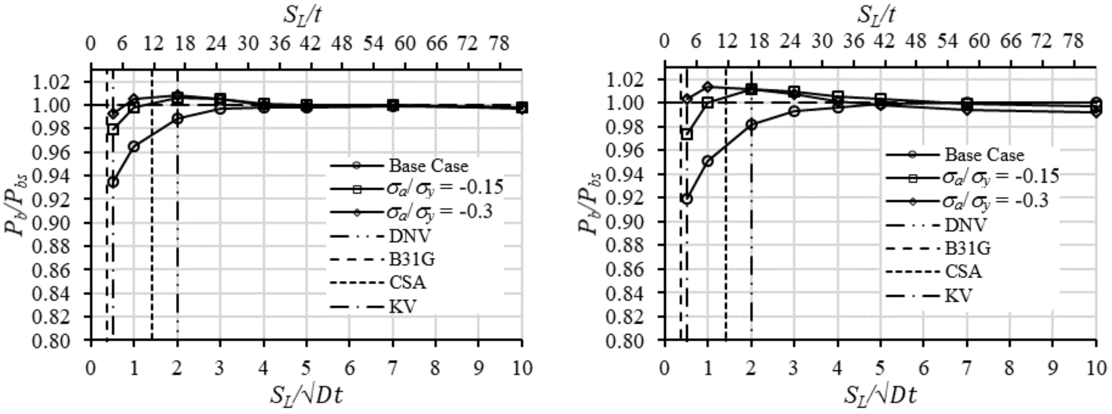

(e) *d/t*=0.6, $l^2/(Dt)$=2, *w/l*=0.5 (f) *d/t*=0.6, $l^2/(Dt)$=2, *w/l*=1.5

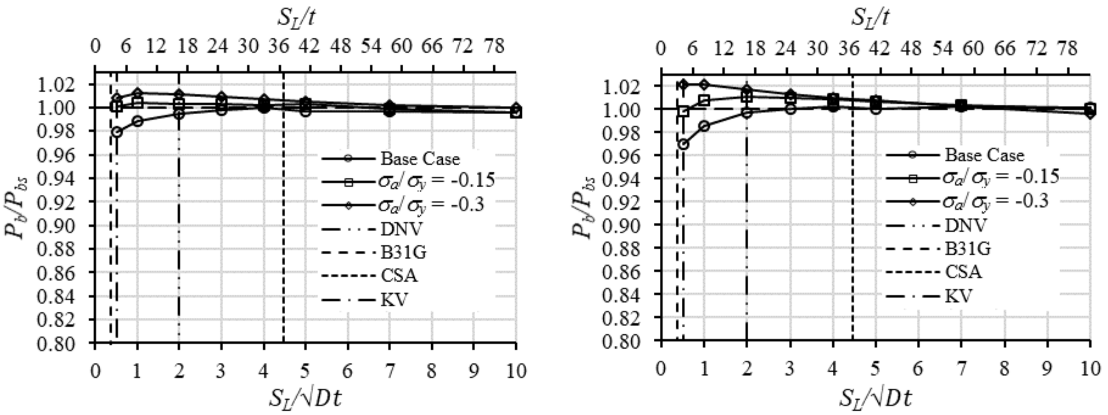

(g) *d/t*=0.6, $l^2/(Dt)$=20, *w/l*=0.5 (h) *d/t*=0.6, $l^2/(Dt)$=20, *w/l*=1.5

Figure 6.8 Interaction effect for longitudinally-aligned defects under combined loads with various combinations of *d/t*, $l^2/(Dt)$ and *w/l*

Under the internal pressure only (i.e. base case), the interaction effect noticeably strengthens as $S_L/\sqrt{Dt}$ decreases from 3 to 0.5. The interaction effect is marked for deep, relatively short defects, as shown in Figs. 6.8(e) and 6.8(f). These observations are consistent with those reported in previous studies (Silva et al., 2007; Li et al., 2016; Xu et al., 2017; Al-Owaisi et al., 2018; Sun and Cheng, 2018). The net cross-sectional area for resisting the hoop stress caused by the internal pressure in a two-defect case is less than that in a single-defect case. It follows that the maximum hoop stress, which is the dominant stress component, in the two-defect case is greater than that in the single-defect case. For small values of $S_L/\sqrt{Dt}$ and relatively short defects, the maximum hoop stress at each defect, which occurs at the defect centre (on the pipe external surface), is influenced by the adjacent defect, leading to the interaction effect. As $S_L/\sqrt{Dt}$ or the defect length increases, the influence of the adjacent defect on the maximum hoop stress decreases, thus diminishing the interaction effect.

Under combined loads, the interaction effect of longitudinally-aligned defects on the burst capacity is marginal (generally within 3%) as indicated in Fig. 6.8. The burst capacity of the two-defect case with a small separation distance ($S_L/\sqrt{Dt}$ < 4) in fact tends to be slightly higher than that of the single-defect case, and this phenomenon is more obvious for a larger magnitude of σ_a (Figs. 6.8(e) – 6.8(h)). This can be attributed to the so-called shielding effect as explained in the following. As confirmed by both experimental and numerical studies reported in the literature (Chouchaoui, 1995; Bjørnøy et al., 2000; Smith and Waldhart, 2000; Liu et al., 2009; Taylor et al., 2015; Mondal and Dhar, 2019), the burst capacity of a corroded pipeline under combined longitudinal compressive stress and internal pressure is lower than that of the same pipeline under the internal pressure only, and the adverse effect of longitudinal compression on the burst capacity is more significant as the magnitude of the compressive stress increases. For two longitudinally-aligned defects under combined loads, the longitudinal compressive stress acting on each defect is smaller than that in the single-defect case because the compressive stress is redistributed around the defects, i.e. the compressive stress in one defect is "shielded" by the other defect. This shielding effect is enhanced as the separation distance between the defects decreases or the defect depth increases or both. The shielding effect is illustrated in Fig. 6.9 using FEA results for the cases containing two defects of d/t=0.6, $l^2/(Dt)$=20 and w/l = 0.5 with $S_L/\sqrt{Dt}$ = 0.5, 1, 2, 3 and 5, respectively, compared with the corresponding single-defect case at a fixed longitudinal stress of σ_a/σ_y = -0.3 and zero internal pressure. As shown in Fig. 6.9, the magnitudes of the compressive stress in the defect-free region adjacent to the defect for the two-defect cases are always lower than that for the single-defect case. As $S_L/\sqrt{Dt}$ increases from 0.5 to 5, the compressive stress corresponding to the two-defect case gradually approaches that of the single-defect case. Note that the shielding effect is insignificant for shallow defects (Figs. 6.8(a)-6.8(d)). This can be explained by the insignificant redistribution of the longitudinal compressive stress due to the fact that the stiffness of the defected region is similar to that of the surrounding defect-free region for shallow defects. The absolute reduction in the magnitude of the compressive stress due to the shielding effect is more significant for σ_a/σ_y = -0.3 than that for σ_a/σ_y = -0.15, therefore resulting in a greater value of P_b/P_{bs} as shown in Figs. 6.8(e) – 6.8(h).

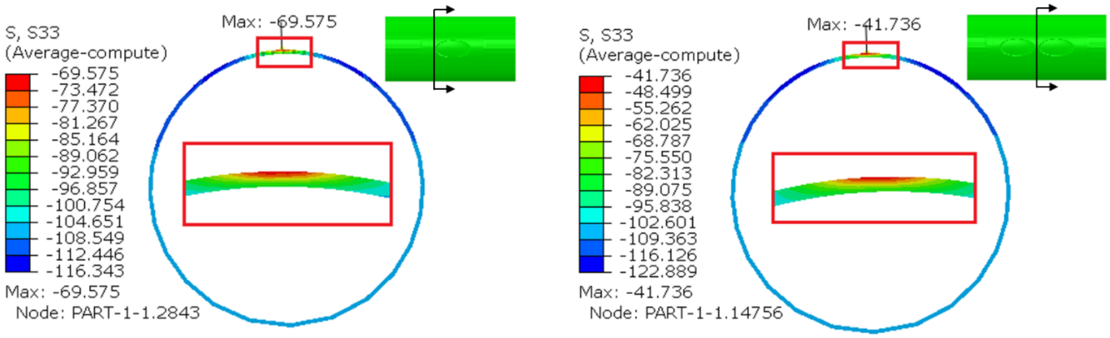

Single defect

$S_C/\sqrt{Dt} = 0.5$

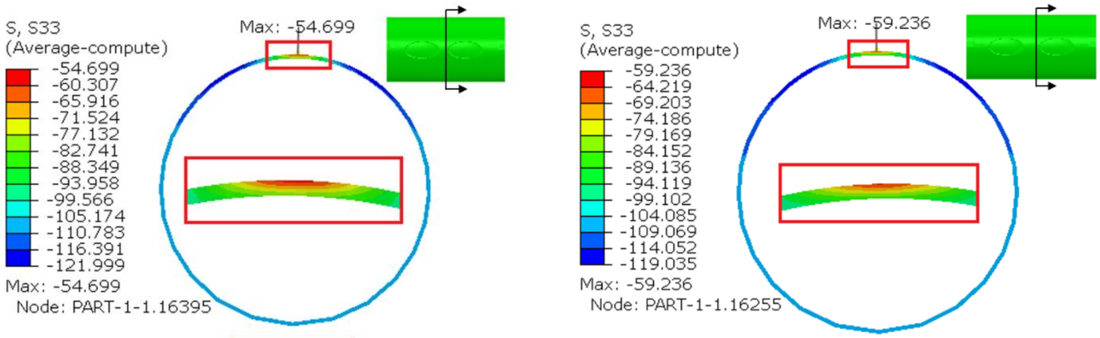

$S_C/\sqrt{Dt} = 1$

$S_C/\sqrt{Dt} = 2$

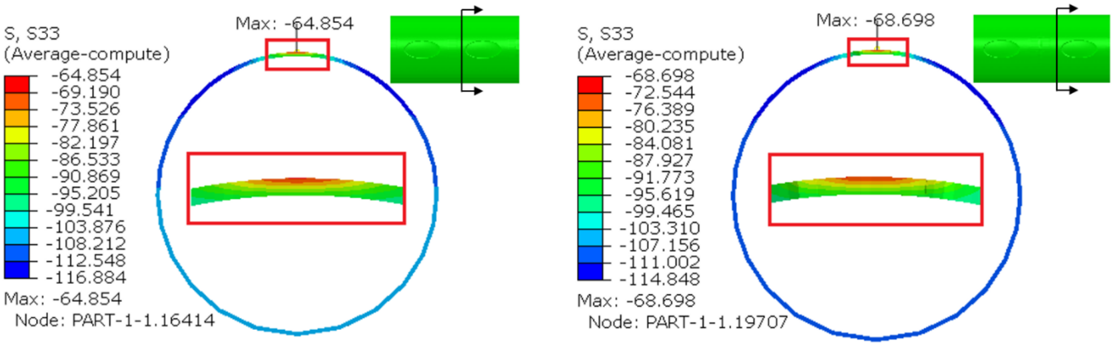

$S_C/\sqrt{Dt} = 3$

$S_C/\sqrt{Dt} = 5$

Figure 6.9 Contours of the axial stress for single- and two-defect cases with d/t=0.6, $l^2/(Dt)$=20 and w/l = 0.5 under σ_a/σ_y = -0.3

6.4 Adequacy of Current Interaction Rules

Practical interaction rules for corrosion defects under internal pressure only are generally expressed in the form of $S_C \leq S_C^{crit}$ and $S_L \leq S_L^{crit}$; that is, two defects are considered to interact with each other if $S_C \leq S_C^{crit}$ and $S_L \leq S_L^{crit}$ are satisfied simultaneously, where S_C^{crit} and S_L^{crit} respectively denote the critical circumferential and longitudinal separation distances between the defects. The critical separation distances are usually functions of pipe geometric properties such as *D* and *t*, or defect sizes such as the defect length and width. The adequacy of four well-known defect interaction rules for the combined loading condition is examined, namely the interaction rules suggested in DNV RP F101 (DNV) (2017), B31G (2017) and CSA Z662 (CSA) (2019) as well as that recommended by Kiefner and Vieth (KV) (1990). The expressions for S_C^{crit} and S_L^{crit} in these rules are summarized in Table 6.5.

Table 6.5 Expressions for S_C^{crit} and S_L^{crit} in four interaction rules

Interaction rule	S_C^{crit}	S_L^{crit}
DNV RP F101	$\pi\sqrt{Dt}$	$2\sqrt{Dt}$
B31G	$3t$	$3t$
CSA Z662	Min (w_1, w_2)	Min (l_1, l_2)
Kiefner and Vieth	$6t$	25.4 mm (1 inch)

Note: w_1 (l_1) and w_2 (l_2) are the widths (lengths) of the two adjacent defects, respectively.

The adequacy of the above four interaction rules for circumferentially- and longitudinally-aligned defects under combined loads is depicted in Figs. 6.3 and 6.8, respectively, where the vertical lines in the figures represent S_C^{crit} and S_L^{crit} values in the interaction rules. The results in Fig. 6.3 indicate that the B31G and KV rules are non-conservative for circumferentially-aligned defects under combined loads except for the cases involving shallow, short and narrow defects (Fig. 6.3(a)), where the interaction effect is negligible. The DNV rule is non-conservative for the cases involving long, wide defects under large longitudinal compression (Figs. 6.3(d) and 6.3(h)), but generally adequate for the other cases. The CSA rule can be overly conservative for long, wide defects (Figs. 6.3(d) and 6.3(h)), but otherwise is reasonably adequate. That none of the four interaction rules is adequate for all of the parametric cases involving combined loads is attributed to the fact that these interaction rules are developed for the internal pressure only as opposed to combined loads. As depicted in Fig. 6.3, P_b/P_{bs} approximately equals 1.0 at $S_C/\sqrt{Dt}$ = 5 for all the cases regardless of the defect sizes and loading condition (i.e. internal pressure only or combined loads). On the other hand, the slopes of P_b/P_{bs} curves for different analysis cases involving combined loads shown in Fig. 6.3 clearly depend on the defect sizes (i.e. d/t, $l/\sqrt{Dt}$ and w/l) as well as (σ_a/σ_y); in other words, to what extent the interaction effect impacts the burst capacity under combined loads is clearly influenced by d/t, $l/\sqrt{Dt}$, w/l and σ_a/σ_y. These observations suggest that an interaction rule adequate for circumferentially-aligned defects under combined loads should involve D, t, d/t, $l/\sqrt{Dt}$, w/l as well as σ_a/σ_y. Developing such an interaction rule is however beyond the scope of the current study. As shown in Fig. 6.8, the interaction between longitudinally-aligned defects under combined loads is generally negligible due to the shielding effect. This is in direct contrast to the significant interaction between longitudinally-aligned defects under the internal pressure only. It follows that the interaction rules summarized in Table 6.5, which are developed for the internal pressure only, are unnecessary for longitudinally-aligned defects under combined loads.

6.5 Conclusions

The present study in this chapter employs 3D elasto-plastic FEA to investigate the interaction between closely-spaced corrosion defects on the burst capacity of corroded pipelines under combined internal pressure and load-controlled longitudinal compression. The corrosion defects are idealized as semi-ellipsoidal-shaped. The UTS-based failure criterion is adopted to predict the burst capacity of the corroded pipe model in FEA. The finite element model and failure criterion are validated by full-scale burst tests of 12 pipe specimens reported in the literature.

The results of a large number of parametric FEA cases indicate that the interaction between circumferentially-aligned defects is significant under combined loads, as a result of the enhanced bulging of the defected region due to the presence of the longitudinal compression. In contrast, the interaction effect is marginal for circumferentially-aligned defects subjected to internal pressure only. The interaction effect is particularly strong for cases involving deep, long and wide defects under a relatively large magnitude of compressive stress; for example, P_b/P_{bs} equals 0.82 for d/t = 0.6, $l/\sqrt{Dt}$ = 20, w/l = 1.5, $S_C/\sqrt{Dt}$ = 0.5 and σ_a/σ_y = -0.3. The interaction effect is negligible for $S_C/\sqrt{Dt} \geq 5$, as the defect-free region between the two defects can effectively resist the bulging. Four well-known practical interaction rules, i.e. the DNV, B31G, CSA and KV rules, are investigated in terms of their adequacy under combined loads. It is observed that the B31G and KV rules are generally inadequate, whereas the DNV and CSA rules are non-conservative or overly conservative, respectively, for two circumferentially-aligned defects that are long and wide.

Results of parametric FEA reveal that the interaction between closely-spaced, longitudinally-aligned defects under combined loads is negligible due to the shielding effect. This shielding effect is enhanced as the separation distance between the defects decreases and/or the defect depth increases. In fact, the shielding effect can result in the burst capacity for the two-defect case with a small separation distance ($S_L/\sqrt{Dt} < 4$) being slightly higher than that for the single-defect case under combined loads. In contrast, the burst capacity of two longitudinally-aligned defects subjected to internal pressure only can be markedly lower than that of a single defect. These results suggest that it is unnecessary to apply the interaction rule to longitudinally-aligned defects under combined loads.

It is emphasized that the observations and findings of the present study are predicated on the basic assumption employed in the parametric FEA, i.e. two identical defects separated longitudinally or circumferentially. Further investigations are needed to understand the interaction effects associated with more complex (and realistic) scenarios such as two defects with different sizes separated both longitudinally and circumferentially.

Reference

Al-Owaisi, S., Becker, A. A., Sun, W., Al-Shabibi, A., Al-Maharbi, M., Pervez, T., & Al-Salmi, H., 2018. An experimental investigation of the effect of defect shape and orientation on the burst pressure of pressurised pipes. *Engineering Failure Analysis*, *93*, 200-213.

Arumugam, T., Rosli, M. K. A. M., Karuppanan, S., Ovinis, M., & Lo, M., 2020. Burst capacity analysis of pipeline with multiple longitudinally aligned interacting corrosion defects subjected to internal pressure and axial compressive stress. *SN Applied Sciences*, *2*(7), 1-11.

ASME B31G-2012., R2017. Manual for Determining the Remaining Strength of Corroded Pipelines: *Supplement to ASME B31 Code for Pressure Piping: an American National Standard.* The American Society of Mechanical Engineers.

Bao, J., Zhang, S., Zhou, W., & Zhang, S., 2018. Evaluation of Burst Pressure of Corroded Pipe Segments Using Three-Dimensional Finite Element Analyses. In 2018 12th International Pipeline Conference (pp. V001T03A043-V001T03A043). American Society of Mechanical Engineers.

Benjamin, A. C., Freire, J. L. F., Vieira, R. D., Diniz, J. L., & de Andrade, E. Q., 2005. Burst tests on pipeline containing interacting corrosion defects. In *ASME 2005 24th International Conference on Offshore Mechanics and Arctic Engineering* (pp. 403-417). American Society of Mechanical Engineers Digital Collection.

Benjamin, A. C., de Andrade, E. Q., Jacob, B. P., Pereira, L. C., & Machado, P. R., 2006. Failure behavior of colonies of corrosion defects composed of symmetrically arranged defects. In *2006 International Pipeline Conference* (pp. 417-432). American Society of Mechanical Engineers Digital Collection.

Bjørnøy, O. H., Sigurdsson, G., & Cramer, E., 2000. Residual strength of corroded pipelines, DNV test results. In *The Tenth International Offshore and Polar Engineering Conference*. International Society of Offshore and Polar Engineers.

Bruère, V. M., Bouchonneau, N., Motta, R. S., Afonso, S. M., Willmersdorf, R. B., Lyra, P. R. M., Torres, J. V. S., Andrade, E. Q., Cunha, D. J., 2019. Failure pressure prediction of corroded pipes under combined internal pressure and axial compressive force. *Journal of the Brazilian Society of Mechanical Sciences and Engineering*, *41*(4), 172.

Canadian Standard Association, (CSA), 2019. Oil and gas pipeline systems. CSA standard Z662-19. *Mississauga, Ontario, Canada*.

Chouchaoui, B., 1995. Evaluating the remaining strength of corroded pipelines, PhD thesis, University of Waterloo.

Cronin, D. S., 2000. Assessment of corrosion defects in pipelines, PhD thesis, University of Waterloo.

Cunha, S. B., Pacheco, M., & da Silva, A. B., 2016. Numerical Simulations of Burst of Corroded Pipes With Thermally Induced Compressive Axial Strain. *In International Pipeline Conference* (Vol. 50251, p. V001T03A002). American Society of Mechanical Engineers.

Dassault Systèmes, D. S., 2016. Abaqus analysis user's guide. Technical Report Abaqus 2016 Documentation, Simulia Corp.

Det Norske Veritas (DNV), 2017. "Recommended practice DNV-RP-F101, corroded pipelines", Hovic, Norway.

Dowling, N. E., 2007. Mechanical behavior of materials. Prentice Hall, New Jersey

Karimian, S. A., 2006. Response of buried steel pipelines subjected to longitudinal and transverse ground movement, Doctoral dissertation, University of British Columbia.

Kiefner, J. F., & Vieth, P. H., 1990. Evaluating pipe – Conclusion. PC program speeds new criterion for evaluating corroded pipe. *Oil and Gas Journal*, *88*(34).

Kuppusamy, C. S., Karuppanan, S., & Patil, S. S., 2016. Buckling strength of corroded pipelines with interacting corrosion defects: Numerical analysis. *International Journal of Structural Stability and Dynamics*, *16*(09), 1550063.

Leis, B. N., & Stephens, D. R., 1997. An alternative approach to assess the integrity of corroded line pipe-part I: current status. In *The Seventh International Offshore and Polar Engineering Conference*. International Society of Offshore and Polar Engineers.

Liu, J., Chauhan, V., Ng, P., Wheat, S., & Hughes, C., 2009. Remaining strength of corroded pipe under secondary (biaxial) loading (Report No. R9068). GL Industrial Services UK Ltd.

Li, X., Bai, Y., Su, C., & Li, M., 2016. Effect of interaction between corrosion defects on failure pressure of thin wall steel pipeline. *International Journal of Pressure Vessels* *and Piping, 138*, 8-18.

Meidani, M., Meguid, M. A., & Chouinard, L. E., 2017. Evaluation of soil–pipe interaction under relative axial ground movement. *Journal of Pipeline Systems Engineering and Practice, 8*(4), 04017009.

Meidani, M., Meguid, M. A., & Chouinard, L. E., 2018. Estimating earth loads on buried pipes under axial loading condition: insights from 3D discrete element analysis. *International Journal of Geo-Engineering, 9*(1), 5.

Mondal, B. C., & Dhar, A. S., 2019. Burst pressure of corroded pipelines considering combined axial forces and bending moments. *Engineering Structures, 186*, 43-51.

Silva, R. C. C., Guerreiro, J. N. C., & Loula, A. F. D., 2007. A study of pipe interacting corrosion defects using the FEM and neural networks. *Advances in Engineering Software, 38*(11-12), 868-875.

Smith, M. Q., & Waldhart, C. J., 2000. Combined loading tests of large diameter corroded pipelines. In *2000 3rd International Pipeline Conference*. American Society of Mechanical Engineers Digital Collection.

Sun, J., & Cheng, Y. F., 2018. Assessment by finite element modeling of the interaction of multiple corrosion defects and the effect on failure pressure of corroded pipelines. *Engineering Structures*, 165, 278-286.

Taylor, N., Clubb, G., & Matheson, I., 2015. The Effect of Bending and Axial Compression on Pipeline Burst Capacity. In *SPE Offshore Europe Conference and Exhibition*. Society of Petroleum Engineers.

Wang, L., & Zhang, Y., 2011. Plastic collapse analysis of thin-walled pipes based on unified yield criterion. *International Journal of Mechanical Sciences, 53*(5), 348-354.

Wijewickreme, D., Karimian, H., & Honegger, D., 2009. Response of buried steel pipelines subjected to relative axial soil movement. *Canadian Geotechnical Journal, 46*(7), 735-752.

Xu, W. Z., Li, C. B., Choung, J., & Lee, J. M., 2017. Corroded pipeline failure analysis using artificial neural network scheme. *Advances in engineering software, 112*, 255-266.

Zhang, S., & Zhou, W., 2020. Assessment of effects of idealized defect shape and width on the burst capacity of corroded pipelines. *Thin-Walled Structures*, 154, 106806.

Zhu, X. K., & Leis, B. N., 2004. Strength criteria and analytic predictions of failure pressure in line pipes. *International Journal of Offshore and Polar Engineering*, *14*(02), 125-131.

Zhu, X. K., & Leis, B. N., 2005. Influence of yield-to-tensile strength ratio on failure assessment of corroded pipelines. *Journal of Pressure Vessel Technology*, *127*(4), 436-442.

7 Summary, Conclusions and Recommendations for Future Study

7.1 General

The research conducted and described in this thesis employs finite element analysis (FEA), multivariate nonlinear regression analysis and machine learning techniques (e.g. artificial neural network) to address five issues regarding the integrity assessment of corroded pipelines. The conclusions drawn from this thesis along with the recommendation for future study are given as follows.

7.2 Assessment of Effects of Idealized Defect Shape and Width on the Burst Capacity of Corroded Pipeline

In Chapter 2, full-scale burst test results of eleven pipe specimens containing naturally-occurring corrosion defects are used to examine implications of the rectangular and semi-ellipsoidal idealizations for the FEA-based burst capacity prediction. It is observed that both idealizations lead to overly conservative predictions for naturally-occurring defects with $d/t \geq 0.7$. For defects with $d/t < 0.7$, the rectangular and semi-ellipsoidal idealizations lead to on average 31 and 17% under-predictions, respectively, of the burst capacity. Furthermore, the COV (15%) of the predictions corresponding to the semi-ellipsoidal idealization is slightly lower than that (18%) corresponding to the rectangular idealization.

The defect width effect on the burst capacity of corroded pipelines is then investigated by employing the semi-ellipsoidal defect idealization by carrying out extensive parametric FEA. It is observed that the burst capacity increases as the defect width increases, all else remaining the same. The width effect is the strongest for deep, relatively short defects: the burst capacity increases by about 15% as w/l increases from 0.25 to 2 for a defect with $d/t = 0.6$ and $l^2/(Dt) = 2$. For long defects with $w/l \leqslant 1.5$, the width effect is marginal regardless of the defect depth. For moderately long defects with $w/l \leqslant 1.5$, the width effect can lead to 5-10% increase of the burst capacity depending on the defect depth. The width effect observed in the present study is opposite to that reported in the literature, which idealizes corrosion defects as rectangular-shaped. The underlying mechanisms for the width effects reported in the present study and literature are explained by considering the contributions of the membrane and bending components to the hoop stress in the defect region. The findings of the study in Chapter 2 suggest that the width effect is significant and beneficial for deep, relatively short corrosion defects, and therefore should be appropriately accounted for in the empirical burst capacity models for corroded pipelines.

7.3 Development of a Burst Capacity Model for Corroded Pipelines Considering Corrosion Defect Width and a Revised Folias Factor Equation

Chapter 3 proposes a burst capacity model for corroded oil and gas pipelines based on extensive parametric 3D elasto-plastic FEA validated by full-scale burst tests. The proposed model idealizes a corrosion defect to be semi-ellipsoidal-shaped as it better approximates the geometry of real corrosion defects than the commonly used rectangular (or cubic) idealization. The model follows the basic form of the NG-18 equation, and incorporates the defect width effect, a new Folias factor equation that depends on both the defect depth and length, and the flow stress defined as a function of the strain hardening exponent and ultimate tensile strength of the pipe steel. The equations for the Folias factor and defect width effect in the proposed model are developed by nonlinear curve fitting of FEA results. The accuracy of the proposed burst capacity model is demonstrated based on extensive parametric FEA and shown to be higher than those of seven existing burst capacity models for corroded pipelines, including B31G, B31G-M, CSA, DNV, RSTRENG and SHELL92 as well as the model recently developed by Sun et al. The validation of the proposed model further indicates that it can be applied to corrosion defects with d/t ranging from 0.3 to 0.65 and $l^2/(Dt)$ ranging from 2 to 100. These ranges are sufficient for the proposed model to be applied in practical fitness-for-service assessment of corroded pipelines.

7.4 Development of a Burst Capacity Model for Corroded Pipelines under Internal Pressure and Axial Compression Using Artificial Neural Network

Chapter 4 investigates the burst capacity of corroded pipelines under combined internal pressure and longitudinal compression loading condition based on extensive parametric 3D elastic-plastic FEA and artificial neural network technique. It is observed that the longitudinal compressive stress can markedly reduce the burst capacity of corroded pipelines. The adverse effect of the compressive stress on the burst capacity is the strongest for wide, relatively shallow defects, and relatively insensitive to the defect length.

Based on the parametric FEA results, an ANN model is developed in the open-source platform PYTHON, to predict the burst capacity of pipelines containing single corrosion defects under internal pressure only or combined internal pressure and axial compression. The ANN model is validated using 105 FEA cases and 9 full-scale burst tests conducted by DNV and the results indicates good accuracy of the ANN model.

7.5 A Burst Capacity Model for Corroded Pipelines Subjected to Combined Internal Pressure and Longitudinal Compression

Chapter 5 develops a semi-empirical burst capacity model for corroded oil and gas pipelines subjected to the combined internal pressure and longitudinal compression. The proposed model is expressed as the burst capacity for corroded pipelines under internal pressure only multiplied by a correction factor to account for the adverse impact of the longitudinal compression on the burst capacity. The correction factor for the longitudinal compression is considered as a function of the defect depth, length and width as well as the magnitude of the longitudinal compressive stress, and developed based on multivariate nonlinear regression analyses of results of 477 parametric FEA cases. The accuracy of the proposed model is validated by 1431 additional parametric FEA cases and full-scale burst tests of corroded pipe specimens reported in the literature. In particular, the proposed model is shown to be markedly more accurate than the DNV and RPA-PLLC models in terms of quantifying the influence of longitudinal compression on the bust capacity of corroded pipelines. The DNV and RPA-PLLC models are found to be inadequate to quantify the longitudinal compression effect on the burst capacity based. The proposed model is a viable practical tool to carry out fitness-for-service assessments of corroded pipelines subjected to combined internal pressure and longitudinal compression.

7.6 Assessment of the interaction of corrosion defects on steel pipelines under combined internal pressure and longitudinal compression using finite element analysis

Chapter 6 investigates the interaction between closely-spaced corrosion defects on the burst capacity of corroded pipelines under combined internal pressure and load-controlled longitudinal compression by employing 3D elasto-plastic FEA. The results of a large number of parametric FEA cases indicate that the interaction between circumferentially-aligned defects is significant under combined loads, as a result of the enhanced bulging of the defected region due to the presence of the longitudinal compression. In contrast, the interaction effect is marginal for circumferentially-aligned defects subjected to internal pressure only. The interaction effect is particularly strong for cases involving deep, long and wide defects under a relatively large magnitude of compressive stress; for example, P_b/P_{bs} equals 0.82 for $d/t = 0.6$, $l/\sqrt{Dt} = 20$, $w/l = 1.5$, $S_C/\sqrt{Dt} = 0.5$ and $\sigma_a/\sigma_y = -0.3$. The interaction effect is negligible for $S_C/\sqrt{Dt} \geq 5$, as the defect-free region between the two defects can effectively resist the bulging. Four well-known practical interaction rules, i.e. the DNV, B31G, CSA and KV rules, are investigated in terms of their adequacy under combined loads. It is observed that the B31G and KV rules are generally inadequate, whereas the DNV and CSA rules are non-conservative or overly conservative, respectively, for two circumferentially-aligned defects that are long and wide.

Results of parametric FEA reveal that the interaction between closely-spaced, longitudinally-aligned defects under combined loads is negligible due to the shielding effect. This shielding effect is enhanced as the separation distance between the defects decreases and/or the defect depth increases. In fact, the shielding effect can result in the burst capacity for the two-defect case with a small separation distance ($S_L/\sqrt{Dt} < 4$) being slightly higher than that for the single-defect case under combined loads. In contrast, the burst capacity of two longitudinally-aligned defects subjected to internal pressure only can be markedly lower than that of a single defect. These results suggest that it is unnecessary to apply the interaction rule to longitudinally-aligned defects under combined loads.

7.7 Recommendations for future study

The recommendations for the future study are summarized as follows:

1. The burst capacity model proposed in Chapter 3 has proved to be more accurate than seven existing burst capacity models for corroded pipelines, i.e., B31G, B31G-M, CSA, DNV, RSTRENG, SHELL92 and Sun et al.'s model, whereas the model is proposed with corrosion defect idealized as semi-ellipsoidal-shaped. It would be valuable to apply the model to individual naturally-occurring corrosion defects to further investigate the accuracy of the model.

2. The experimental data for investigating the influence of longitudinal compression the burst capacity of corroded pipeline is very limited. Besides, the existing experimental tests are conducted with rectangular-shaped defects. It would be a good topic to experimentally investigate the longitudinal compression effect on the burst capacity with naturally-occurring corrosion defects.

3. The observations and findings of Chapter 6 are predicated on the basic assumption employed in the parametric FEA, i.e. two identical defects separated longitudinally or circumferentially. Further investigations are needed to understand the interaction effects associated with more complex (and realistic) scenarios such as two defects with different sizes separated both longitudinally and circumferentially.

Appendices

Appendix A

The photos of naturally-occurring corrosion defects on two represented pipe specimens (16-6 and 16-7) from Table 3 as well as their rectangular and semi-ellipsoidal idealizations in FEA are depicted sin the figures below.

(a) Naturally-occurring corrosion defect on pipe specimen 16-6

(b) Naturally-occurring corrosion defect on pipe specimen 16-7

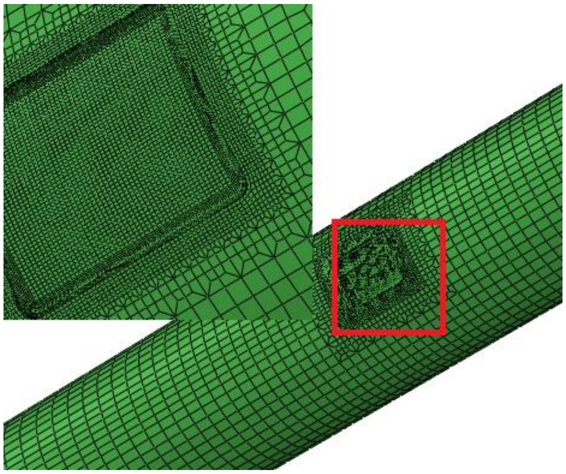

(c) Rectangular idealization of corrosion defect on specimen 16-6 in FEA

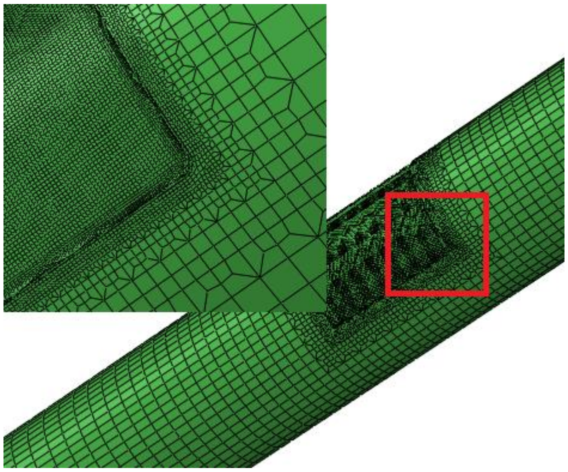

(d) Rectangular idealization of corrosion defect on specimen 16-7 in FEA

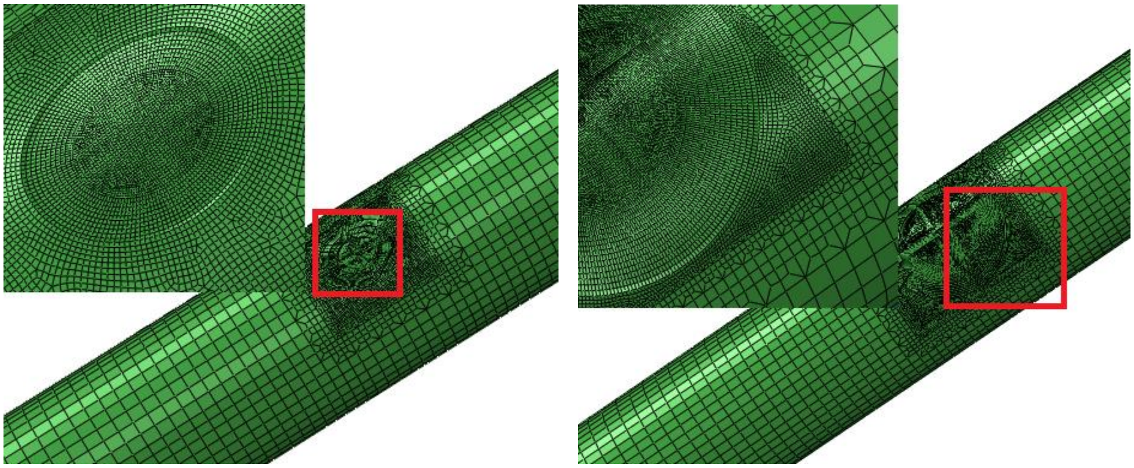

(e) Semi-ellipsoidal idealization of corrosion defect on specimen 16-6 in FEA

(f) Semi-ellipsoidal idealization of corrosion defect on specimen 16-7 in FEA

Figure A.1 Naturally-occurring corrosion defects and corresponding idealization in FEA on pipe specimens 16-6 and 16-7

Appendix B

Table B.1 Summary of FEA-predicted burst capacities (MPa) for all the parametric analysis cases to investigate the defect width effect

$l^2/(Dt)$	w/l	d/t=0.30	d/t =0.45	d/t =0.60
2	0.25	12.25	11.26	10.20
	0.50	12.67	11.80	10.84
	0.75	12.86	12.03	11.00
	1.00	13.05	12.23	11.22
	1.25	13.15	12.43	11.41
	1.50	13.25	12.58	11.61
	1.75	13.34	12.68	11.75
	2.00	13.37	12.78	11.88
5	0.25	12.07	10.79	9.35
	0.50	12.40	11.23	9.78
	0.75	12.59	11.46	10.00
	1.00	12.81	11.71	10.23
	1.25	12.94	11.84	10.37
	1.50	13.02	12.03	10.59
	1.75	13.11	12.15	10.73
	2.00	13.13	12.23	10.77
15	0.25	11.78	10.21	8.32
	0.50	12.04	10.49	8.56
	0.75	12.24	10.64	8.62
	1.00	12.42	10.86	8.87
	1.25	12.50	11.01	8.98
	1.50	12.57	11.08	9.05
20	0.25	11.57	9.85	7.80
	0.50	11.83	10.11	8.02
	0.75	12.07	10.23	8.17
	1.00	12.20	10.55	8.38
	1.25	12.31	10.65	8.50
	1.50	12.35	10.72	8.58
30	0.25	11.43	9.57	7.46
	0.50	11.68	9.82	7.63
	0.75	11.85	9.97	7.76
	1.00	11.98	10.16	7.91
	1.25	12.03	10.23	8.01
	1.50	12.06	10.26	8.06
40	0.25	11.33	9.40	7.26
	0.50	11.54	9.62	7.38
	0.75	11.70	9.75	7.51
	1.00	11.80	9.90	7.63
	1.25	11.84	9.93	7.70
	1.50	11.84	9.94	7.74
50	0.25	11.24	9.28	7.13
	0.50	11.44	9.48	7.24

	0.75	11.59	9.60	7.31
	1.00	11.66	9.65	7.43
	1.25	11.67	9.73	7.50
	1.50	11.66	9.72	7.51
60	0.25	11.17	9.18	7.02
	0.50	11.35	9.35	7.10
	0.75	11.48	9.46	7.18
	1.00	11.54	9.51	7.28
	1.25	11.54	9.56	7.34
	1.50	11.52	9.53	7.34

Appendix C

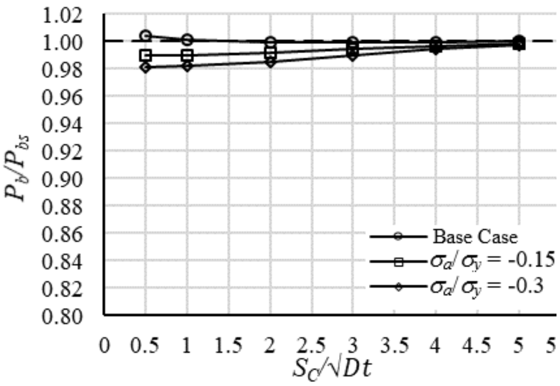

(a) d/t=0.3, $l^2/(Dt)$=2, w/l=1

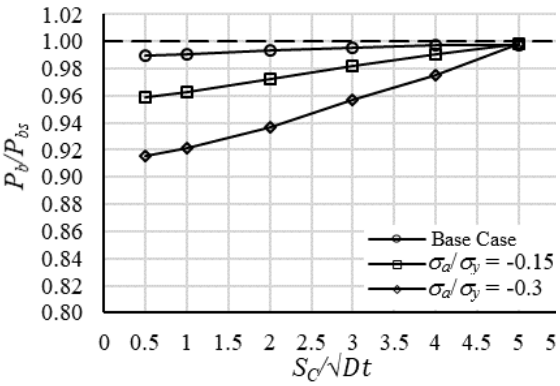

(b) d/t=0.3, $l^2/(Dt)$=20, w/l=1

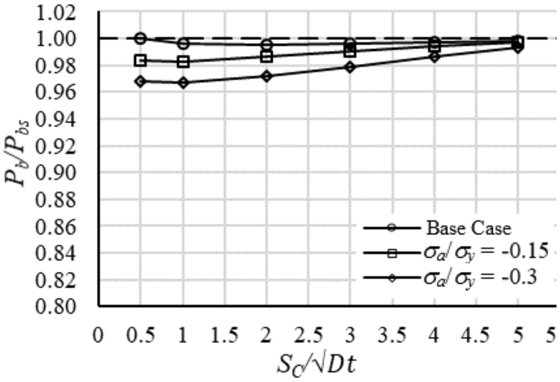

(c) d/t=0.3, $l^2/(Dt)$=10, w/l=0.5

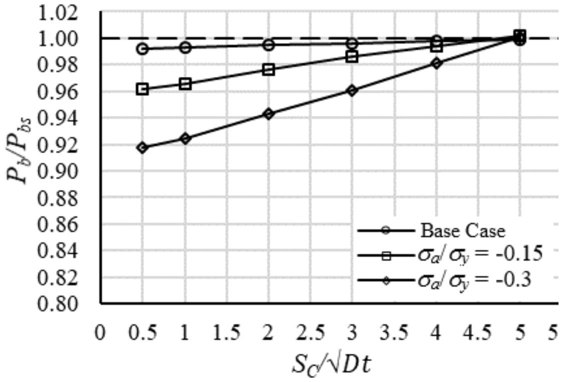

(d) d/t=0.3, $l^2/(Dt)$=10, w/l=1.5

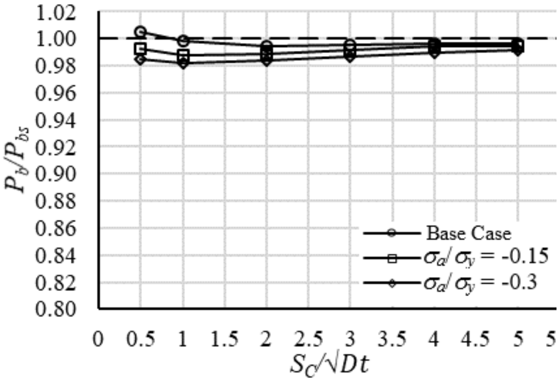

(e) d/t=0.45, $l^2/(Dt)$=2, w/l=0.5

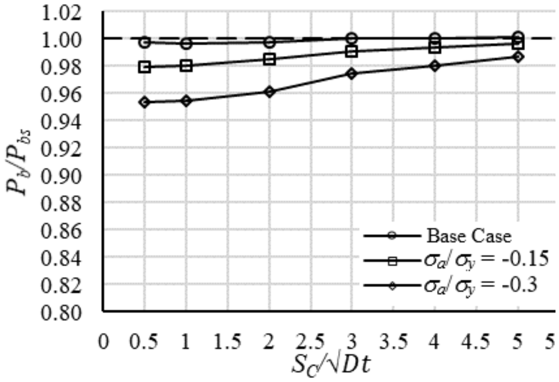

(f) d/t=0.45, $l^2/(Dt)$=2, w/l=1.5

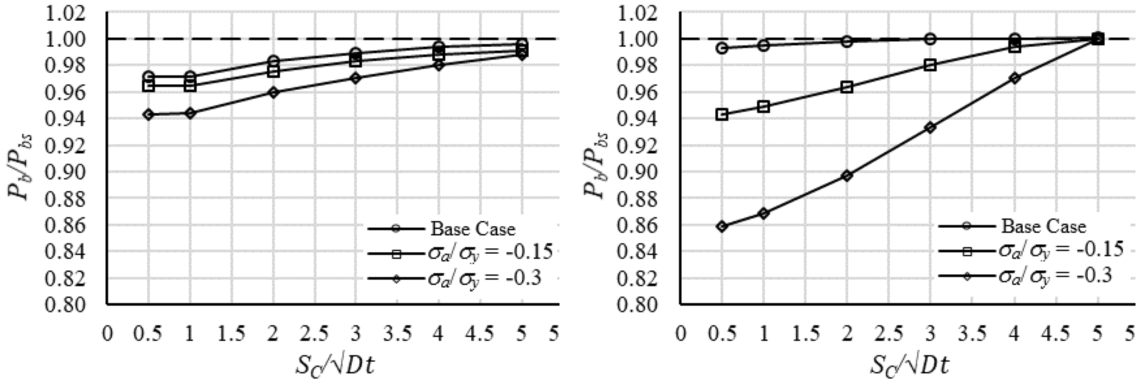

(g) d/t=0.45, $l^2/(Dt)$=20, w/l=0.5 (h) d/t=0.45, $l^2/(Dt)$=20, w/l=1.5

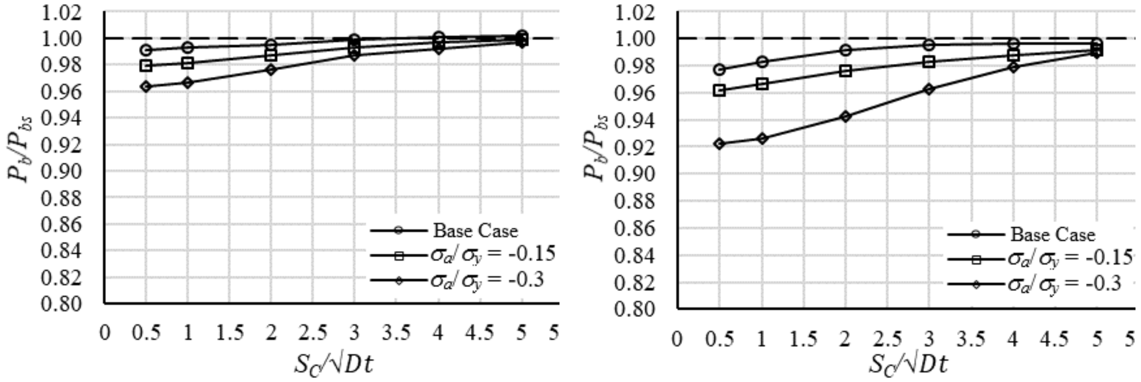

(i) d/t=0.6, $l^2/(Dt)$=2, w/l=1 (j) d/t=0.6, $l^2/(Dt)$=20, w/l=1

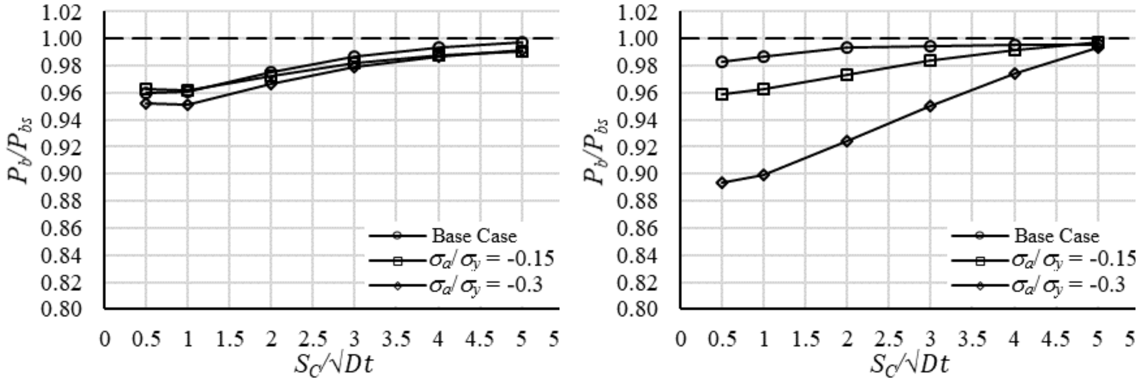

(k) d/t=0.6, $l^2/(Dt)$=10, w/l=0.5 (l) d/t=0.6, $l^2/(Dt)$=10, w/l=1.5

Figure C.1 Interaction effects for circumferentially-aligned corrosion defects under combined loads

Appendix D

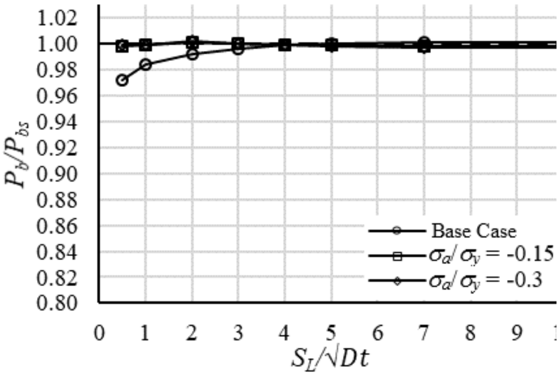

(a) *d/t*=0.3, $l^2/(Dt)$=2, *w/l*=1

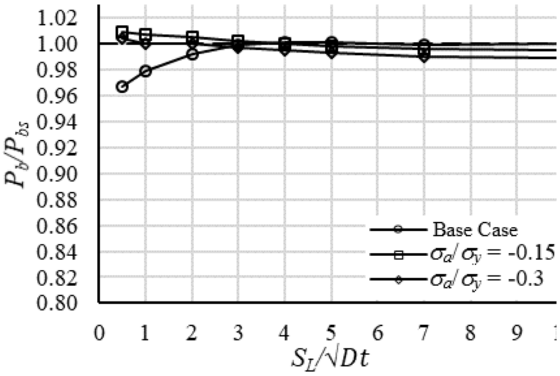

(b) *d/t*=0.3, $l^2/(Dt)$=20, *w/l*=1

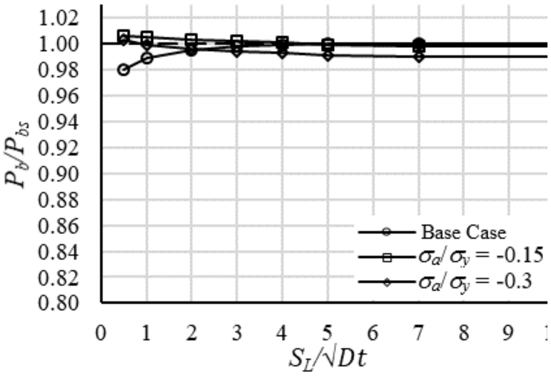

(c) *d/t*=0.3, $l^2/(Dt)$=10, *w/l*=0.5

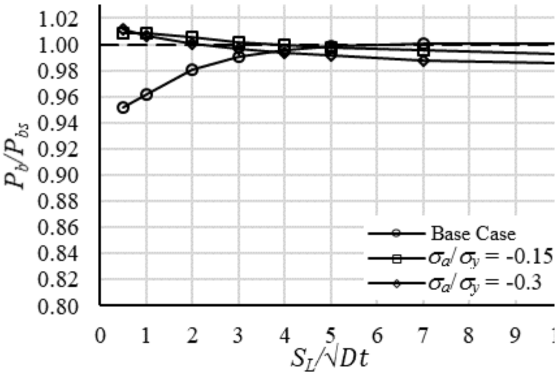

(d) *d/t*=0.3, $l^2/(Dt)$=10, *w/l*=1.5

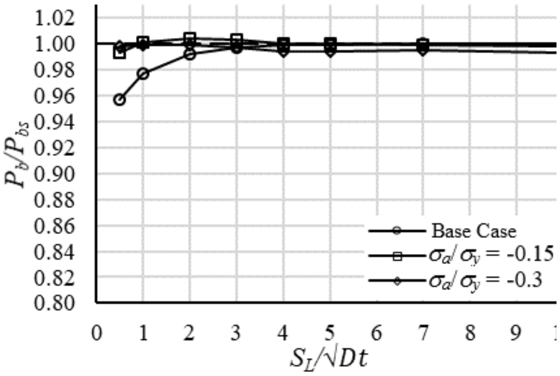

(e) *d/t*=0.45, $l^2/(Dt)$=2, *w/l*=0.5

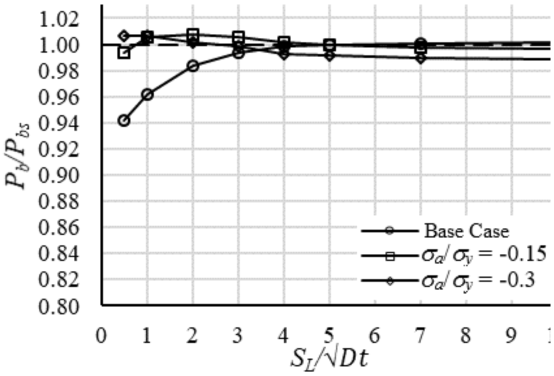

(f) *d/t*=0.45, $l^2/(Dt)$=2, *w/l*=1.5

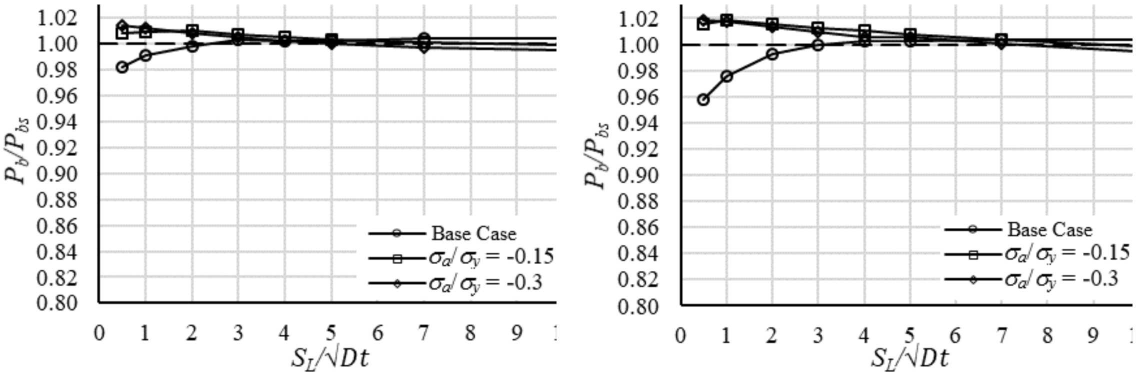

(g) *d/t*=0.45, $l^2/(Dt)$=20, *w/l*=0.5 (h) *d/t*=0.45, $l^2/(Dt)$=20, *w/l*=1.5

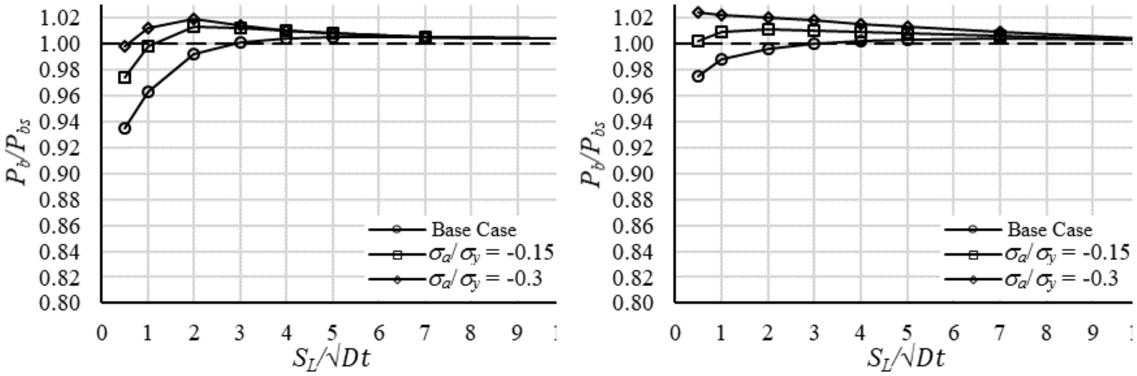

(i) *d/t*=0.6, $l^2/(Dt)$=2, *w/l*=1 (j) *d/t*=0.6, $l^2/(Dt)$=20, *w/l*=1

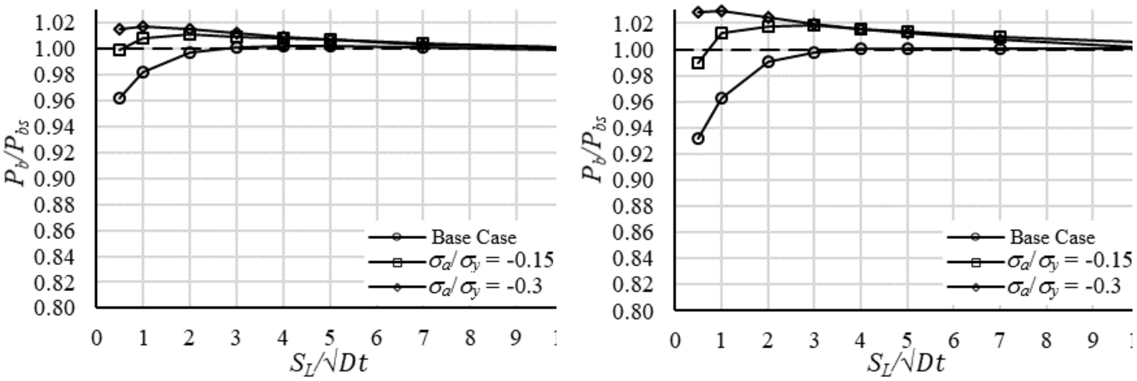

(k) *d/t*=0.6, $l^2/(Dt)$=10, *w/l*=0.5 (l) *d/t*=0.6, $l^2/(Dt)$=10, *w/l*=1.5

Figure D.1 Interaction effects for longitudinally-aligned corrosion defects under combined loads

Curriculum Vitae

Name:	Shulong Zhang
Post-secondary Education and Degrees:	Ocean University of China Qingdao College Qingdao, Shandong, China 2008-2012 B.S. Shandong University Jinan, Shandong, China 2012-2015 M.Sc. The University of Western Ontario London, Ontario, Canada 2016-2017 M.Eng. 2017-2021 Ph.D.
Honours and Awards:	Western Graduate Research Scholarship 2017-2021
Related Work Experience	Teaching Assistant and Research Assisstant The University of Western Ontario 2017-2021

Publications:

Articles in Refereed Journals

Zhang, S., Wang, Q., & Zhou, W. (2019). Implementation of the Tresca yield criterion in finite element analysis of burst capacity of pipelines. *International Journal of Pressure Vessels and Piping, 172*, 180-187.

Zhang, S., & Zhou, W. (2020). Assessment of effects of idealized defect shape and width on the burst capacity of corroded pipelines. *Thin-Walled Structures, 154*, 106806.

Zhang, S., & Zhou, W. (2021). Development of a burst capacity model for corroded pipelines considering corrosion defect width and a revised Folias factor equation. *Journal of Natural Gas Science and Engineering*, 103812.

Zhang, S., & Zhou, W. (2021). Assessment of the interaction of corrosion defects on steel pipelines under combined internal pressure and longitudinal compression using finite element analysis. *Engineering Structures,* (Under review, revision submitted).

Zhang, S., & Zhou, W. (2021). A burst capacity model for corroded pipelines subjected to combined internal pressure and longitudinal compression. *Journal of Pressure Vessel Technology*. (Submitted in January 2021, PVT-21-1019)

Conference Papers

Bao, J., **Zhang, S.**, Zhou, W., & Zhang, S. (2018). Evaluation of burst pressure of corroded pipe segments using three-dimensional finite element analyses. *In International Pipeline Conference* (Vol. 51869, p. V001T03A043). American Society of Mechanical Engineers

Zhang, S., Zhou, W., & Zhang, S. (2020). Development of a Burst Capacity Model for Corroded Pipelines Under Internal Pressure and Axial Compression Using Artificial Neural Network. In *International Pipeline Conference* (Vol. 84447, p. V001T03A028). American Society of Mechanical Engineers.